Abstract

BAO, SHAOWU. Numerical Simulation of the Mesoscale Air-Sea Interaction over the Western Pacific Warm Pool. (Under the direction of Lian Xie and Sethu Raman.)

The purpose of the research is to improve our understanding of the air-sea interaction processes over the region of western Pacific warm pool and ultimately improve weather and climate predictions. To achieve this goal, an air-sea coupled numerical model that includes the momentum, heat and freshwater fluxes across the air-sea interface is developed by combining the Advanced Regional Prediction System (ARPS) and the Princeton Ocean Model (POM).

First, a squall line system observed during the Tropical Ocean Global Atmosphere/Coupled Ocean-Atmosphere Response Experiment (TOGA/COARE) Intensive Observation Period (IOP) is simulated. The simulation results are in agreement with the observations. Sensitivity experiments reveal that the orientation of the initial perturbation can affect the development of the squall line. Inclusion of ice microphysics and surface fluxes affects the strength and extent of the simulated downdraft-induced low level cold air pool.

Then, the ocean's response to precipitation is investigated using the POM model. The results show that the rainfall-induced heat and salinity gradients cause a thin low density, low temperature stable layer near sea surface. The rainfall-induced stable layer near the surface diminishes the downward transfer of the effects of the atmospheric forcing. This causes the effects of the atmospheric forcing to be

concentrated accumulate near the sea surface. Because of this rainfall-induced shallow (about 10 m) stable layer, the sea surface responds to atmospheric forcing much faster than it would do without the rainfall-induced stable layer.

Finally, the air sea coupled system is used to investigate the ocean's response to an observed squall line precipitation process and the feedback effects of the sea surface temperature (SST) variation on the atmosphere. The results show that the SST feedback effect does not have a significant influence on the local existing atmospheric convection. However, the feedback effects have significant effect on the variation of sensible and latent heat fluxes across the air-sea interface, and hence may significantly affect the overall heat and moisture balance in the tropical coupled atmosphere-ocean system. Thus, parameterization schemes of heat and moisture fluxes in large-scale models need to consider not only air-sea heat fluxes due to temperature differences and evaporation, but also the effects of precipitation.

Numerical Simulation of the Mesoscale Air-Sea Interaction over the Western Pacific Warm Pool

By
SHAOWU BAO

A Dissertation Submitted to the Graduate Faculty of
North Carolina State University
in partial fulfillment of the
Requirements for the Degree of
Doctor of Philosophy

Marine, Earth and Atmospheric Sciences

Raleigh, NC
2002

APPROVED BY:

John Morrison	Gerald Janowitz
Sethu Raman Co-chair of Advisory Committee	Lian Xie Co-chair of Advisory Committee

Dedication

To my wife, Ying Zhao, without whose love, support, and understanding I wouldn't have had the confidence to face this challenge

Personal Biograghy

Shaowu Bao was born on March 29, 1971 in Shenyang City, Liaoning Province, China. His father Daxin Bao is a middle school teacher and his mother Xueqing Zhao is a department store manager. In September 1989, he enrolled in Nanjing Institute of Meteorology to pursue a degree in meteorology. He received his Bachelor's degree in 1993. In September 1993, he enrolled in Chinese Academy of Meteorological Sciences and two years later he received his Master's degree. In August 1998, he came to the United States of America and began his study for a Doctoral Degree of Philosophy in the department of Marine, Earth and Atmospheric Science in North Carolina State University.

Acknowledgments

This work is the sum of great help from many great people and I owe them sincere gratitude for what they have done for me. At the top of thanks I would like to acknowledge my committee co-chairs Dr. Xie and Dr. Raman, my committee members Dr. Janowitz and Dr. Morrison, for providing me great help, support and advice. Without your help, it is impossible for me to finish this work.

I would also like to thank my colleagues and friends, Machuan Peng, Xuejin Zhang, TingZhuang Yan, Robert Bright, and Chen Zhang. You all gave me great help over the years. My thanks also go to my friend, Haolin Liu. Your computer knowledge is a great resource to me.

I would also like to say thank you to my parents, Xueqing Zhao and Daxin Bao, and my brother, Shaowen, for your tremendous love and support through out my life.

This work is jointly supported by the Division of Atmospheric sciences, National Science Foundation under grant No. ATM-9632390 and ATM-0080088, and National Oceanic and Atmospheric Administration under grant No. NA06060373-001 through subcontract from the Waterstone Enterprise Strategies and Technologies Inc. The model developments and simulations were performed in the Coastal Fluid Dynamic Laboratory, North Carolina State University, and North Carolina Super-Computing Center, Research Triangle Park, North Carolina.

Table of Contents

List of Tables

Chapter **2**

Chapter 3

Chapter 4

List of Figures

List of symbols

ζ	Vertical coordinate in ARPS model
u	Zonal velocity (m/s)
v	Meridonal velocity (m/s)
w	Vertical velocity (m/s)
f and $\tilde{f}$	Coriolis parameters
S_θ	diabatic term in ARPS model
θ	Potential temperature (K)
D	mixing terms
α	damping coefficient
Q_v	Water vapor (kg/kg)
σ	Vertical coordinate in POM model
q^2	Turbulent kinetic energy (m^2/s^2)
l	Turbulent mixing length (m)
ρ	Density (kg/m^3)
K_m	vertical kinematics viscosity (m^2/s)
K_h	vertical diffusivity
K_q	TKE diffusivity
c_s	Speed of sound (m/s)
k	Von Karman constant
S_h and S_m	Stability coefficients (functions of Richardson number)
τ	Wind stress (N/m^2)
Fs	Rainfall-induced freshwater flux ($kg\ m^{-2}\ sec^{-1}$)
Ft	Rainfall-induced heat flux (W/m^2)
s	Salinity
I	Rain rate (m/s)
Cd	Drag coefficient

$\overline{(u'w')_s}$	Momentum flux (m^2/s^2)
$\overline{(q'w')_s}$	Latent heat flux (W/m^2)
$\overline{(q'w')_s}$	Sensible heat flux(W/m^2)
C_H	bulk transfer coefficient for heat
C_E	bulk transfer coefficient for moisture

Chapter 1 INTRODUCTION

The region of the western Pacific where sea surface temperature (SST) is higher than 28 ^{o} C is called the western Pacific warm pool. Because of the high SST the western Pacific warm pool supplies the atmosphere with a large amount of heat and moisture that result in substantial annual tropical precipitation. Western Pacific warm pool is the product of the air-sea interaction and plays an important role in the global seasonal and inter-annual climate variability, most notably, the El Niño and Southern Oscillation (ENSO).

El Niño is a disruption of the ocean-atmosphere system in the tropical Pacificthat has important consequences for global weather and climate. One aspect of El Niño is the appearance, every few years, of unusually warm surface waters of the Pacific Ocean along the tropical west coast of South America.Today El Niño is referred to as El Niño Southern Oscillation (ENSO). Southern oscillation refers to a seesaw shift in sea surface pressure at Darwin, Australia and the South Pacific Island of Tahiti. When the pressure is high at Darwin, it is low at Tahiti and vice versa. El Niño is an extreme phase of the southern oscillation

ENSO affects fishing, agriculture, and local weather from Ecuador to Chile and can cause global climate anomalies in the equatorial Pacific, Asia, and North America. It is estimated that the worldwide damage caused by the 1982-83 El Niño exceeded $10 billion.

Because of the significant impacts of ENSO on global weather and climate, it has been extensively investigated. The seasonal and inter-annual air-sea coupling mechanism in ENSO has been well understood.

The atmospheric pressure fluctuations between the western Pacific and the eastern Pacific was observed as early as the end of nineteenth century and the beginning of 20th century. The negative atmospheric pressure anomaly in the western Pacific corresponds with the concurrent occurrence of positive atmospheric pressure anomaly in the eastern Pacific, and vice versa. The western Pacific normally is characterized by low atmospheric sea-level pressure, tropical convection, ascending air and intense precipitation. The eastern Pacific is characterized by high atmospheric sea-level pressure, subsidence and dry conditions. The ascending air and descending air, with the low level westward zonal trade wind and the upper level eastward flow, form the zonal "Walker circulation". During the high phase of Southern Oscillation, the phase of the Southern Oscillation characterized by higher than normal pressure on the eastern side of the Pacific and lower than normal pressure on the western side, the western part of Pacific has a negative atmospheric pressure anomaly and the low pressure is deeper than usual, the eastern part has a positive atmospheric pressure anomaly and the high pressure is higher than usual, thus the zonal trade wind is enhanced. During the low phase of the SO, the western Pacific has a positive pressure anomaly and the eastern Pacific has a negative pressure anomaly, the zonal trade winds are weakened.

Normally easterly (westward) trade winds prevail over the equatorial Pacific. The ocean responses to the easterly trade wind forcing include a sea level gradient and a

SST gradient. Due to the easterly trade wind, the western Pacific has a higher sea level than that of eastern Pacific. The SST in the western part of Pacific is also higher than that in the eastern part. However the fishermen along the coasts of Peru and Ecuador noticed that in some years the normally cold water becomes especially warmer than usual. This long lasting and intense positive SST anomaly is originally called El Niño. The opposite of El Niño is known as La Nina when the cold water becomes colder than usual.

ENSO is a complicated nonlinear air-sea interaction system. The prevailing easterly trade winds are periodically interrupted by strong westerly wind bursts (WWB). The westerly wind bursts can generate Kelvin waves propagating eastward. The weakening of easterly trade winds and the eastward propagating of Kelvin waves cause a negative SST anomaly over western Pacific warm pool and a positive SST anomaly propagation eastward with the eastward propagating Kelvin waves. The eastward propagating of the positive SST anomaly causes the convection and precipitation to shift eastward. So the central and eastern parts of the Pacific experience more precipitation and the western Pacific may have drought.

SST changes have impacts on the atmospheric circulation that, in turn, can strengthen the SST variation. During El Niño years, the negative SST anomaly over the western Pacific causes the weakening of the ascending air motion and the positive SST anomaly over the central and eastern Pacific causes the weakening of the descending air motion. Meanwhile, the east trade winds weakens, which in turn strengthens the negative SST anomaly over the western Pacific and the positive SST anomaly over the eastern Pacific. Thus the air-sea system causes a feedback looping which turns the weakening of zonal trade winds or the westerly wind burst into global

seasonal or inter-annual climate variations. The conditions are reversed during La Nina years.

Although the importance of air-sea interaction in seasonal to inter-annual climate prediction is well documented, as mentioned above, the air-sea coupled processes in cloud scale, mesoscale to synoptic scale weather and ocean prediction and on time scales from hours to days over the western Pacific warm pool are not well understood. The mesoscale air-sea interaction processes are thought to be important in the areas with intense convection such as the western Pacific warm pool. For example, Gary Barnes (1994) stated that "The ocean and atmosphere in the tropics communicate on the mesoscale". Mesoscale precipitation systems play an important role in the ENSO cycle. Such precipitation systems are also connected with westerly wind bursts over the equatorial western Pacific, which sometimes trigger the onset of the El Niño events. However, not much is known about the nature of the western Pacific precipitation systems - their structure, how they form, how they impact the upper ocean and how the upper ocean's feedback effects affect the atmosphere. The physical mechanisms are not well understood yet. The progress was limited by lack of high quality measurements of air-sea fluxes of heat, moisture, and momentum in the warm pool region and by the difficulty encountered by coupled models in simulating air-sea interaction processes over the western Pacific warm pool. In order to enhance the understanding of the principal air-sea interaction processes over the western Pacific warm pool both the availability of high quality measurements and the improvement of air-sea coupled models are necessary.

The TOGA/COARE (tropical ocean-global atmosphere/ Coupled ocean-atmosphere response experiment) was conducted from 1992 to 1993 over the western Pacific warm pool. One of its main objectives was to describe and understand the principal processes responsible for the coupling of the ocean and the atmosphere in the western Pacific warm pool system. The field phase of the TOGA/COARE was very successful. Data collected during the experiment provided investigators with great potential for understanding the air-sea interaction processes in the warm pool. However, success in the field program of TOGA/COARE is yet to be translated into improvement of the coupled atmospheric ocean models.

The principal goal of this study is to enhance the understanding of the mesoscale air-sea interaction mechanisms in the western Pacific warm pool. The improvements in the understanding of the mesoscale air-sea interaction mechanisms can lead to better parameterization of air-sea fluxes ultimately more accurate coupled climate models for seasonal to inter-annual prediction. A coupled system that combines the Advanced Regional Prediction System (ARPS) and Princeton Ocean Model (POM) is developed. The coupled system is described in Chapter 4. Results from the simulation of a squall line system observed during TOGA/COARE IOP are presented in Chapter 2. The simulated results compare well with the observations. Several sensitivity experiments are conducted to investigate the influence of different factors on the squall line structure and evolution, including the microphysics scheme, surface turbulent fluxes of momentum and heat, and the orientation and strength of the initial potential temperature perturbation.Results of the numerical experiments conducted to investigate the ocean's response to precipitationare discussed in Chapter 3. Oceanic response to an idealized precipitation process with similar characteristics observed

during TOGA COARE was simulated. The simulation reproduced some of the observed ocean responses to the precipitation, such as the formation of a fresh water layer, surface cooling and the variation of upper layer turbulent mixing. Sensitivity experiments reveal that the sea surface temperature increases faster after rainfall due to the formation of a shallow fresh water layer near the surface In Chapter **4**, development of a coupled system that combines the Advanced Regional Prediction System (ARPS) and Princeton Ocean Model (POM) is discussed. The numerical simulation results of the oceanic response to a squall line system observed during TOGA/COARE and the ocean's feedback effects on atmosphere are presented. Main conclusions of this research are summarized in Chapter 5.

Chapter 2. NUMERICAL SIMULATION OF A TROPICAL SQUALL LINE CONVECTION OVER PACIFIC OCEAN

2.1. Introduction

The western Pacific warm pool has a mean annual sea surface temperature (SST) of about 29°C. Because of the large SST, the western Pacific warm pool supplies the atmosphere with large amounts of water vapor and heat that result in substantial annual tropical precipitation. It has an important influence on the global climate and weather pattern and in the occurrence of the El Niño / La Nina events.

The 1992-93 Tropical Ocean Global Atmosphere Coupled Ocean Atmosphere Response Experiment (TOGA COARE) was an international field program to study the atmospheric and oceanic coupling processes over this warm pool region (Webster and Lukas, 1992). Squall line is defined as a line or band of active thunderstorms, which are generally observed to last several hours. There were many squall lines over the western Pacific warm pool region during the TOGA COARE experiment. In this paper, a well-documented squall line on Feb 22, 1993 was simulated using the 3-D Advanced Regional Prediction System (ARPS) model. This squall line has been investigated by Jorgensen (1995), Trier et al. (1996) and Hong et al. (1999). Jorgensen (1995) presented the general structure and momentum fluxes of the squall line using observations by airborne doppler radar over the TOGA COARE region.

Trier et al. (1996) conducted a 3-D numerical simulation of this squall line using a primitive equation model with a fully automated adaptive-grid algorithm and suggested that the ice microphysics in the simulation is important to produce realistic strength and depth of the convectively induced cold air poolTheir study also showed that the surface fluxes have significant influence on the strength and the areal extent of the simulated surface cold air pool.

In this Chapter results from the simulation of the Feb 22,1993 squall using the ARPS (Advanced Regional Prediction System) model developed at University of Oklahoma (Xue *et. al.* 1995) to investigate its structure and evolution. Several sensitivity experiments were conducted to study theinfluence of different factors on the squall line development, including the microphysics scheme, surface turbulent fluxes of momentum and heat, and the orientation and strength of the initial potential temperature perturbation.

2.2. Observations

2.2.1. Observed characteristics of the squall line

The Feb 22, 1993 event during TOGA COARE was a rapidly eastward propagating squall line. This 100 km convective line, observed near Guadalcanal island (9^{o}S, 160^{o}E), was northwest to southeast oriented with a direction of around 150^{o}-330^{o}, nearly perpendicular to a low-level wind shear and was located at the leading edge of a large-scale west wind burst. This observed convective line experienced a transition from a highly linear line to a bow shape in about 1.5 hours.

At the two edges of this line of convection, two vortices were observed. One was counter-clockwise at the north end and the other clockwise at the south end. Along with these vortices, westerly rear inflow was also observed. Vertically the squall line was characterized by rearward tilt and updraft maximums at two altitudes. Updrafts at low altitudes (about 2 km) were observed to be about 4-5 m/s and the ones at a height of 10 km were at about 8-10 m/s (Jorgensen, 1994).

2.2.2. Sounding used in the simulation

The sounding data used in this paper is based on the Feb 22,1993 observations from Honiara Guadalcanal (Figure 2.1). For this sounding, the CAPE (Convective Available Potential Energy) defined for irreversible pseudo-adiabatic ascent of air parcel averaged through the lowest 50mb is 1500 Jkg^{-1} (Figure 2.1 a). This moderate unstable profile has a strong vertical wind shear due to a low-level jet of 12m/s at an altitude of about 2 km (Figure 2.1 b).

2.3. Model Description and Configuration

ARPS model is a non-hydrostatic atmospheric prediction model and can be used to study atmospheric motions with scales ranging from a few meters to hundreds of kilometers. The model is based on compressible Navier-Stokes equations describing the atmospheric flow, and uses a generalized terrain-following coordinate system (Xue, 1995).

The governing equations of ARPS are written in a curvilinear coordinate system defined by:

$$\xi = x,$$
$$\eta = y,$$
$$\zeta = \zeta(x, y, z).$$

The governing equations are given by:

$$\frac{\partial u^*}{\partial t} = -\left[u^* \frac{\partial u}{\partial \xi} + v^* \frac{\partial u}{\partial \eta} + W^{\zeta^*} \frac{\partial u}{\partial \zeta}\right] - \left[\frac{\partial}{\partial \xi}\left\{J_3 (p' - \alpha Div^*)\right\} + \frac{\partial}{\partial \zeta}\left\{J_1 (p' - \alpha Div^*)\right\}\right] + \left[\rho^* fv - \rho^* \tilde{f} w\right] + \sqrt{G}\, D_u, \tag{2.1}$$

$$\frac{\partial v^*}{\partial t} = -\left[u^* \frac{\partial v}{\partial \xi} + v^* \frac{\partial v}{\partial \eta} + W^{\zeta^*} \frac{\partial v}{\partial \zeta}\right] - \left[\frac{\partial}{\partial \eta}\left\{J_3 (p' - \alpha Div^*)\right\} + \frac{\partial}{\partial \zeta}\left\{J_2 (p' - \alpha Div^*)\right\}\right] - \rho^* fu + \sqrt{G}\, D_v, \tag{2.2}$$

$$\frac{\partial}{\partial t}(\rho^* w) = -\left[u^* \frac{\partial w}{\partial \xi} + v^* \frac{\partial w}{\partial \eta} + W^{\zeta^*} \frac{\partial w}{\partial \zeta}\right] - \frac{\partial}{\partial \zeta}(p' - \alpha Div^*) + \rho^* B + \rho^* \tilde{f} u + \sqrt{G}\, D_w \tag{2.3}$$

$$\frac{\partial}{\partial t}(\rho^* \theta') = -\left[u^* \frac{\partial \theta'}{\partial \xi} + v^* \frac{\partial \theta'}{\partial \eta} + W^{c*} \frac{\partial \theta'}{\partial \zeta}\right] - \left[\rho^* w \frac{\partial \bar{\theta}}{\partial z}\right] + \sqrt{G}\, D_\theta + \sqrt{G}\, S_\theta \tag{2.4}$$

$$\frac{\partial}{\partial t}(\rho^* q_\psi) = -\left[u^* \frac{\partial q_\psi}{\partial \xi} + u^* \frac{\partial q_\psi}{\partial \eta} + W^{c*} \frac{\partial q_\psi}{\partial \zeta}\right] + \frac{\partial(\rho^* V_{q_\psi} q_\psi)}{\partial \zeta} + \sqrt{G}\, D_{q_\psi} + \sqrt{G}\, S_{q_\psi} \tag{2.5}$$

where

$$\rho^* = \sqrt{G}\,\bar{\rho}$$
$$u^* = \rho^* u$$
$$v^* = \rho^* v$$
$$w^* = \rho^* w$$
$$Wc^* = \rho^* Wc$$

$$J_1 \equiv J^{yz}_{\xi\eta} = -\frac{\partial z}{\partial \xi},$$
$$J_2 \equiv J^{zx}_{\xi\eta} = -\frac{\partial z}{\partial \eta},$$
$$J_3 \equiv J^{zx}_{\zeta\xi} = \frac{\partial z}{\partial \zeta}.$$

$$\sqrt{G} = |J_3|$$

$$U^c = uJ_3 / \sqrt{G} \ ,$$
$$V^c = vJ_3 / \sqrt{G} \ ,$$
$$W^c = (u J_1 + v J_2 + w) / \sqrt{G}$$

$$p\ (x,y,z,t) \quad = \quad \overline{p}\ (z) + p'\ (x,y,z,t)$$

$$Div^* = \frac{1}{\sqrt{G}} \left[\frac{\partial u^*}{\partial \xi} + \frac{\partial v^*}{\partial \eta} + \frac{\partial W^{c*}}{\partial \zeta} \right]$$

S_q = diabatic term

q = potential temperature

D = mixing terms

a = damping coefficient

f and $\tilde{f}$ = Coriolis parameters in east-west and north-south directions

Turbulence parameterization, which is a planetary boundary layer (PBL) closure linking the resolved scales and the unresolved subgrid-scales is critical to the successful simulation of many flows. In ARPS, four options of turbulence parameterization are available: first order closure, Smagorinsky/Lilly closure (Smagorinsky, 1963; Lilly 1962), 1.5-order TKE closure, and Germano Scheme

(Germano et al., 1991). In this study, the 1.5-order TKE closure is used to compute the turbulent mixing.

In this study, two cloud microphysics schemes are used. One is Kessler warm rain microphysics and the other is a water/ice scheme. Kessler's warm rain scheme considers three categories of water: water vapor, cloud water and rain water. When the air becomes saturated, the condensation occurs and cloud droplets are formed. Cloud droplets turn into raindrops by auto-conversion. Then raindrops fall at their terminal speed and collect smaller cloud droplets by accretion. Cloud droplets and raindrops evaporate in unsaturated air. The water/ice scheme used in this study is based on Kessler scheme and includes three more categories for ice-phase: cloud ice, snow, and graupel /hail.

Numerical simulation is often sensitive to surface fluxes of heat, momentum and moisture. A stability and roughness-length dependent surface flux model is used (Businger, et. al. 1971). The surface fluxes enter the model as the lower boundary conditions for the turbulent momentum and heat fluxes.

The center of the simulation domain is located at 9°S, 160°E because of the availability of observations in this region. Generalized terrain-following coordinate with equal spacing in x and y directions and grid stretching in the vertical is used. The simulation domain is 120 km x 120 km with a horizontal resolution of 2km. We used vertical stretching with hyperbolic tangent to enhance the resolution of the low-level grids. We assumed that the initial condition is horizontally homogeneous in the entire simulation domain and used a single sounding as the initial condition (Figure 2.1).

Because this squall line system moved eastward at a speed of around 10 m/s, a grid translation is used to keep the system within the simulation domain. The translation speed, set to be 12 m/s for east-west wind speed (U) and –3m/s for north-south wind speed (V), does not change during the simulation.

A low-level (at 150m) negative potential temperature anomaly of 8K is used to initialize the convection at the beginning of the simulation. The initial perturbation of the potential temperature is given in Figure 2.2. The initial potential temperature perturbation also has an orientation of 150^{o} to 330^{o} consistent with the shape of the observed convective line. Other initial potential temperature perturbations with different orientations and strengths were used in the sensitivity experiments to investigate the influence of the initial perturbation on the structure andthe evolution of the squall line.

2.4. Simulation of the FEB 22, 1993 TOGA COARE Squall Line

In this simulation both ice microphysics and surface fluxes are included. The simulation reproduced some key observed characteristics of the TOGA COARE squall line.

Simulated horizontal wind and vertical velocity fields at a height of 1.5 km are shown in Figures 2.3a, 2.3b, 2.3c and 2.3d for 2h, 3h, 4h, and 5h of integration, respectively. At this altitude the observed and hence initialized east-west wind component (U) was 11 m/s and north-south wind component (V) was –5m/s. The

system grid translation speed was set to 12 m/s (U) and –3 m/s (V) respectively. Hence, in Figure 2.3 the vectors are the system relative velocities.

The transition from the highly linear initial perturbation (Figure 2.2) to the bow shaped leading edge convective line occurs after 2 h of model integration (Figure 2.3a). The maximum vertical velocity at this time reaches 6.59 m/s. The convective system expanded to more than 80 km long from its initial 50 km extent potential temperature perturbation. At 3 h and 4 h (Figures 2.3b and 2.3c respectively), the convective system develops further and the rainfall increases rapidly. However, at 5h the structure of the squall line is not as coherent as before.The simulated maximum vertical velocity is 6.6 m/s at 2h, 8.0 m/s at 3h and 8.4 m/s at 4h and 9.7 at 5h of integration. A downdraft region is simulated at 2h, 3h, 4h, and 5h of integration behind the leading edge of the convective line as indicated in Figures 2.3a, 2.3b, 2.3c and 2.3d respectively. These downdrafts with a maximum value of about 3.2 m/s are much weaker than the updrafts. The accumulated rainfall occurs mainly in the locations of the downdraft region behind the strong updraft leading edge, in agreement with the observations (Trier *et al.* 1996). The simulated accumulated maximum rainfall reaches a value of 191 mm at 3 h and 245 mm at 4 h as shown in Figures 2.4a, 2.4b, 2.4c, and 2.4d representing for simulation times 2h, 3h, 4h, and 5h respectively.

The downdrafts associated with the rainfall caused a low-level dry cold air pool at an altitude of 150m as shown in Figure 2.5. The maximum potential temperature deficit at this height reaches a value of 6K. Comparing Figures 2.3, 2.4 and 2.5, it is apparent that the cold air pool expands at the same speed as the convective line. The

leading edge of the simulated cold air pool and that of the updrafts are coincident. The maximum in the potential temperature perturbation occurs in the area behind the leading edge of the updraft. It is believed that the cold air pool is the result of the melting of the ice and the resulting evaporation during the precipitation. In the region behind the squall line system, the simulated cold air pool has covered a larger area (Figure 2.5) than that of the rainfall (Figure 2.4) due to the divergent outflow below the melting layer. The intensity of the cold air pool decreases with the distance from the leading edge of the convective line.

From Figures 2.3 and 2.4, it is obvious that the transition of the squall line from linear to the bow shape structure is associated with a strong rear inflow jet of about 10 m/s and two vortices at the two ends of the bow shaped convective line. One of these is clockwise at the south end and the other counter-clockwise at the north end. With the propagation of the squall line, the rear inflow and the two vortices get stronger. Basically, the centers of the two vortices correspond to the rainfall centers and the cold air pool regions.

Vertical cross-sections of the perturbations of the potential temperature and water vapor are shown in Figure 2.6a, 2.6b, 2.6c and 2.6d for 2h, 3h, 4h and 5h integration of the model respectively. A strong low-level convergence results in a strong updraft at the leading edge of the squall line at 2h (Figure 2.6a). In the rear of the squall line, the low-level horizontal winds are eastward and in the front of the squall line, winds are westward. A low-level vertical wind shear is simulated, which results in a significant rearward tilting structure of the convection. This rearward tilting is also one reason that the cold air pool expanded behind the squall line. As can be seen in

Figure 2.6, the updraft region corresponds to the positive moisture content (Q_v) perturbation region (the dark shaded area in Figure 2.6) in the lower levels (below 1 km). The cold air pool area (the dashed contour) is consistent with the negative Q_v area (the light shaded area) indicating dry region.

Another feature of the simulated vertical structure in agreement with the observations is the prediction of regions of maximum vertical velocity (W) at two altitudes as shown in Figure 2.6. One maximum W is simulated at 2 km altitude, and another one at about 8-10 km (Figure2.6a). At model integration time of 4 h and 5 h as shown in Figures 2.6c and 2.6d respectively, the maximum vertical velocities at 2 km are still large with a value of about 8 m/s, but the values at higher altitudes become smaller.

2.5. Sensitivity Experiments

Five numerical sensitivity experiments were conducted in this study and the results are given in Table 2 1.

The simulations discussed in section 2.4 are for the CONTROL experiment. NOICE and NOFLUX numerical experiments were conducted to investigate the influence of ice microphysics and surface heat, moisture, and momentum fluxes respectively. In NOICE experiment, only Kessler warm rain scheme is used, while in CONTROL, a microphysics scheme including ice, snow and graupel is used. In the NOFLUX experiment, surface fluxes are switched off. Experiments WEAK-PTPRT and N-S were conducted to investigate the influence of the initial perturbation on the

structure and evolution of the squall line. In WEAK-PTPRT, the strength of the initial potential temperature perturbation is set to −2K while in CONTROL it was −8K. In N-S, the orientation of the initial potential temperature perturbation is set to exactly North-South, while in CONTROL, it was Northwest-Southeast with an angle of 120 ^{o}/300 ^{o} as observed.

Table 2.1. Details of the sensitivity experiments.

Experiments	Initial perturbation orientation (Degree to north)	Initial perturbation strength	Ice Microphysics scheme	Surface fluxes
CONTROL	120/300	8K	Yes	Yes
NOICE	120/300	8K	No	Yes
NOFLUX	120/300	8K	Yes	No
WEAK-PTPRT	120/300	2K	Yes	Yes
N-S	0/180	8K	Yes	Yes

2.5.1 Sensitivity to the initial perturbation

Experiments WEAK-PTPRT and N-S were conducted to investigate the influences of the different initial perturbations on the structure and evolution of the squall line. In WEAK-PTPRT, the initial potential temperature perturbation is set to 2K, much weaker than that in CONTROL (-8K). In N-S, the orientation is set to be exactly north south. In CONTROL, The orientation is set to 120-300^{o} in accordance with the observations. In WEAK-PTPRT and N-S, all the other parameters are the same as those in CONTROL except for the strength and orientation of the initial perturbation.

Figures 2.7 and 2.8 show the development of the convective system in WEAK-PTPRT. There is no significant difference between the CONTROL and WEAK-

PTPRT in the development of the squall line. AT 2 hour, the bow-shapestructure is already evident. However in WEAK-PTPRT the magnitude of the updraft (Figure2.7) and the intensity of the rainfall (Figure 2.8) are smaller than those in CONTROL (Figure 2.3 and 2.4). Because of the weaker rainfall, the cold air pool is also weaker propagating at a slower speed in WEAK-PTPRT as compared to CONTROL experiment (Table 2.2). But the differences are not significant if we take into account the big difference of 6K in the strength of the initial potential temperature perturbations. This numerical simulation result indicates that a strong initial cold air pool with a potential temperature anomaly of 8K is not needed to simulate this convective system and the observed cold air pool. This is because the initial cold air pool only acts to trigger the convection. Once the convection is initialized,the shape and strength of the cold air pool is mainly determined by the model-generated precipitation and downdraft and not the strength of the initial perturbation

Table 2.2. Comparison of maximum potential temperature perturbation (PTPRT) at z=150m, maximum vertical velocity at z=1500m (W) and maximum rainfall between CONTROL and WEAK-PTPRT experiments.

	Min of PTPRT (K)			Max of W (m/s)			Max Rainfall (mm)	
	CONT	Weak		CONT	weak		CONT	weak
1 hour	-4.8	-2.2		5.5	1.6		41	28.2
2 hour	-4.3	-2.9		6.6	5.2		124	112
3 hour	-6.5	-4.4		8.0	5.5		191	189
4 hour	-6.2	-6.1		8.4	7.4		245	271
5 hour	-7.7	-6.5		9.7	7.3		291	314
6 hour	-7.8	-7.2		7.3	9.8		347	332

In N-S experiment, the convective system develops much slower than in CONTROL. A comparison of maximum potential temperature perturbation at different integration time is shown in Table 2.3. By comparing Figure 2.4 with Figure 2.9 a, it is obvious that it takes longer for the convective line to transform from linear to bow shape. After two hours of integration in the CONTROL experiment the convective line has showed a bow-shape structure while in N-S the transition has just begun and the squall line is basically still a linear structure. At this model time, the simulated cumulative precipitation has reached 110 mm, while in the N-S the simulated rainfall is only 40 mm. Because of the weaker rainfall and downdraft (Table 2.3), the cold air pool in N-S is also weaker and covered a smaller (Figure 2.10) area than that in CONTROL.

Table 2.3. Comparison of maximum potential temperature perturbation (PTPRT) at z=150m, maximum vertical velocity at z=1500 m (W) and maximum rainfall between CONTROL and N-S experiments.

	Min of PTPRT (K)			Max of W (m/s)			Max Rainfall (mm)	
	CONT	N-S		CONT	N-S		CONT	N-S
1 hour	-4.8	-1.7		5.5	3.2		41	6
2 hour	-4.3	-1.36		6.6	3.9		124	43
3 hour	-6.5	-3.76		8.0	6.5		191	109
4 hour	-6.2	-5.37		8.4	7.6		245	188
5 hour	-7.7	-5.91		9.7	7.3		291	236
6 hour	-7.8	-6.58		7.3	7.0		347	274

Figure 2.11 is the cross section of the potential temperature, moisture, and vertical velocity in N-S. After 3 hours of model integration, from the potential temperature perturbation (the dashed line contour near surface in Figure2.11), the

cold air pool in N-S experiment is significantly weaker than that in CONTROL (Figure 2.5a). It also covers a smaller area. This same difference continues at 3h, 4h and 5h of model integration.

In N-S experiment, the magnitude of initial potential temperature perturbation is the same as that in CONTROL (-8K), but the orientations are different by 60^0. However the simulated results are quite different. While in WEAK-PTPRT, the orientation was the same as that in CONTROL, the initial magnitudes of perturbation were quite different (-8K in CONTROL and −2K in WEAK-PTPRT). No significant difference results from the big difference in the initial perturbation strength. Simulated results show that the orientation of the initial perturbation has more significant impact on the evolution of the squall line that of the magnitude of the initial perturbation.

2.5.2. Influence of Ice Microphysics

In the squall line system, the updraft reaches an altitude higher than 10kmwhere formation of the ice could play an important role in the cloud physics Inclusion of ice and snow in the microphysics scheme may be important to obtain more realistic simulation. In NOICE experiment, the Kessler warm rain microphysics is used to investigate the influence of the ice microphysics on the simulation of the squall line. From Figures 2.12 (a, b, c, d) and Figures 2.3, and 2.4, one can see that the exclusion of the ice and snow in the microphysics scheme in NOICE did not make a significant difference in the horizontal wind field and the updraft pattern. There was no significant difference in the rainfall distribution (Figures 2.13). However, the rainfall amount is significantly less than in CONTROL (Table 2.4).

Table 2.4. Comparison of cumulative rainfall (mm) between CONTROL and NOICE experiments.

	1 hour	2 hour	3 hour	4 hour	5 hour	6 hour
Control	41	124	191	245	291	347
NOICE	38	113	150	178	221	242

The weaker simulated precipitation results in a less intense downdraft. In Figure 2.12, the downdrafts behind the convective leading edgesare –2.70 m/s, -2.66 m/s, -2.96 m/s and –2.51 m/s at 2,3,4,5 hours of model integration respectively, less than those in Figure 2.3 for the CONTROL experiment, which were –3.17 m/s, -3.7 m/s, -3.07 m/s and –3.95 m/s respectively.

The convective line causes precipitation and the downdraftsbehind the leading edge. Divergence associated with the downdrafts causes movement of the squall line. A slower movement of the squall line occurred in NOICE experiment than in CONTROL as can be seen in Figures 2.6 for CONTROL and Figure 2.14 for NOICE experiment. At the 4^{th} hour of model integration, the squall line leading edge in NOICE experiment is 10 Km behind that in CONTROL experiment.

Because the cold air pool is formed mainly by the melting and evaporation during the precipitation, less intense precipitation leads to a less intense cold air pool (Figure 2.15). Also the weaker downdrafts lead to weaker downdraft-induced divergent low-level outflow. This might be the reason why in NOICE experiment the cold air pool covers a smaller area over the sea surface than in CONTROL (Figure 2.15).

From Figure 2.**14** (a, b, c, d), another feature associated with the cold air pool, negative water vapor perturbation or drying of the air (Q_v, the light shaded contour lines near the surface), another feature associated with the cold air pool, is also apparent. Comparing Figures 2.6 and 2.**14**, one can see that the depth of the negative potential temperature perturbation area in NOICE experiment is smaller than that in CONTROL. In CONTROL experiment the potential temperature perturbation reaches –3.5 K, while in NOICE experiment it reaches only –3 K. This difference also indicates that the exclusion of ice and snow in the microphysics reduces the strength of the cold air pool formed by the precipitation.

2.5.3. Influence of the Surface Fluxes

Because of the high SST in the western Pacific warm pool region, the inclusion of surface heat and moisture fluxes would lead to a warmer and dryer low level cold air pool in the simulated downdraft region, thus reducing the strength and extent of the negative potential temperature anomaly as shown in Table 2.5. From Table 2.5 it is clear that during most of the model integration the cold air pool in CONTROL experiment is weaker than that in NOFLUX experiment, due to the inclusion of surface fluxes in CONTROL experiments. Figure 2.16 is the vertical cross section of the potential temperature perturbation, water vapor perturbation, and U-W vector for NOFLUX experiment. From a comparison between Figure 2.**16** and Figure 2.6 it is apparent that both the depth and the extent of the cold air pool in NOFLUX experiment are stronger than those in CONTROL. At 3h of model integration, the difference is not large between the NOFLUX experiment and the CONTROL. But at 4h of model integration the difference becomes more significant. The leading edge of

he cold air pool in CONTROL experiment is 10 Km behind that in NOFLUX experiment. In Figure 2.**16** (NOFLUX experiment), one can see a maximum of –4K (the dashed line) in the contours of potential temperature perturbation. While in Figure 2.6 (CONTROL experiment), the maximum values reached only –3K. In NOFLUX experiment, the depth of negative Q_v perturbation area is also deeper than that in CONTROL experiment. In NOFLUX experiment, the simulated negative Qv perturbation reaches an altitude of 3 km while in CONTROL experiment the simulated negative Q_v perturbation only reaches a height less than 2 km. Both these comparisons indicate a stronger and dryer cold air pool in NOFLUX experiment. At 4 hour of model integration, in CONTROL experiment the simulated leading edge of the convective line reached a distance of 90 km from its western boundary (Figure 2.6), while in NOFLUX experiment, it reached a distance of about 95km. At 5 hour of model integration, the difference becomes even more prominent. Due to the inclusion of the heat and moisture fluxes, the strength and depth of the cold air pool remained almost the same as at 4h of model integration with the -3K line as the maximum magnitude of the cold air pool strengthas shown in Figure 2.6d. But in Figure 2.**16**d (NOFLUX experiment), the –0.5 K contours reaches heights above 3km. The maximum magnitude of the potential temperature perturbation reaches–4K, located near the surface. Thus the depth of the cold air pool is larger in NOFLUXexperiment (Figure 2.**16**d) than in CONTROL experiment (Figure 2.6d). This is believed to be due to substantially less mixing in the NOFLUX case.

Table 2.5. Comparison of maximum potential temperature perturbation (K) (strength of the cold air pool) between CONTROL and NOFLUX experiments.

	1 hour	2 hour	3 hour	4 hour	5 hour	6 hour
Control	-4.8	-4.3	-6.5	-6.2	-7.7	-7.8
NOFLUX	-5.5	-5.7	-8.6	-6.5	-6.4	-4.3

The simulated cumulative rainfall distribution at 2h, 3h, 3h and 4h of model integration for NOFLUX experiment is shown in Figures 2.17 a, b, c and d respectively. The maximum simulated cumulative rainfall at 2h and 3h are not much different from the CONTROL experiment (Figure 2.4), but at 4h the maximum rainfall decreases in the NOFLUX case. This decreasing tendency in rainfall continues at 5h of model integration as well probably due to lack of evaporation in the model simulation.

2.6. Conclusions

The 3-D simulation of the Feb 22 1993 TOGA COARE squall line reproduced the main observed characteristics of the squall line. Sensitivity experiments show that the orientation of the initial potential perturbation in the model can affect the simulation of the development of the squall line. The initial potential perturbation without a realistic orientation results in slower development of the squall line. The strength of the initial potential perturbation does not appear to influence the structure and evolution of the convective system. Inclusion ofthe ice microphysics affects the

strength and extent of the simulated downdraft induced low-level cold air pool. Also, the inclusion of the surface fluxes is important to simulate the evolution of the squall line.

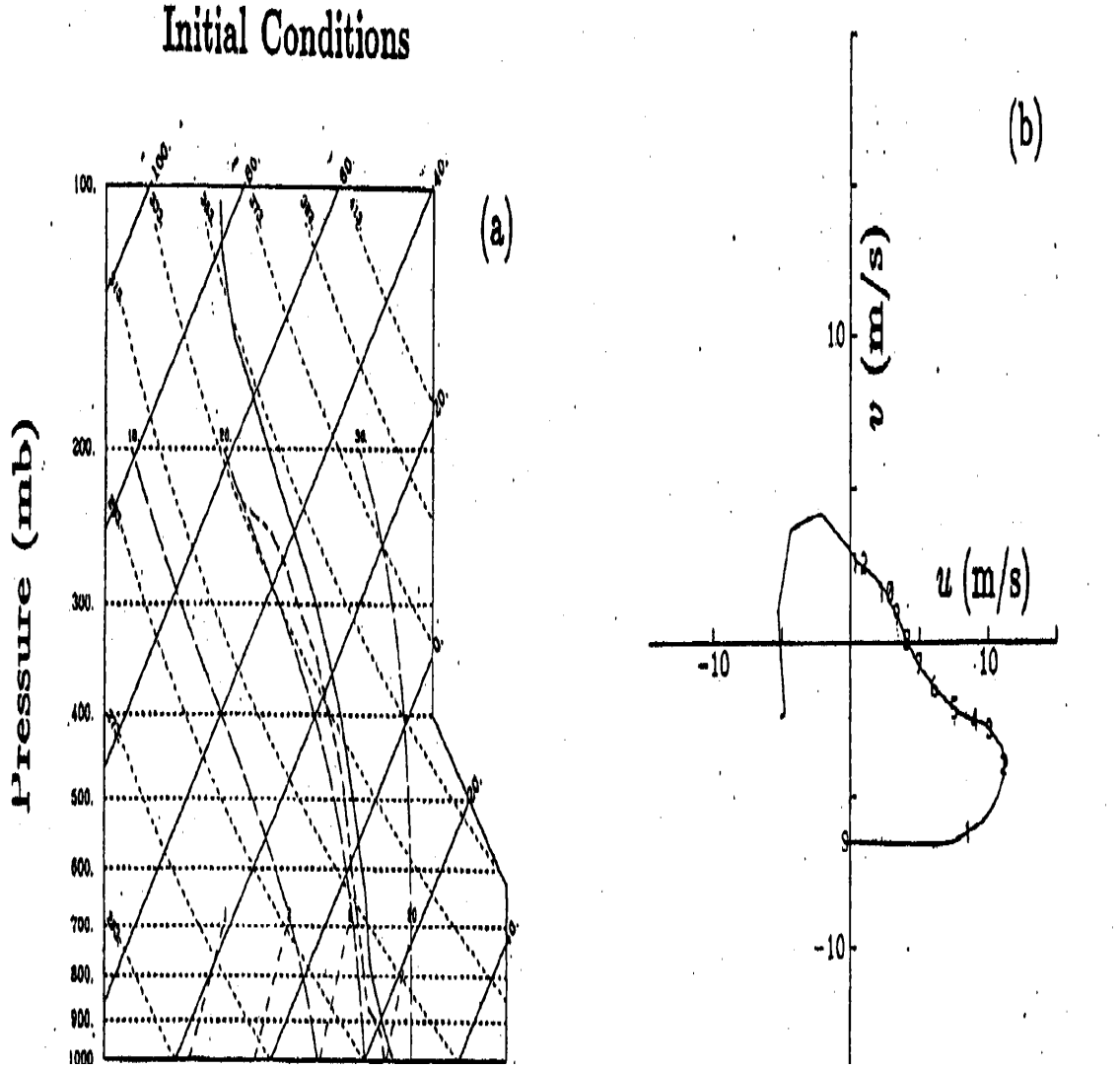

Figure 2.1. Vertical profile of potential temperature(a) and horizontal wind (U and V) (b) used for the initialization of the model. The altitudes (in Km) of the wind are indicated in (b).

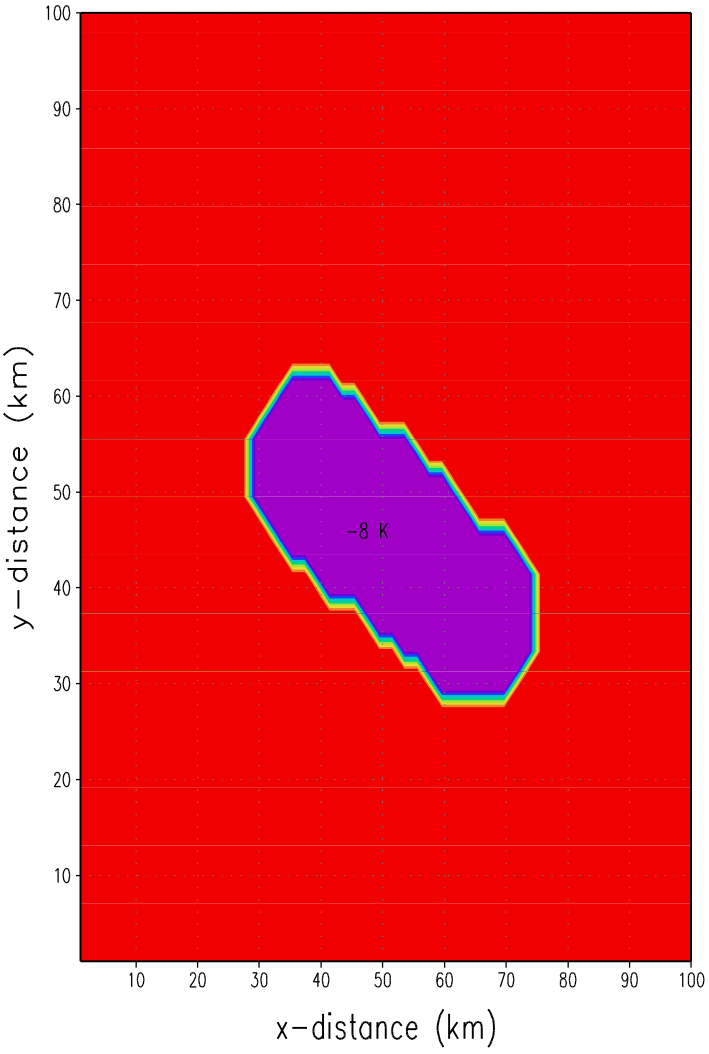

Figure 2.2. Initial potential temperature perturbation for the simulation

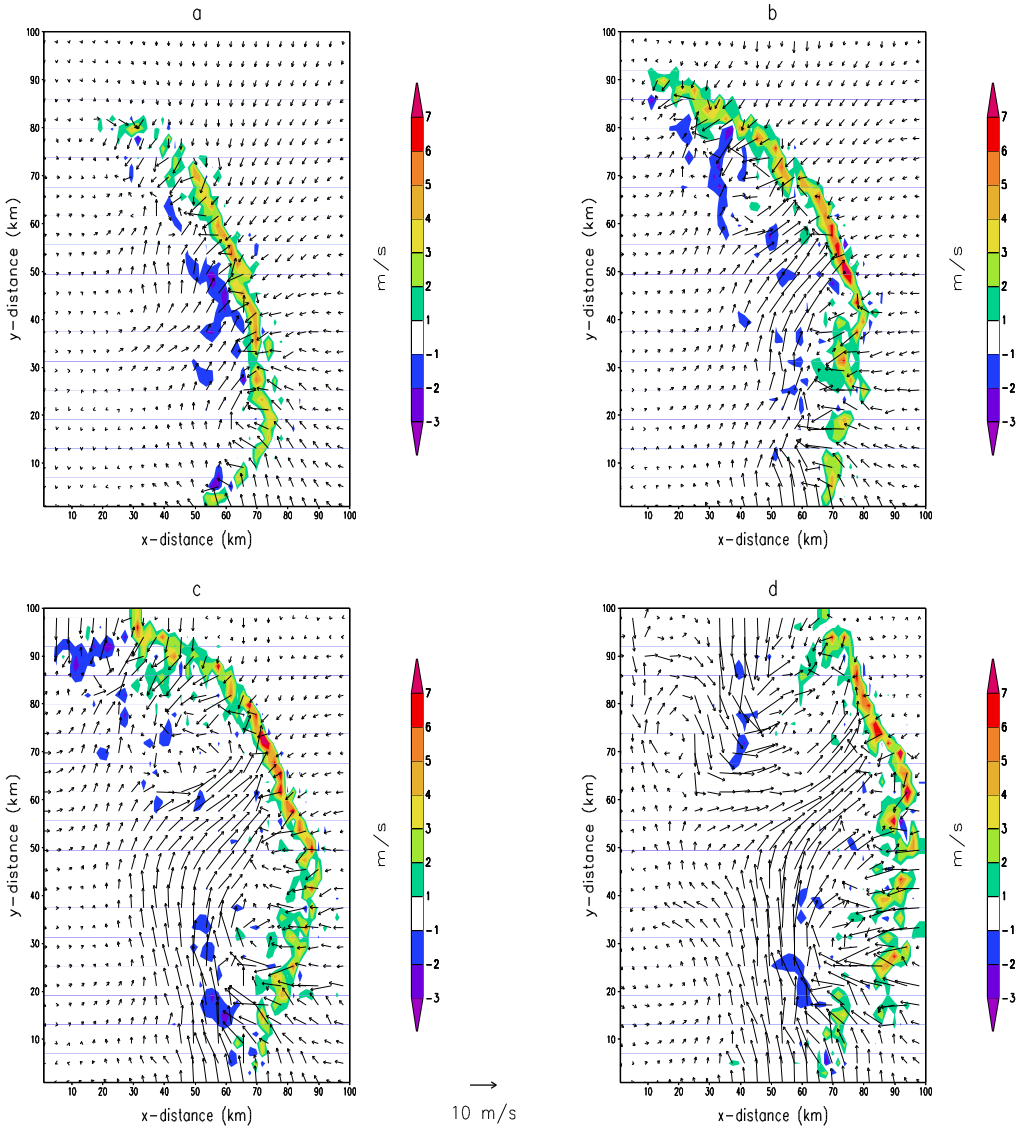

Figure 2.3. Vertical velocity (m/s) shown as shaded contours, and the system relative horizontal wind field (m/s) shown as vectors at the altitude of 1.5km for the CONTROL experiment at (a) 2h (b) 3h (c) 4h (d) 5h integration times. Notice the bow shape squall line with two vortices in its leading edges and the presence of a rear inflow jet.

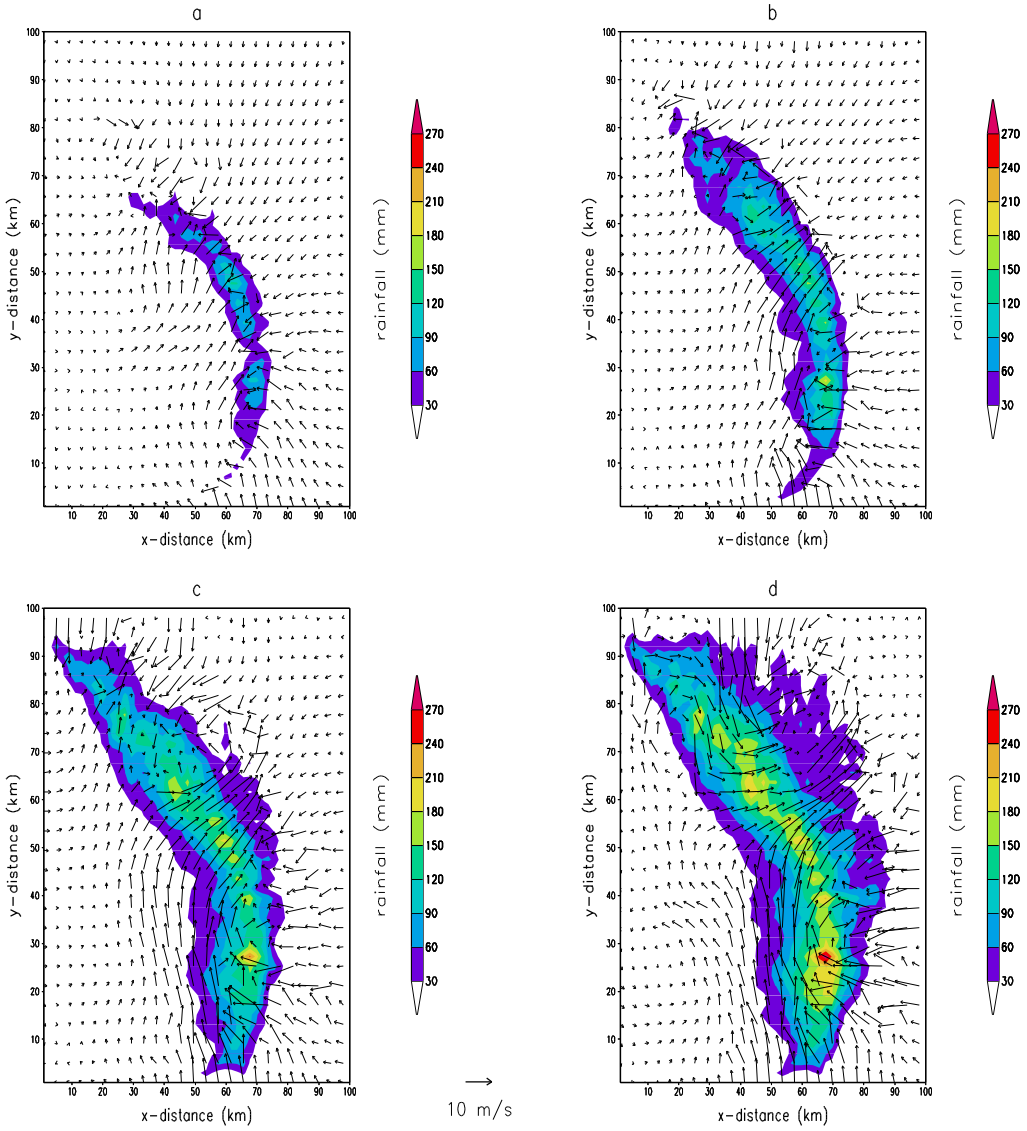

Figure 2.4. Rainfall (mm) shown as shaded contours and the system relative horizontal wind field (m/s) shown as vectors at the altitude of 1.5km in CONTROL experiment at (a) 2h (b) 3h (c) 4h (d) 5h integration times Notice that the rainfall occurs behind the leading edge of the simulated squall line system.

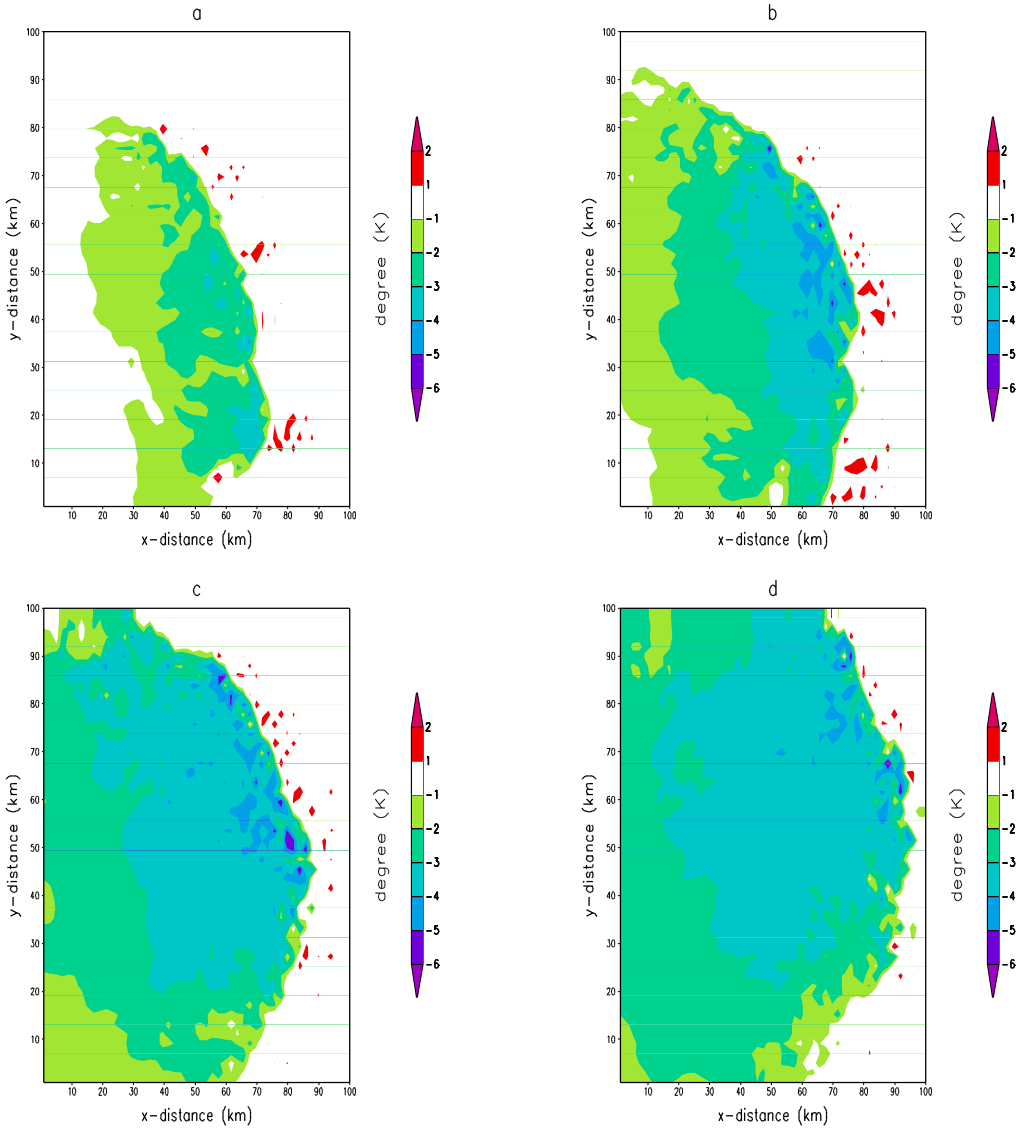

Figure 2.5. Potential temperature perturbation (K) shown as shaded contours at the altitude of 150m associated with the cold air pool resulting from the downdraft associated with the precipitation in CONTROL experiment at (a) 2h (b) 3h (c) 4h (d) 5h integration times. Notice that the leading edge of the simulated cold air pool and that of the updrafts are coincident.

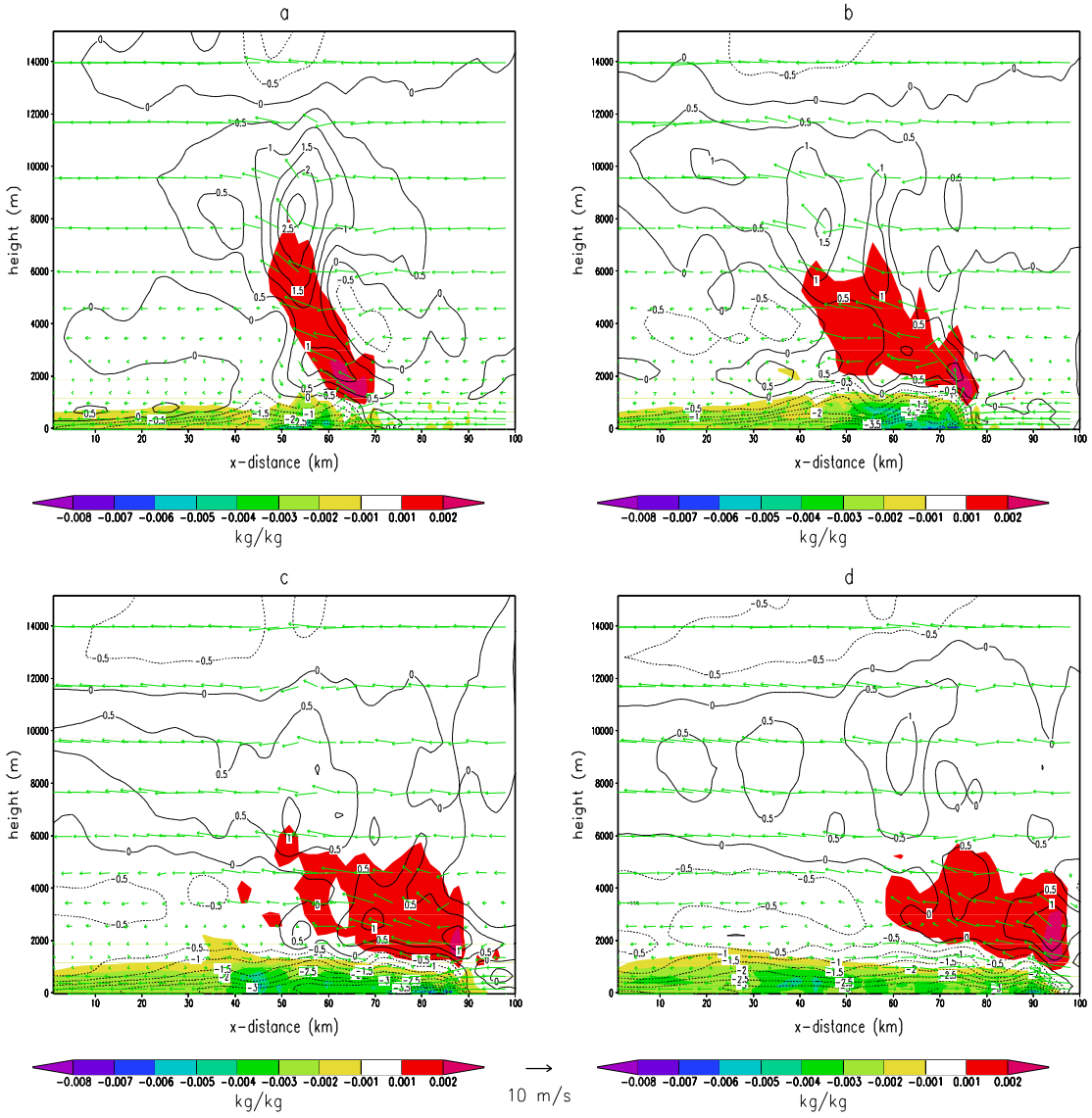

Figure 2.6. Vertical cross section of the potential temperature perturbation (K) shown as contours, moisture perturbation (kg/kg) shown as shaded contours and U-W vectors (m/s) in CONTROL experiment at (a) 2h (b) 3h (c) 4h (d) 5h integration time Notice the vertical tilting structure of the convection and the presence of cold air pool near the surface.

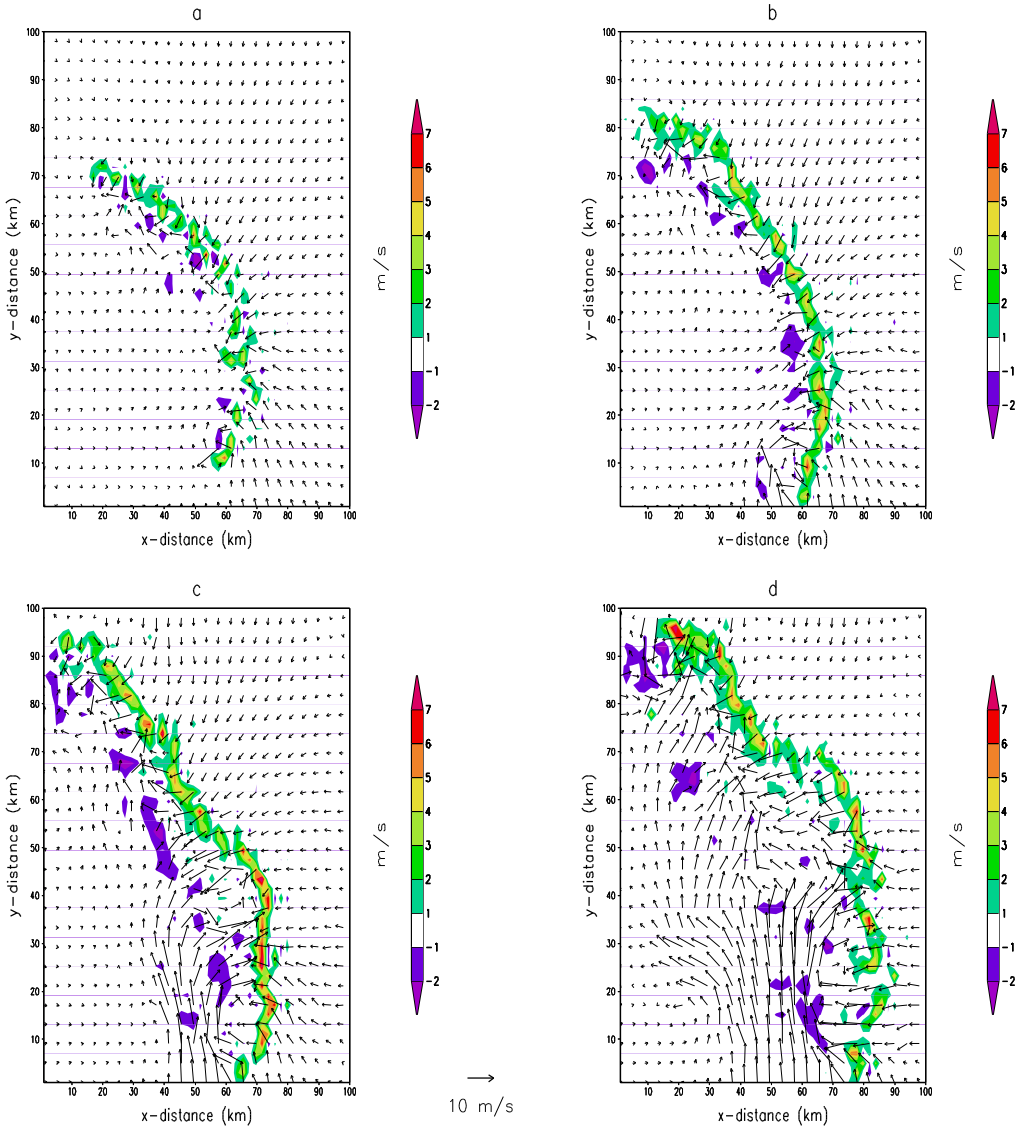

Figure 2.7. Vertical velocity (m/s) shown as shaded contours, and the system relative horizontal wind field (m/s) shown as vectors at the altitude of 1.5km for the WEAK-PTPRT experiment at (a) 2h (b) 3h (c) 4h (d) 5h integration times There is no significant difference in the structure of the simulated squall line between WEAK-PTPRT experiment and CONTROL experiment (Figure 2.3).

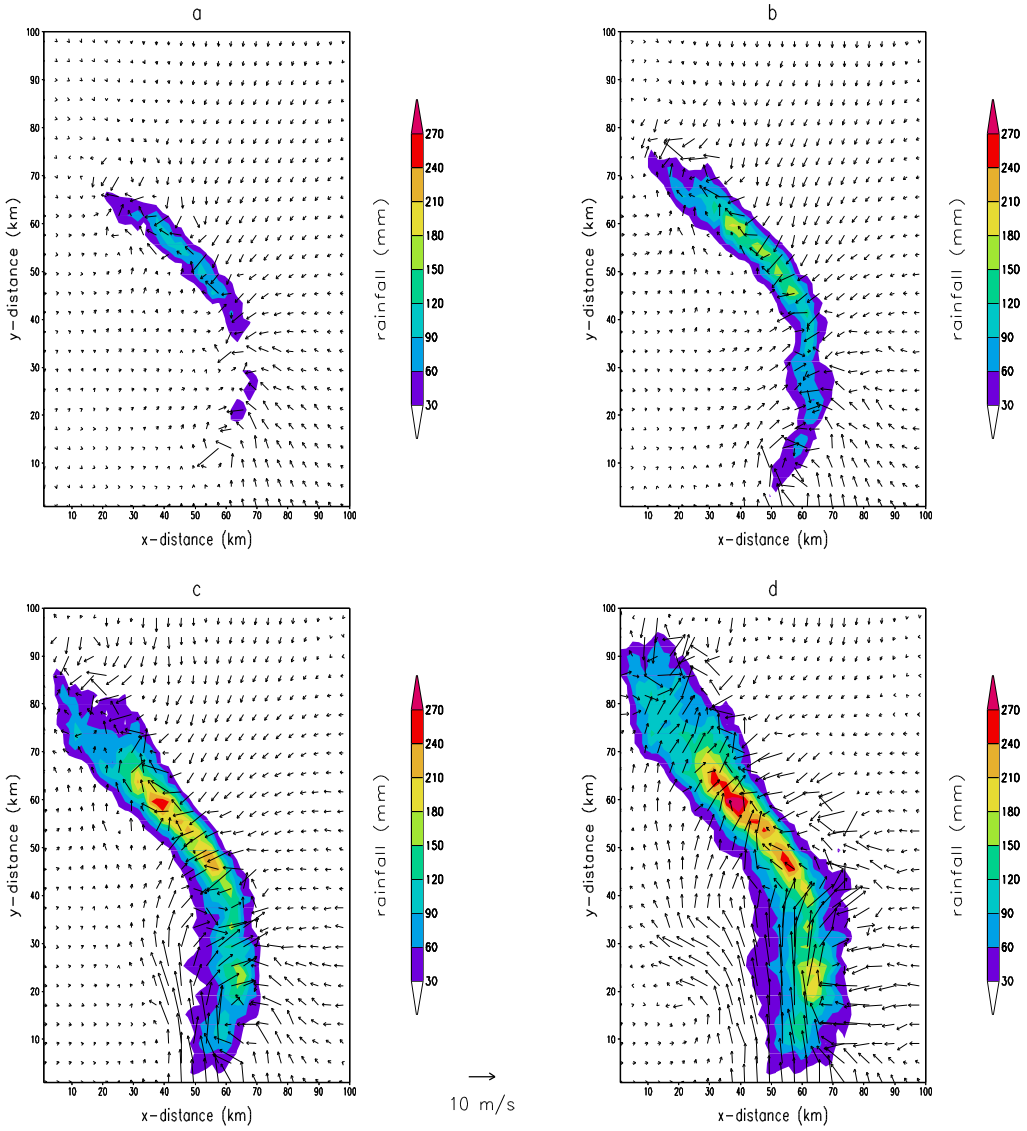

Figure 2.8. Rainfall (mm) shown as shaded contours and the system relative horizontal wind field (m/s) shown as vectors at the altitude of 1.5km in WEAK-PTPRT experiment at (a) 2h (b) 3h (c) 4h (d) 5h integration times. There is no significant difference in the simulated rainfall amount between WEAK-PTPRT experiment and CONTROL experiment (Figure 2.4).

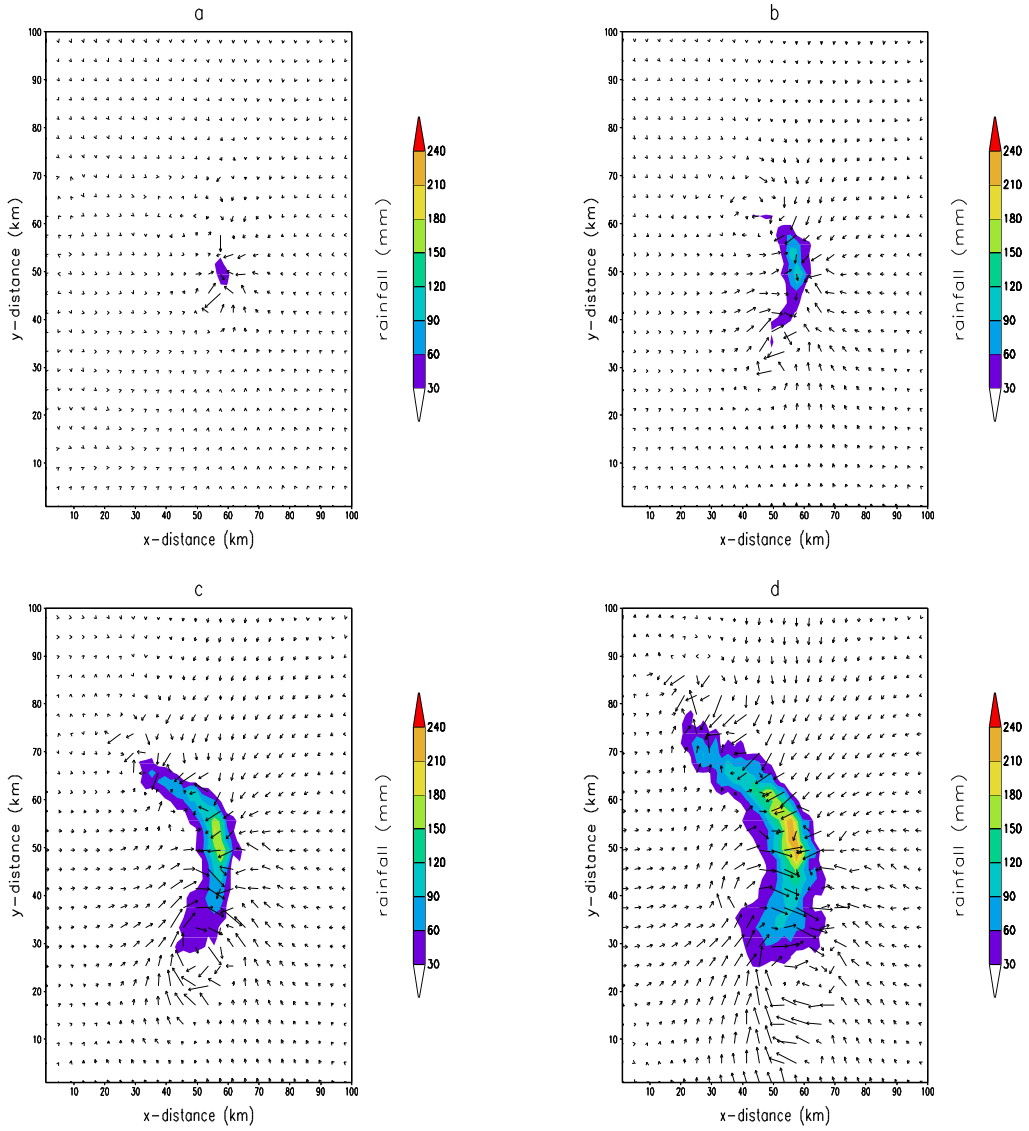

Figure 2.9. Rainfall (mm) shown as shaded contours and the system relative horizontal wind field (m/s) shown as vectors at the altitude of 1.5km in N-S experiment at (a) 2h (b) 3h (c) 4h (d) 5h integration times It takes longer for the convective line to transform from linear to bow shape in N-S experimentas compared to CONTROL experiment (Figure 2.3) and that the rainfall amount in N-S experiment is much smaller than that in CONTROL experiment (Figure 2.4).

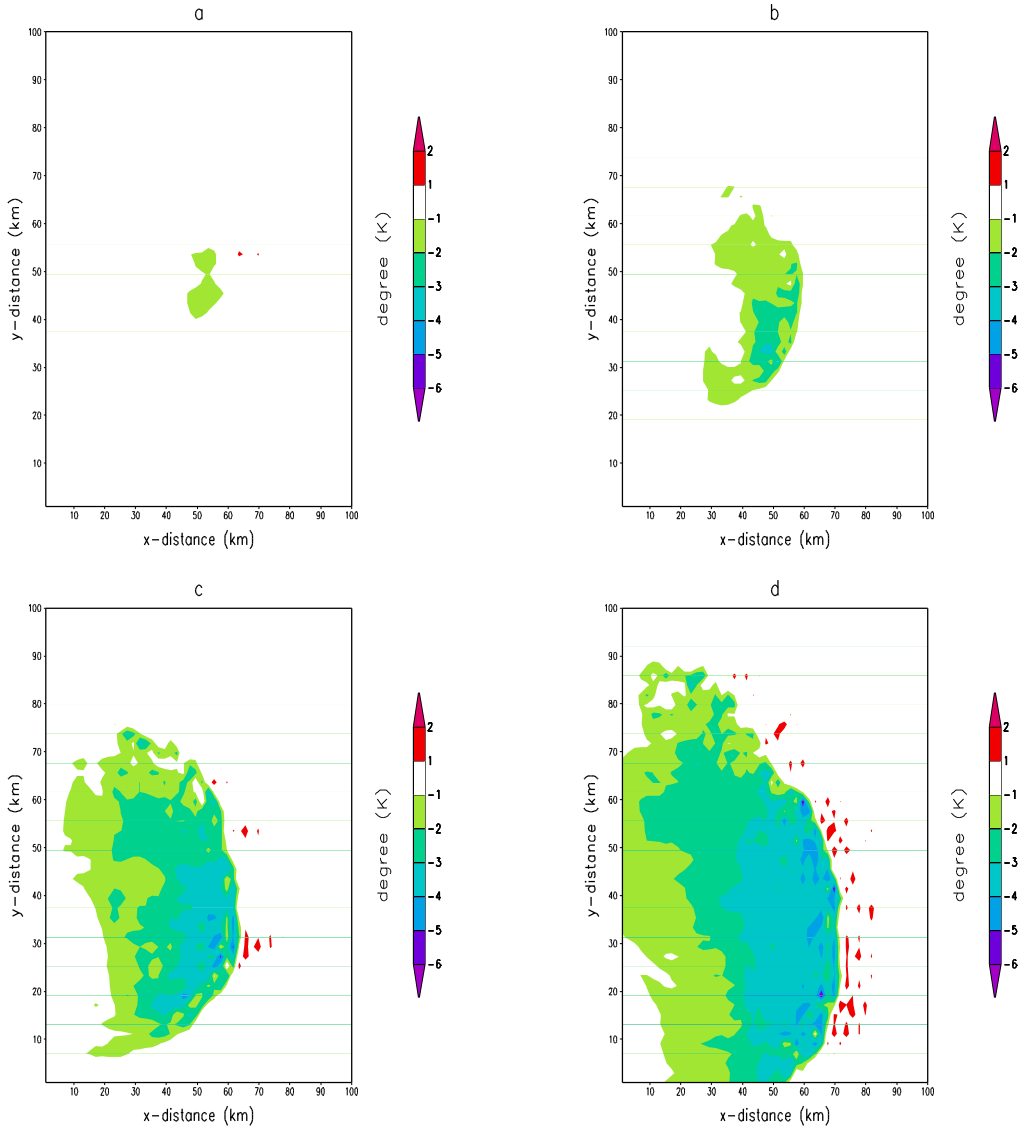

Figure 2.10 Potential temperature perturbation (K) shown as shaded contours at the altitude of 150m associated with the cold air pool resulting from the downdraft associated with the precipitation in NS experiment at (a) 2h (b) 3h (c) 4h (d) 5h integration times. The cold air pool in NS experiment is weak and covers a smaller region as compared to CONTROL experiment (Figure 2.5).

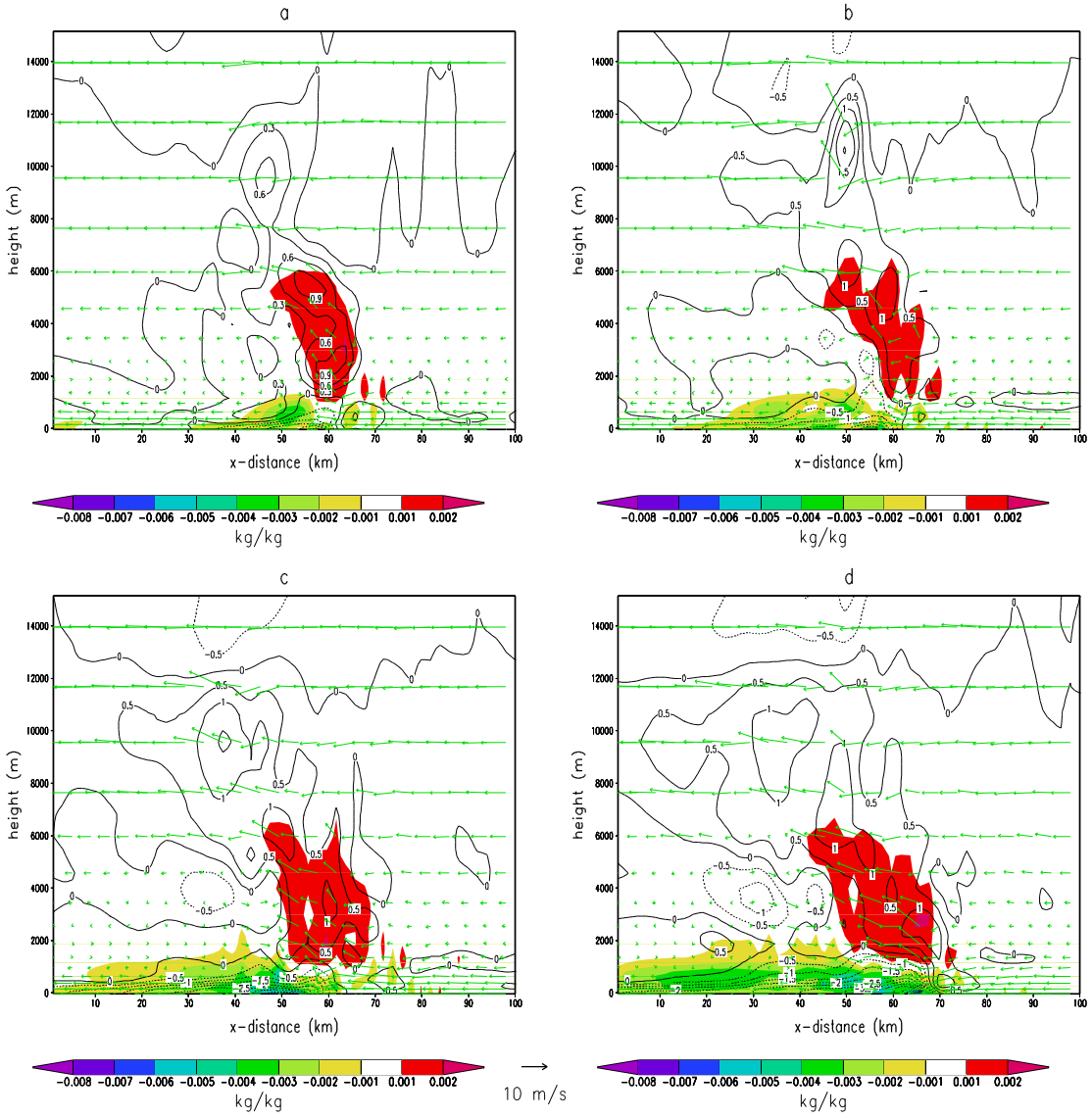

Figure 2.11. Vertical cross section of the potential temperature perturbation (K) shown as contours, moisture perturbation (kg/kg) shown as shaded contours and U-W vectors (m/s) in N-S experiment at (a) 2h (b) 3h (c) 4h (d) 5h integration times. The cold air pool in N-S experiment is weaker than that in CONTROL experiment (Figure 2.6).

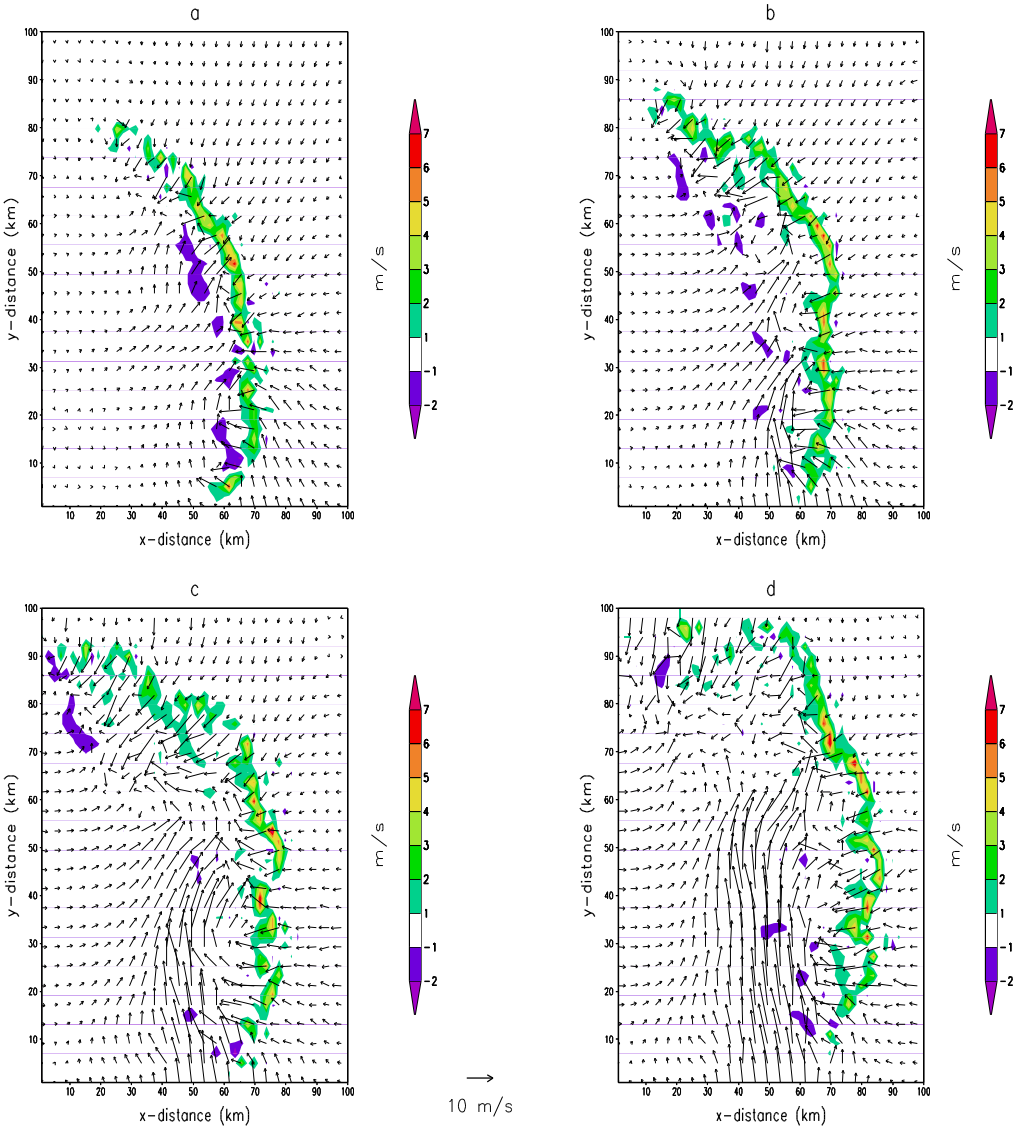

Figure 2.12. Vertical velocity (m/s) shown as shaded contours, and the system relative horizontal wind field (m/s) shown as vectors at the altitude of 1.5km for the NOICE experiment at (a) 2h (b) 3h (c) 4h (d) 5h integration times. There is no significant difference in the structure of the simulated squall line between NOICE experiment and CONTROL experiment (Figure 2.3).

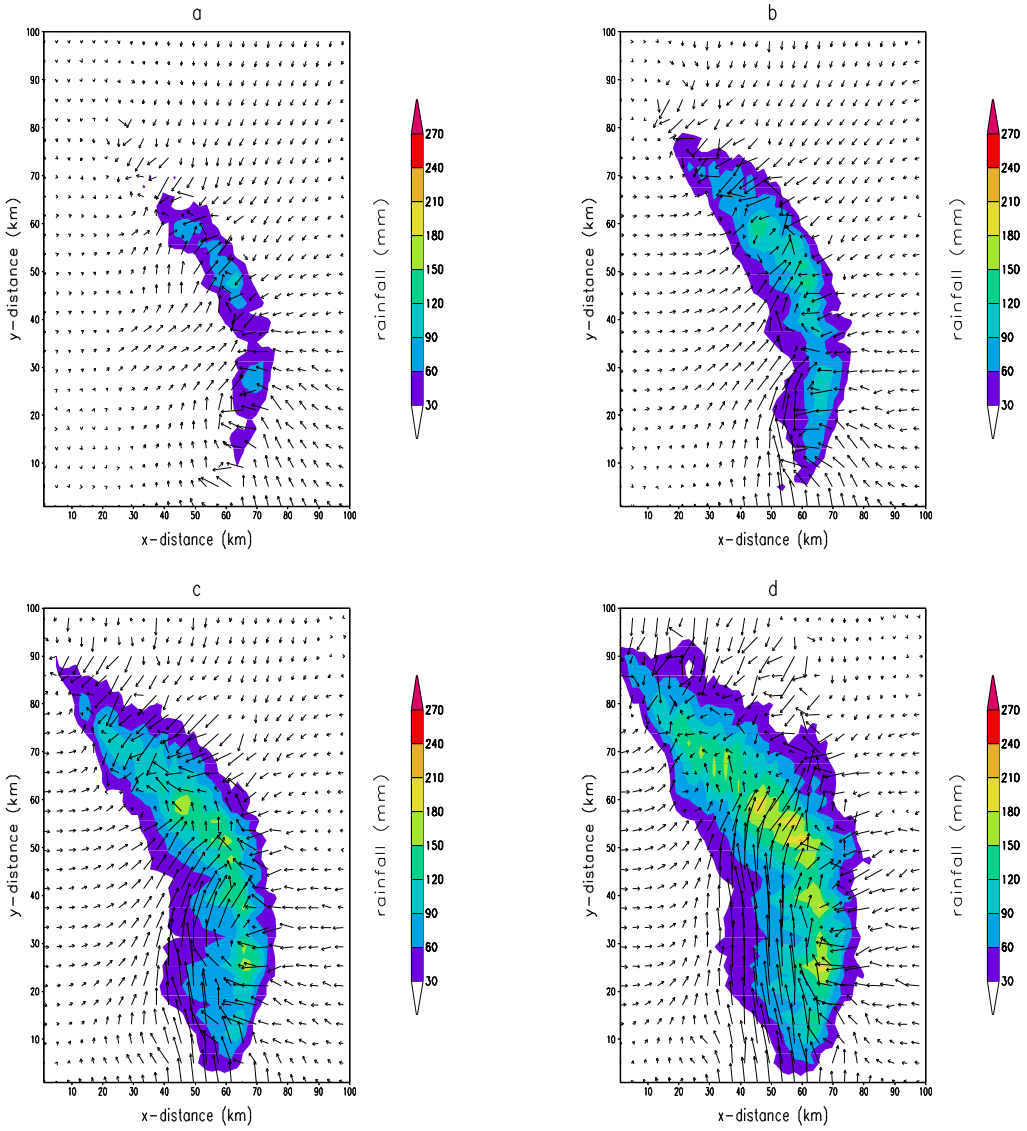

Figure 2.13. Rainfall (mm) shown as shaded contours and the system relative horizontal wind field (m/s) shown as vectors at the altitude of 1.5km in NOICE experiment at (a) 2h (b) 3h (c) 4h (d) 5h integration times. There is no significant difference in the distribution of rainfall between NOICE experiment and CONTROL experiment.

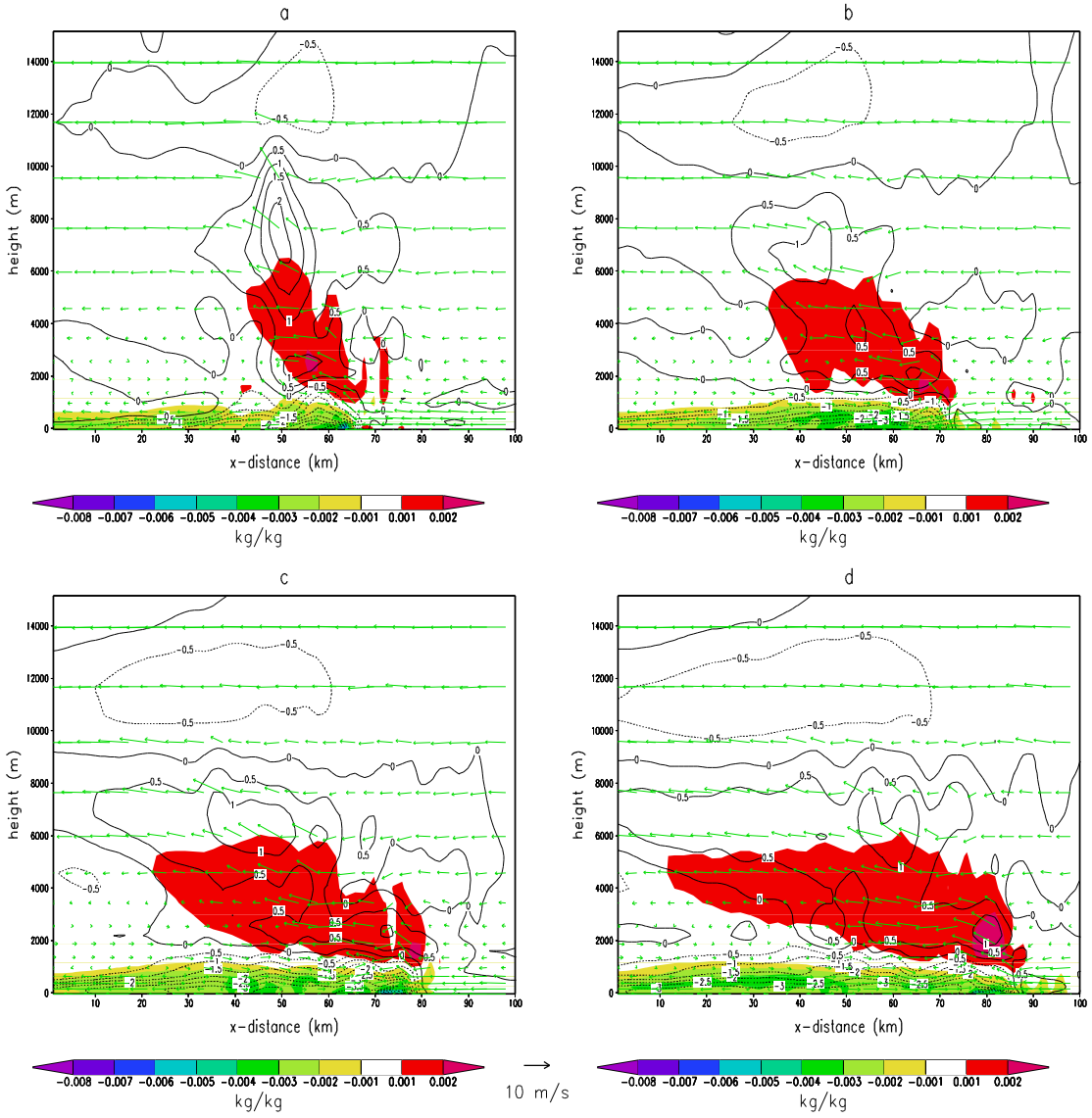

Figure 2.14. Vertical cross section of the potential temperature perturbation (K) shown as contours, moisture perturbation (kg/kg) shown as shaded contours and U-W vectors (m/s) in NOICE experiment at (a) 2h (b) 3h (c) 4h (d) 5h integration times The exclusion of ice and snow leads to a shallow cold air pool near the surface.

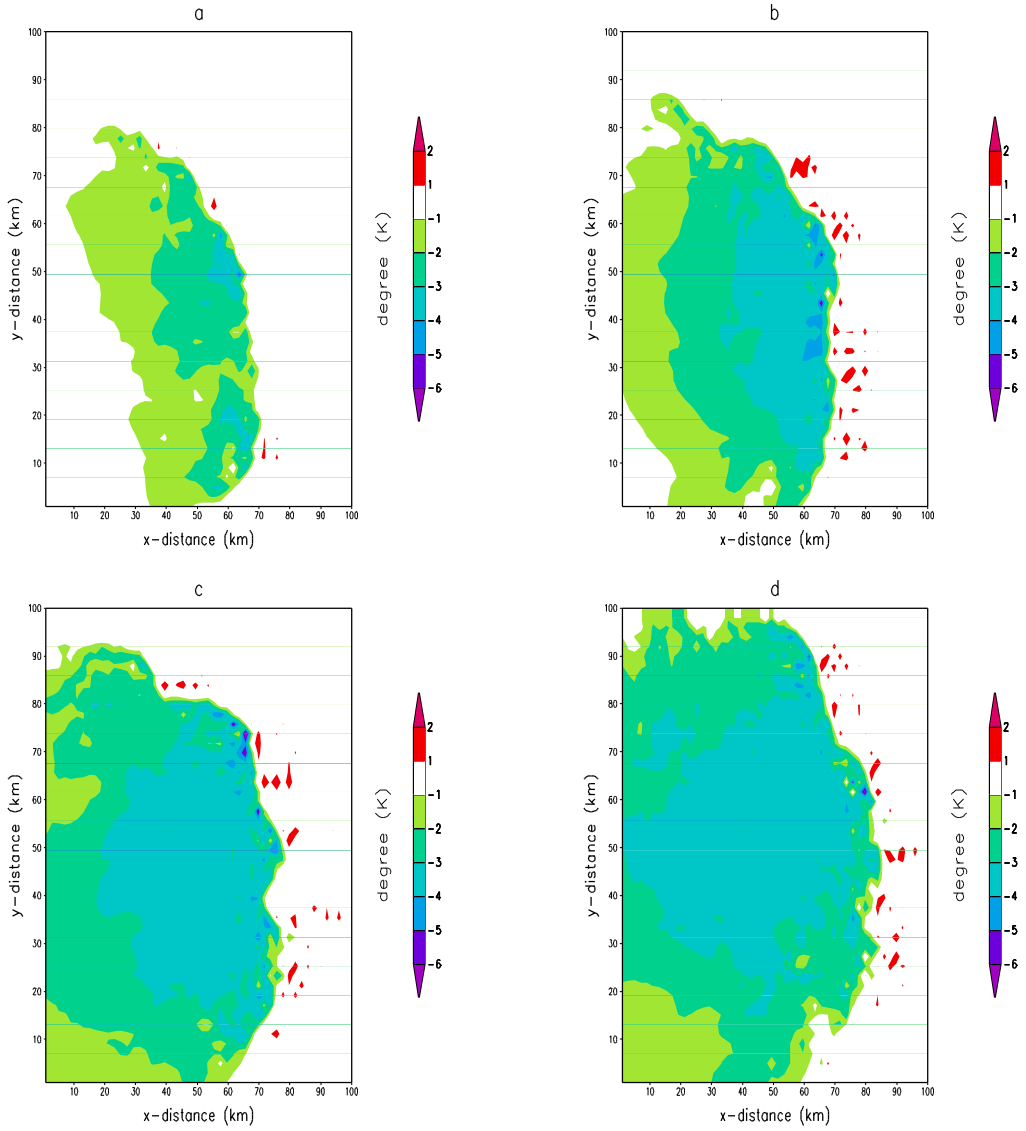

Figure 2.15 Potential temperature perturbation (K) shown as shaded contours at the altitude of 150m associated with the cold air pool resulting from the downdraft associated with the precipitation in NOICE experiment at (a) 2h (b) 3h (c) 4h (d) 5h integration times. The leading edge of cold air pool moves slower than in CONTROL experiment.(Figure 2.5)

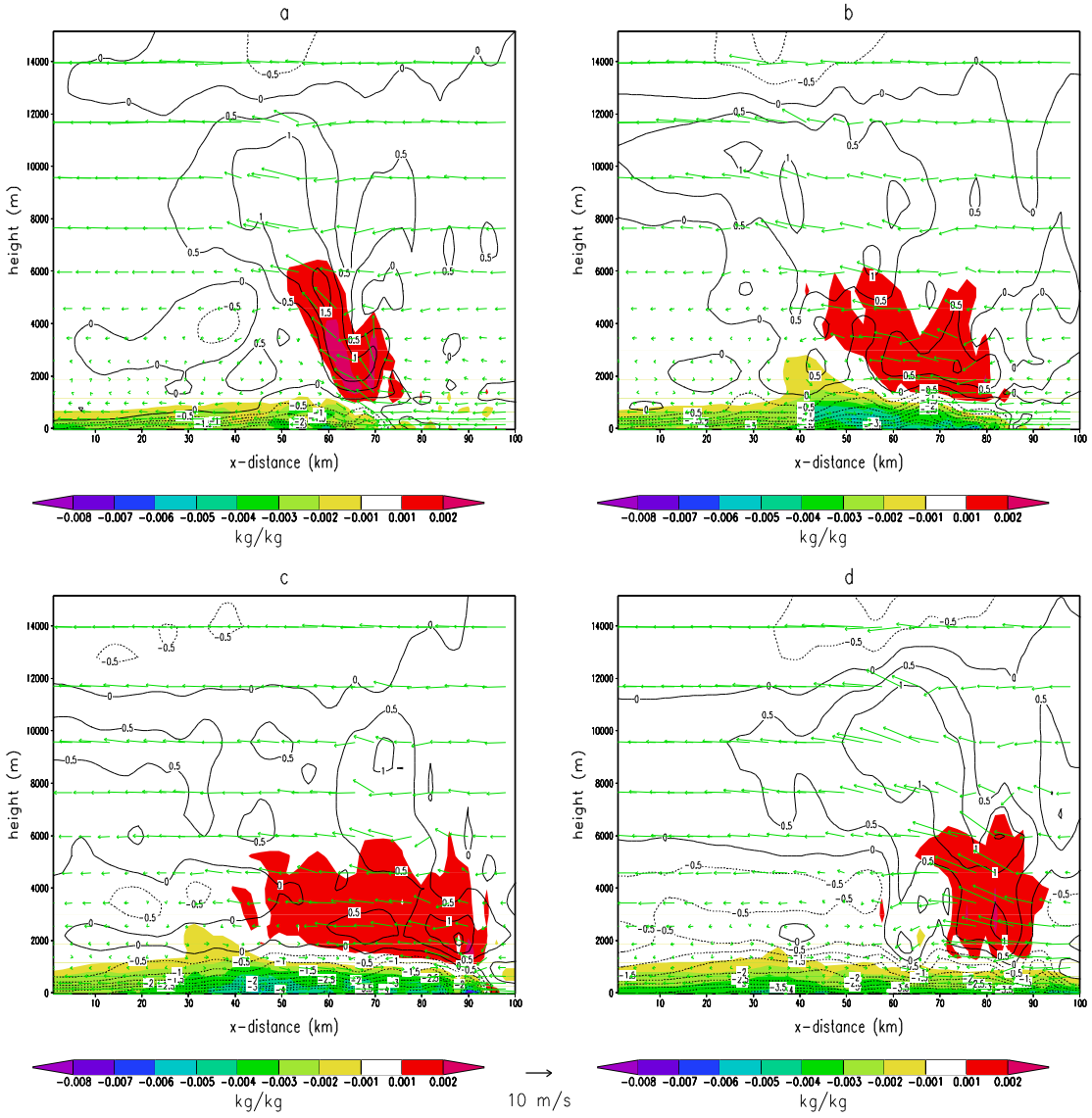

Figure 2.16. Vertical cross section of the potential temperature perturbation (K) shown as contours, moisture perturbation (kg/kg) shown as shaded contours and U-W vectors (m/s) in NOFLUX experiment at (a) 2h (b) 3h (c) 4h (d) 5h integration times Exclusion of surface fluxes leads to stronger cold air pool than in CONTROL experiment (Figure 2.6).

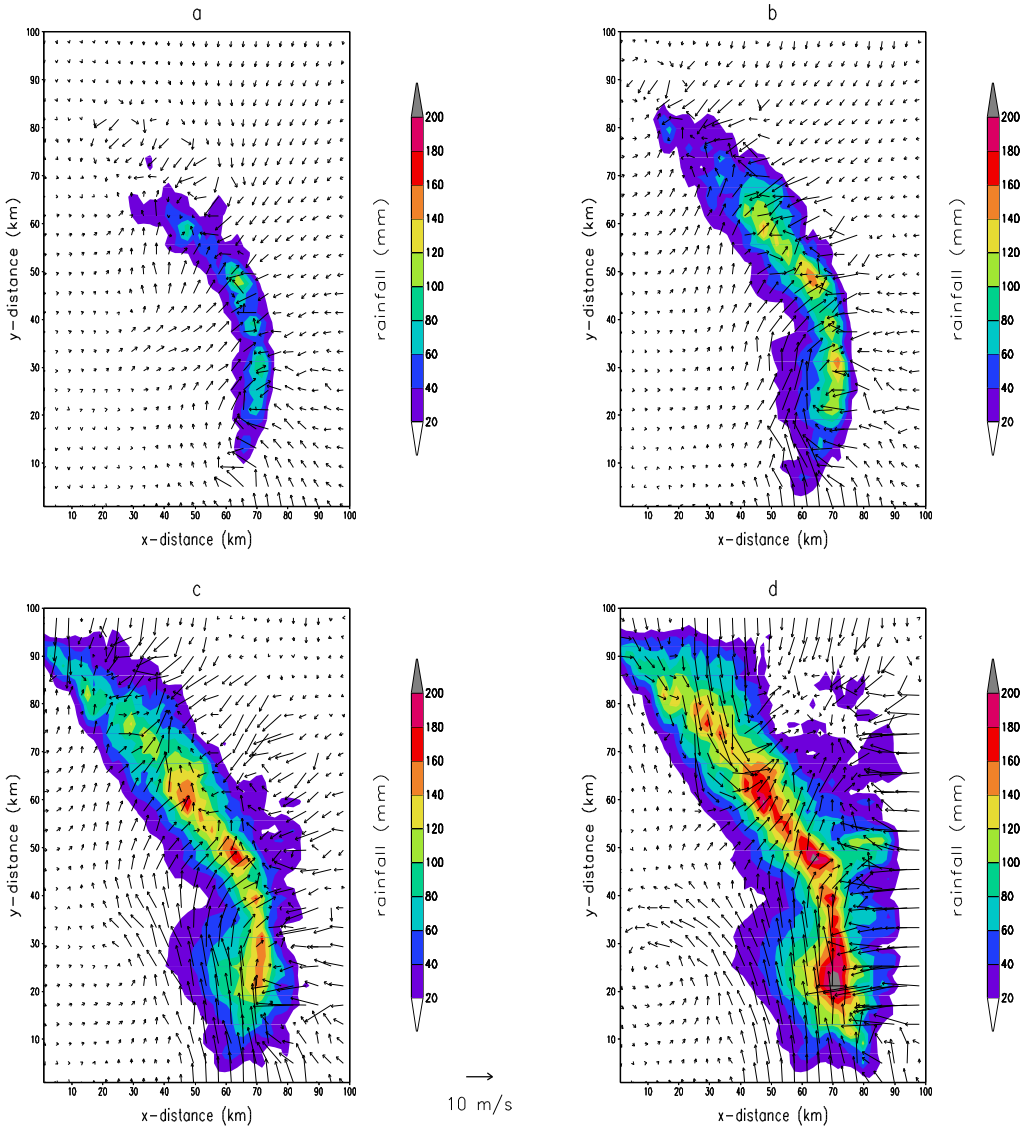

Figure 2.17. Rainfall (mm) shown as shaded contours and the system relative horizontal wind field (m/s) shown as vectors at the altitude of 1.5km in NOFLUX experiment at (a) 2h (b) 3h (c) 4h (d) 5h integration times The rainfall amount in NOFLUX experiment is less as compared to CONTROL experiment (Figure 2.4).

Chapter 3. NUMERICAL SIMULATION OF THE RESPONSE OF THE OCEAN SURFACE LAYER TO PRECIPITATION

3.1. Introduction

The region of the tropical western Pacific that has SST higher than 28^{o}C is called the western Pacific warm pool. Because of the high SST, the western Pacific warm pool supplies the atmosphere a large amount of heat and moisture that result in substantial annual tropical precipitation. Western Pacific warm pool is a product of regional air-sea interaction and it plays an important role in the global seasonal and inter-annual climate variability such as El Niño and Southern Oscillation (ENSO). Easterly trade winds prevail over most of the western equatorial Pacific. However during boreal winters and springs the easterly trade winds are often interrupted by strong westerly wind bursts (WWB), lasting from a couple of days to two or three weeks. In recent years, the WWBs and their impacts, both local and remote, have been investigated extensively (Zhang *et al*. 1998, Richardson *et al*. 1999). It has been suggested that the WWB can generate eastward propagating Kelvin waves, an important factor in the eastern Pacific warming during El Niño events. As for the local response, it is believed that the WWB could cause the eastward surface jet (Yoshida, 1959). Observations have shown that the eastward surface jet is often

accompanied by a significant subsurface westward current. During TOGA COARE IOP (Intensive Observation Period) experiment, subsurface westward currents (SSWC) were observed during strong WWB episodes.

The importance of air-sea interaction in seasonal to interannual climate prediction is well documented. However, the air-sea coupled processes and their role in mesoscale to synoptic scale weather prediction on time scales from hours to days over the western Pacific warm pool are not well understood. Mesoscale air-sea interaction processes are important in regions with intense convection such as the western Pacific warm pool (Sui *et al.* 1997).

It is apparent that the ocean and the atmosphere in the tropics communicate on the mesoscale. However, the physical mechanisms are not well understood yet. The progress was limited by the lack of high quality measurements of air-sea fluxes of heat, moisture, and momentum in the warm pool region as well as by the difficulty encountered by coupled models in simulating the air-sea interaction processes over the western Pacific warm pool. In order to achieve a better understanding of the air-sea interaction processes over the western Pacific warm pool both the availability of high quality measurements and the improvement of air-sea coupled models are necessary. The TOGA/COARE (Tropical Ocean-Global Atmosphere/Coupled Ocean-Atmosphere Response Experiment) was conducted from 1992 to 1993 over the western Pacific warm pool (Webster and Lukas, 1992). One of its main objectives was to describe and understand the principal processes responsible for the coupling of the ocean and the atmosphere in the western Pacific warm pool system. Data collected during the experiment provided investigators with information for a better

understanding of the air-sea interaction processes in the warm pool. However the development of the fully air-sea coupled models and the numerical experiments of the coupled processes are still limited. It is well known that there is a lag in the ocean's response to the atmospheric forcing. Therefore, a valid question is as to how important the mesoscale air-sea interaction processes are when the ocean's response time scale is much larger than that of the atmospheric forcing.

Our hypothesis is that the precipitation-induced low salinity stable layer may play an important role in the mesoscale air-sea interaction processes. This stable layer tends to isolate the rest of the mixed layer from the surface atmospheric forcing. Consequently, downward transfer of the effects of the surface atmospheric forcing (momentum, heat and freshwater fluxes) is impeded by the stable surface layer and their effects effectively limited within the top few meters. Therefore, the thin top layer can respond more effectively to the surface atmospheric forcing.Thus the response could be significantly faster than it would be without the precipitation induced stable surface layer. Existence of the thin top layer in locations with rainfall can also induce mesoscale circulations due to horizontal gradients in sensible heat flux.

It has been observed that precipitation can cause the development of a fresh stable layer at the surface (Price 1979, Wijesekera *et al.* 1999). Smyth *et al.* (1997) observed that associated with this low salinity layer, there is a rapid attenuation of the turbulence below this stable layer; However, the turbulence increases in the precipitation-induced stable layer near the surface. The authors suggested that the turbulence production continues, and the vertical turbulent flux of theturbulent

kinetic energy (TKE) is substantially reduced, leading to the decay of the turbulence below the surface precipitation-induced stable layer.

Observations reveal several features of the precipitation-induced fresh stable layer. However, most of the observations were made after the precipitation stopped, and therefore cannot describe the ocean's response during the precipitation. The sampling of rain rates is often made along a track, and thus provides only a one-dimensional description of the oceanic response. Three-dimensional numerical simulation is needed to investigate the temporal and spatial variations of the ocean's response to precipitation.

In this study, three-dimensional numerical simulations of the ocean's response to the westerly wind burst and precipitation are conducted. The simulation resultsare compared to the observations. The difference in the ocean's response with and without precipitation is investigated. The mechanism by which the atmospheric forcing changes the upper ocean turbulent mixing process is analyzed.

3.2. Model description

POM (Princeton Ocean Model) is used in this study. Developed at the Princeton University, it contains an imbedded second moment turbulence closure model to provide vertical mixing coefficients. It is a sigma coordinate model in that the vertical coordinate is scaled by the water column depth. $s = \frac{z-h}{H+h}$ is the vertical coordinate. z is the conventional Cartesian vertical coordinate. $D \equiv H + h$ where H is the bottom topography that is constant in this study and h is the surface elevation. The horizontal time differencing is explicit whereas the vertical differencing is implicit. The latter eliminates time constraints for the vertical coordinate and permits the use of fine vertical resolution in the surface and bottom boundary layers. The model has a free surface and a split time step. The external mode portion of the model is two-dimensional and uses a short time step based on the CFL condition and the external wave speed. The internal mode is three-dimensional and uses a larger time step based on the CFL condition and the internal wave speed. Complete thermodynamics have been implemented. Details of the model are described by Blumberg *et al*. (1987) and Kantha *et al*. (2000).

The finest horizontal resolution of this simulation is 10 km. A stretching vertical grid scheme is used. Higher vertical resolution is used for the upper layers because the ocean's response to the surface atmospheric forcing such as precipitation associated with squall lines, which last only a few hours, occurs mainly in the upper few meters of the ocean. Below 50 meters, the ocean's response is not significant. In this study,

the finest vertical resolution, at the upper-most layer, is about one meter. The external mode time step is 20 seconds, and the internal mode has a time step of 600 seconds.

We assume that the initial temperature and salinity profiles are horizontally homogeneous and the ocean is initially calm with no motion. The temperature and salinity profiles are based on a global data set (Levitus *et al*., 1994; Levitus and Boyer, 1994). February monthly average data at 165 ^{o} E and 5 ^{o} N is used. This location is the center of thesimulation domain.

The parameterization of the turbulent mixing processes is critical in the simulation of the upper ocean boundary layer response to the atmospheric forcing. The second moment turbulent closure model included in POM, often cited in the literature as the Mellor-Yamada turbulent closure model (Mellor and Yamada, 1974,1982), is widely used in geophysical fluid studies because it is relatively simple and still retains much of the second moment accuracy.

Turbulent kinetic energy (TKE) and turbulent mixing length are predicted using the following equations:

$$\frac{\partial q^2 D}{\partial t} + \frac{\partial U q^2 D}{\partial x} + \frac{\partial V q^2 D}{\partial y} + \frac{\partial w q^2 D}{\partial s} = \frac{\partial}{\partial s}\left[\frac{K_q}{D}\frac{\partial q^2}{\partial s}\right] + \frac{2K_m}{D}\left[\left(\frac{\partial U}{\partial s}\right)^2 + \left(\frac{\partial V}{\partial s}\right)^2\right] + \frac{2g}{\rho_0} K_\rho \frac{\partial \tilde{\rho}}{\partial s} - \frac{2Dq^3}{B_1 l} + F_q \qquad \textbf{(3.1)}$$

$$\frac{\partial q^2 l D}{\partial t} + \frac{\partial U q^2 l D}{\partial x} + \frac{\partial V q^2 l D}{\partial y} + \frac{\partial w q^2 l D}{\partial s} = \frac{\partial}{\partial s}\left[\frac{K_q}{D}\frac{\partial q^2 l}{\partial s}\right] + E_1 l\left\{\frac{K_m}{D}\left[\left(\frac{\partial U}{\partial s}\right)^2 + \left(\frac{\partial V}{\partial s}\right)^2\right] + E_3 \frac{g}{\rho_0} K_\rho \frac{\partial \tilde{\rho}}{\partial s}\right\} W - \frac{2Dq^3}{B_1} + F_l \qquad \textbf{(3.2)}$$

where $g = 9.8\ \mathrm{m\,s^{-2}}$, q^2 is the turbulent kinetic energy (TKE). l is the turbulent length scale and w is the velocity component normal to the sigma surface. $\tilde{W} = 1 + E_2(l/kL)$, where von Karman constant $k = 0.4$, $L^{-1} = (h - z)^{-1} + (H - z)^{-1}$. $\partial \tilde{r} / \partial s \equiv \partial(r\,\partial / s -)\ (c_s^{-2}\ \partial p / s\ )$ where c_s is the speed of sound. *B1, E1, E2* and E_3 are constants. *U* and *V* are zonal and meridional velocities. F_q and F_l are diffusion terms of q^2 and *l*, respectively.

The vertical kinematic viscosity and vertical diffusivity, K_m and K_h, are defined according to

$$K_m = qlS_m \tag{3.3}$$

$$K_h = qlS_h \tag{3.4}$$

The coefficients, S_m and S_h are functions of Richardson number and K_q is the TKE diffusivity.

During westerly Wind Burst events, the winds over western Pacific warm pool are mainly zonal. Impact of the meridional wind stress is relatively small compared to the zonal ones (Harrison and Craig, 1993). Therefore, in this study, only idealized zonal wind stress is used. The wind stress field is imposed in the following form (Figure 3.1):

$$t(x, y) = ramp \cdot t_0 \cdot \exp(-(x - x_0 \Delta x)^2) \exp(-(y - y_0 \Delta y)^2) \tag{3.5}$$

t_0 is the maximum amplitude of stress. The variable *ramp* varies from 0 to 1 within the first day of the simulation, so the wind stress is switched on at the

beginning of the simulation and is increased to its maximum strength within one day. Same value is then maintained for 10 days and then switched off. (x_0,y_0) is the center of the simulation domain. Δx and Δy are the horizontal grid sizes.

The rainfall-induced freshwater flux (F_s) and heat flux (F_t) are given by:

$$F_s = r I S_o \qquad (3.6)$$

$$F_t = r C_p I (T_a - T_0) \qquad (3.7)$$

where r is the water density, I is the rainfall intensity, S_0 is the surface salinity, C_p is specific heat of liquid water (4218 J K^{-1}/Kg), T_a is the atmospheric temperature and T_0 is the sea surface temperature.

In this study, an idealized precipitation process is considered. The rainfall-induced freshwater flux and heat flux are included. The rainfall has an intensity of 15 mm /hour and covers a region enclosed by a circle with a radius of 100 km (Figure 3.1). The precipitation process lasts for five hours.

3.3. Experiment Design

A total of five experiments are conducted to study the effect of precipitation on the upper ocean's response (Table 3.1). In Exp 3.1, the overall features of the Westerly Wind Burst (WWB) and precipitation are simulated with a horizontal

resolution of 60 km and a finest vertical resolution of 10m (top layer). The simulation domain is 9000 km x 3000 km, and the integration time 30 days. However, the effect of the rainfall on the ocean's response occurs mainly within the top few meters of the ocean. In order to investigate the rainfall-induced effects and their spatial variation, higher resolution numerical modeling is required. In Exp 3.2, Exp 3.3, Exp.3.4, and Exp 3.5, the horizontal resolution is 10 km and the finest vertical resolution within the upper ocean is 1 meter. The domain covers a region of 1000 km x 1000 km and the integration time is 24 hours in Exp 3.2, Exp 3.3, Exp 3.4, and Exp 3.5. Effects of the precipitation on the mixing processes of the upper ocean are investigated in Exp3.2 and Exp 3.3. Because the wind stress forcing remains after the formation of the rainfall-induced fresh layer, effects of the precipitation on the vertical transfer of the momentum is investigated. In Exp 3.4 and Exp 3.5, the effects of rainfall on the vertical transfer of heat flux contributed by short-wave radiation are investigated. In Exp 3.4 and Exp 3.5, the ocean receives a downward vertical heat flux of 200 W/m^2, a typical value for the location simulated in this study, due to the idealized short-wave radiation.

Table 3.1. Sensitivity experiments design for the oceanic responses to atmospheric forcing.

Experiment #	Horizontal Grid Resolution	Rainfall	Incoming Short-wave Radiation
3.1	Coarse (60 km)	Not included	Not included
3.2	Fine (10 km)	Not included	Not included
3.3	Fine (10 km)	Included	Not included
3.4	Fine (10 km)	Not included	Included
3.5	Fine (10 km)	Included	Included

3.4. Results

3. 4. 1. Experiment 1: General features of the ocean's response to the westerly wind burst

The wind stress generates an eastward surface Yoshida jet (Yoshida 1959) as indicated in Figure 3.2and Figure 3.3. Time series of the simulation results of the surface velocity fields in Exp 3.1 are shown in Figure 3.2. Time series of the simulation results of the surface zonal velocity, U (m/s), in Exp3.1 are shown in Figure 3.3. Positive values indicate eastward currents in Figure3.3. The wind stress is switched off on the 10^{th} day. The eastward jet increases to its maximum strength in about 10 days, then begins to decrease due to the switch-off of the wind stress. The maximum current reaches a value of 1.5 m/s.

The eastward jet causes meridional current, southward in the Northern hemisphere and northward in the southern hemisphereas shown in Figure 3.4. The meridional velocities also reach their maximums just after the wind stresses are switched off on the 10^{th} day of the simulation and then begin to decrease. Simulated maximum value of the meridional current is 0.35 m/s.

Vertical X-Z cross-section of zonal current U is shown in Figure 3.5. The momentum spreads from surface downward by two major processes: the mean vertical velocity transport and the turbulent flux. The turbulent flux process plays a greater role than the mean velocity transport. The eastward current causes a convergence zone on the leading edge and a divergence zone on the trailing edge. Because of mass continuity, the convergence and divergence caused by the surface eastward jet generate the subsurface westward jet (SSWJ) below the eastward jet. This feature agrees well with the observations (Hisard *et al.*, 1970) and with other simulations such as that by Zhang *et al.* (1998) using a general circulation model originally developed by Gent and Cane (1989).

When the surface wind stress is switched off on the 10th day, there is no energy source to drive the ocean surface current, so the surface eastward jet begins to weaken. However, the upwelling and downwelling, which are the energy sources of the SSWJ, still exist. Therefore, from Figure 3.5, it is apparent that the SSWJ did not begin to weaken immediately after the surface wind stress is switched off. It continues to increase, reaching its maximum on the 15th day, 5 days after the wind stress is switched off.

3. 4. 2. Sensitivity to Rainfall (Experiments 3.2 and 3.3)

The (X Z) vertical cross-section of the differences in the salinity and the potential temperature between the simulation results with and without rainfall (S_{rain}-S_{norain} and T_{rain}-T_{norain}, respectively) are shown in Figure 3.6 and Figure 3.7

respectively. It is clear that immediately after the precipitation process started, the negative salinity anomaly and negative temperature anomaly began to develop. The salinity anomaly and the potential temperature anomaly are limited in the region where the precipitation occurred. The magnitudes of the anomalies and the thickness of the rainfall-induced fresh layer kept increasing with time until the precipitation stopped. Then the precipitation-induced layer remains stable near the surface. The magnitudes of the salinity and potential temperature anomalies are the highest near the surface, and decrease with depth. The maximum salinity anomalies reach 0.3-0.35 psu, and the maximum potential temperature anomalies reaches 0.05^{o}C just before the precipitation stops. Four to five hours after the precipitation stopped, the magnitudes of the salinity and potential temperature anomalies at a depth of 2-3 meters, reaches 0.15-0.2 psu and 0.04-0.05 ^{o} C respectively. This rainfall-induced stable layer reaches a depth of about 11-13 meters within a few hours after the precipitation stopped.

A rainfall process with similar characteristics (intensity, range and duration) was observed in December 1992 as part of the Tropical Ocean Global Atmospheres/Coupled Ocean Atmosphere Response Experiment (TOGA/COARE) in the western Pacific warm pool, at 156^{o}E and 2^{o}S. The observed rainfall-induced negative salinity anomaly reached a magnitude of 0.12 psu near the surface with a depth of about 2-3 meters. The magnitude of the corresponding rainfall-induced negative potential temperature anomaly, measured also at a depth of 2-3 meters, reached 0.05 ^{o} C at about 5 hours after the formation of the rainfall-induced low salinity stable layer (Wijesekera *et al.* 1999). Thus the simulation results agree well with the observations.

The magnitudes of salinity anomaly and potential temperature anomaly have opposite effects on the density. The negative salinity anomaly tends to reduce the density (making the upper layer more stable) while the negative potential temperature anomaly tends to increase the density (making the upper layer unstable). Figure3.8 is the (X-Z) vertical cross-section of the resulting density anomaly (rho_{rain} - rho_{norain}). It is clear that (the negative) salinity anomaly has the dominant effect on the density. The density anomaly essentially follows the pattern of the salinity anomaly. The maximum magnitude of the density anomaly reached 0.3, or 1.4 % of the simulated value with no rain.

The UNESCO equation of state, as adapted by Mellor (1991) is used to calculate the sea water density. The equation of state of seawater is a complex nonlinear relationship. The general relationship between temperature, salinity and density is illustrated in the Figure 3.26. It is clear that the salinity anomaly has a more important effect on the variation of density than the temperature anomaly does.

The rainfall-induced low salinity, low temperature and low-density layer has a significant effect on the vertical turbulent transport of the momentum from the surface atmospheric forcing. Differences in the vertical current profiles between the no-rain case and the with-rain case (Figure 3.9) are analyzed to investigate the effect of the rainfall on the vertical turbulent transport. Horizontal positions of the profiles are at the center of the rainfall region, which is also the center of the simulation domain. It is clear from Figure 3.9 that immediately after the rainfall started the zonal velocity near the surface within the rainfall-induced fresh stable layer began to increase, causing significant positive anomaly of U. The magnitude of the U anomaly is at a maximum

value of 0.35 m/s near the surface in five hours since the start of the rainfall event. Below a depth of 11-13 meters, which is also the lower boundary of the rainfall-induced fresh stable layer, the anomaly turns negative. The magnitude of the positive anomaly of U near the surface reaches 0.35 m/s at the fifth hour, a 55% increase. It is much larger than that of the negative anomaly of U below the depth of 11-13 meters, less than 0.1 m/s, about 10%. Similar features are found in other precipitation regions as shown in the vertical cross-sections of the anomaly of the zonal velocity (U_{rain}-U_{norain}) (Figure 3.10).

From Figure 3.9 and Figure 3.10, it is clear that the lower part of the rainfall-induced layer acts as a barrier and the effects of the surface atmospheric forcing cannot penetrate it. This process causes the part of the ocean near the surface to respond to the atmospheric forcing much faster than it would without the effects of rainfall.

As mentioned in Section 2 (the model), the vertical turbulent transport terms, which cannot be resolved explicitly and therefore have to be parameterized, are given by $\frac{\partial}{\partial s}\left[\frac{K_m}{D}\frac{\partial U}{\partial s}\right]$, $\frac{\partial}{\partial s}\left[\frac{K_h}{D}\frac{\partial T}{\partial s}\right]$ and $\frac{\partial}{\partial s}\left[\frac{K_h}{D}\frac{\partial S}{\partial s}\right]$. The vertical diffusivities of momentum and heat, K_m and K_h, respectively, play an important role in the estimation of the vertical turbulent terms. Vertical cross-sections of the anomalies of the simulated K_m and K_h are shown in Figure 3.11 and Figure 3.12.It is apparent that the rainfall causes a significant decrease in the values of K_m and K_h. The magnitudes of the anomalies of K_m and K_h are at their minimum, near zero, at the surface, and increase with depth. At a depth of about 11-13 meters, where the anomaly of U changes sign from positive to

negative, the magnitude of K_m anomaly reaches a value of 0.05 m^2/s, or 90% of the value of K_m, in four hours since the rainfall started. K_h anomaly shows a similar pattern; its magnitude reaching a value of 0.065 m^2/s or 90% of the value of the initial K_h, at a depth of about 11-13 meters in four hours after the rainfall starts. Vertical cross-sections of K_m with and without rainfall are shown in Figure 3.13 and Figure 3.14 respectively.

It appears that the decrease in the simulated vertical diffusivity, K_m, which corresponds to an attenuation of the vertical turbulent mixing, could have caused the effects of the surface atmospheric forcing to be concentrated near the sea surface. Therefore, the effects of the surface rainfall-induced heat flux (cooling), freshwater flux, and the wind stress-induced momentum transport can reach a depth of 11-13 meters only. The isolation of the surface rainfall-induced fresh stable layer from the rest of the mixed layer also causes the surface layer to respond to the atmospheric forcing much faster.

It will be of interest to investigate as to why the rainfall-induced fresh stable layer tends to attenuate the vertical turbulent mixing. As mentioned in Section 2, the vertical turbulent diffusivities are determined by three factors: Turbulent kinetic energy (TKE), turbulent length scale and Richardson number (Ri). The results of the numerical experiments show that the rainfall-induced fresh stable layer has significant effects on the TKE and Ri.

Equation 3.**1** is used to predict the TKE. The left-hand-side has temporal change and horizontal and vertical advection terms. The right-hand-side terms are, from left to right, the vertical turbulent flux, the shear production, the buoyancy production, and the turbulent dissipation.

In the simulations that have a time scale of a few hours, the advection terms are not as important as other terms. Therefore, the discussion will focus on the production terms (buoyancy and shear), dissipation and the turbulent mixing term.

Due to the presence of the rainfall-induced low density layer, the density gradient increases, leading to an increase in Brunt Väisälä frequency, and hence an increase in static stability and a decrease in the buoyancy production of turbulence. Figure 3.15 shows the vertical cross-section of the anomaly of the buoyancy production. It is clear that for depths less than 11-13 meters, the anomaly of the turbulence buoyancy production is negative, apparently caused by the stabilization of the surface fresh layer. The magnitude of the anomaly is at maximum at about 3 meters. The maximum anomaly of the buoyancy production term reaches a value of 6 x 10^{-7} m^2/s^3, at the 4^{th} hour.

At the beginning of the rainfall process, the direct effect of rainfall-induced fresh layer is the stabilization of the upper layer, which tends to decrease the turbulent production. The decrease of the turbulent production leads to the attenuation of the vertical turbulent flux (Figures 3.11 and 3.12), causing the momentum to concentrate near the surface. Consequently, the shear production of turbulence begins to develop,

due to the increased velocity gradient between the rainfall-induced fresh layer and the layer below it. Figure 3.16 is the vertical cross-section of the anomaly of shear production term. The magnitude of the positive anomaly of shear production of turbulence is larger than that of the negative anomaly of the buoyancy production of turbulence (Figures 3.15 and 3.16). Thus the rainfall-induced stable layer does not cause the total turbulence production (buoyancy production + shear production) to decrease. However, the increased turbulence also leads to an increase in the turbulence dissipation as shown in Figure 3.17. The anomaly of the net turbulence production (buoyancy production + shear production – dissipation) is shown in Figure 3.18. It appears that one hour after the precipitation starts, the net turbulence production increases significantly (a positive anomaly) near the surface and decreased (a negative anomaly) below the depth of about 11-13 meters. However, the magnitudes of the anomalies of the net turbulence production decreases quickly in the following hours. The positive anomalies near the surface become 1, 0.8 and 0.6 m^3/s^3 at second, third and fourth hours, respectively. The simulated negative anomalies are not as coherent as at the beginning of the rainfall. The decrease in the magnitudes of the anomalies shows that the effect of the rainfall-induced stable fresh water layer on the net turbulence production is diminishing rapidly.

Vertical cross-section of the anomaly of the TKE is shown in Figure 3.19. Comparing Figure 3.18with Figure 3.19, it is clear that with the decrease in the effect of the rainfall-induced fresh stable layer on the net turbulence production, the magnitude of the anomalies of the TKE increases significantly. This means that in

addition to the effects on the net turbulence production, the vertical turbulent flux term (the first right-hand-term in TKE equation Equation (3.1)) also appears to be an important factor in determining the variation of turbulence due to the rainfall. Vertical cross-section of the anomaly of the vertical diffusivity K_q is shown in Figure 3.20. Similar to the momentum, the turbulence that is transported downward to depths below 11-13 meters also decreases. More turbulence is concentrated near the surface causing the turbulence near the surface to increase. After getting disconnected from its source above, the turbulence below 11-13 meters decreases significantly.

In addition to TKE, the stability parameter Richardson number (Ri) is also affected by the rainfall. Ri is actually the ratio of buoyancy production to the shear production. Figure 3.21 is the vertical cross-section of the anomaly of Ri. Before the rainfall starts, the uppermost few meters are well mixed without significant density gradient, so Ri is close to zero near the surface. One hour after the rainfall started, due to the stratification induced by the rainfall, Ri increases drastically, reaching a maximum value of 0.35 and remaining positive through the rainfall-induced fresh layer. However, in later hours, due to the increase in the simulated velocity shear, the effects of the dynamic instability increase rapidly. After the end of the rainfall, source of fresh water does not exist, while the wind stress continues to provide momentum, causing stronger velocity shear. Consequently, the Ri dropped to a value below 0.25 (Figure 3.21), the critical Richardson number. This means that the effect of the shear on the TKE production is larger than the effect of the rainfall-induced stratification. This agrees with the simulation results discussed above that the turbulence production continues even after the end of the rainfall.

Although the R_i is under the critical Richardson number, which means the shear-induced dynamic instability is still dominant, the rainfall-induced stratification has significant effects on the vertical diffusivities, K_h and K_m, through the functions, S_h and S_m, in (see Equation (3.3) and (3.4) in section 2, the model). The rainfall-induced fresh layer causes the stability functions S_h and S_m to decrease drastically (Figure 3.22 and Figure 3.23). The details of the calculation of S_h and S_m are available from Mellor and Yamada (1982).

The anomaly of stability-related functions S_h and S_m in Equations (3.3) and (3.4), combined with the anomaly of turbulence kinetic energy, result in a significant decrease in the simulated vertical turbulent flux diffusivities, K_h and K_m. (Figure 3.11, 3.12, 3.13 and 3.14). The magnitudes of the negative anomaly of turbulent diffusivities are small near the surface. At a depth of 11-13 meters, the magnitudes of the anomalies reach 90%. This appears to be the reason that the turbulence caused by the surface atmospheric forcing due to the freshwater flux and the momentum flux cannot propagate below the depth of 11-13 meters. The fresh layer is thus isolated from the rest of the ocean and its response to the atmospheric forcing becomes much more rapid.

3. 4. 3 Sensitivity to the short-wave radiation warming (Exp 3.4 and Exp 3.5)

The results of the numerical experiments 3.2 and 3.3 show that K_h, the vertical heat diffusivity, experienced similar variation to K_m, the vertical momentum diffusivity. It is believed that the surface downward heat flux, such as the short-wave radiation after the rainfall, an important mechanism in air-sea interaction, may act in a similar way to the momentum flux. That is, the heat may also concentrate near the surface, without being transferred downward. An experiment is carried out to examine the rainfall-induced fresh layer's effect on the downward heat fluxes. A short-wave radiation that contributes to a downward vertical heat flux of 200 W/m^2 to the ocean is imposed on the surface after the rainfall stopped, and the warming continued for four hours (Exp 3.5).

In a companion experiment, the same short wave warming is imposed with the same configuration except that there is no rainfall (Exp 3.4). Increase of the sea surface temperature (SST_{norain}-$SST_{norain\_t=0}$) due to the short wave radiation warming without rainfall (Exp 3.4) is shown in Figure 3.24. Increase of the sea surface temperature due to the short wave radiation warming with rainfall is shown in Figure 3.25. From Figure 3.24 and Figure 3.25, it is apparent that without rainfall, the increase in SST due to the short-wave radiation reaches a maximum value of only 0.035 ^{o}C. In addition, the warming effect does not last long. In four hours, the warming effect has become insignificant. In the case with rainfall, the increase in SST reaches a maximum value of 0.13 ^{o}C, nearly three times more than that without rainfall. In addition, the warming effect lasts significantly longer than that without rainfall. On the fourth hour since the start of the short-wave radiation, the positive SST anomalies are still significant and coherent. It is clear that due to the inclusion of the rainfall, the simulated K_h decreases, as mentioned before (Figure 3.12), and the

short-wave radiation warming is concentrated near the surface. The rainfall-induced fresh layer responds to this warming much more rapidly than the rest of the ocean below it.

3.5. Conclusions

Because of a lack of adequate observations on the western Pacific warm pool region during convective precipitation, numerical simulations provide an important approach to study the air-sea interaction processes. The simulations reproduced ocean's response to the precipitation, such as the formation of a fresh layer and surface cooling, which agree well with the observations. The precipitation-induced fresh layer can cause the vertical turbulent diffusivities to diminish at a depth of about 11-13 meters within a few hours. The concentration of the surface wind stress-induced momentum near the surface causes an increase in the velocity shear, which, in turn, causes significant dynamic instability and turbulence increases near the surface. Hence when there is precipitation, the ocean appears to respond to the surface atmospheric forcing much faster than it would without rainfall. The simulation results are in agreement with the observations

Although the results of this study support the hypothesis that rainfall can cause the upper ocean to respond to atmospheric forcing more rapidly than it would without rainfall, further studies are still needed to fully understand the air sea interaction mechanisms. One of the inadequacies of this study is that only the atmospheric effects on the ocean are considered. The ocean's feedback is not included. To fully understand the air-sea interaction processes, aair-sea coupled model is required.

The simulated freshwater (or the barrier) layer is shallower (10-13 m) as compared to the observed barrier layer over the western Pacific warm pool region (Lukas and Lindstrom, 1991). In this simulation only SST is fed back from ocean model to atmospheric model. Other effects such as those of waves and spray are not considered. Further work is needed to consider these factors and thus to make the coupled model a dynamical two-way modeling system.

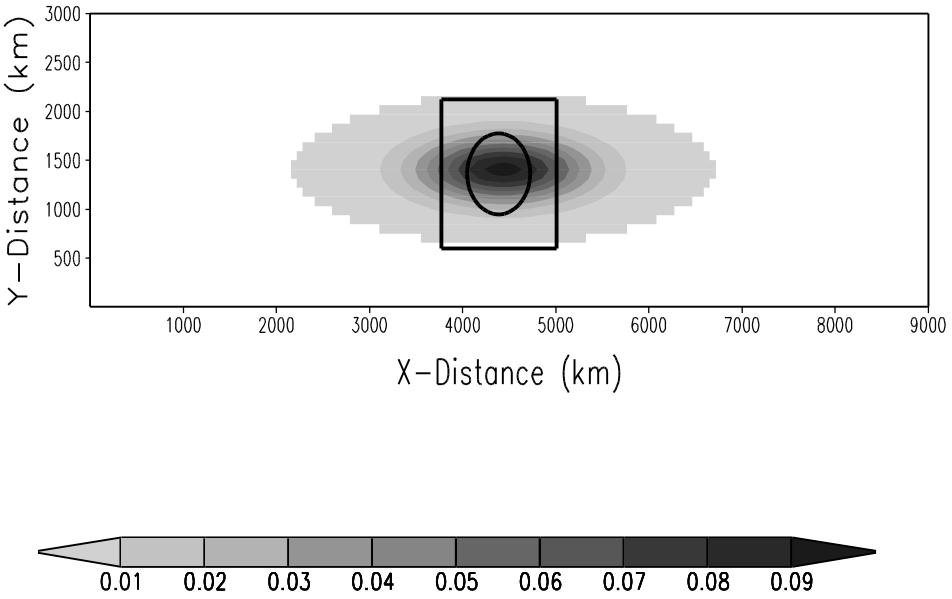

Figure 3.1. Wind stress (N/m^2) used in Exp 3.1. The region enclosed by the inner rectangle is the domain in Exp 3.2, Exp 3.3, Exp 3.4 and Exp 3.5 The area enclosed by the inner circle is the region of the imposed rainfall in Exp 3.2, Exp 3.3, Exp 3.4 and Exp 3.5.

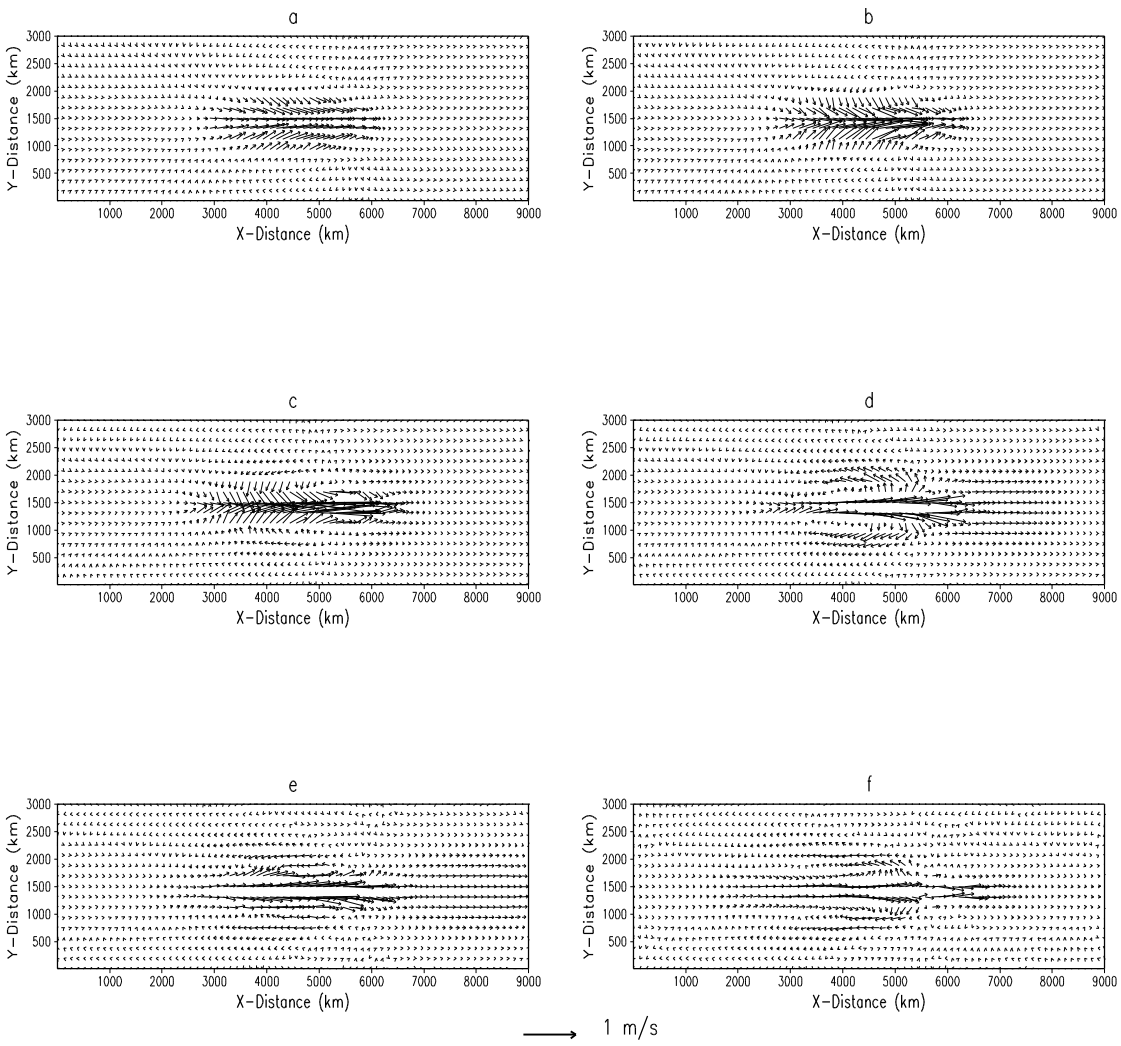

Figure 3.2. Simulated surface velocity fields in Exp 1 (a) 3 days (b) 5 days (c) 10 days (d) 15 days (e) 20 days (f) 30 days since the beginning of simulation.

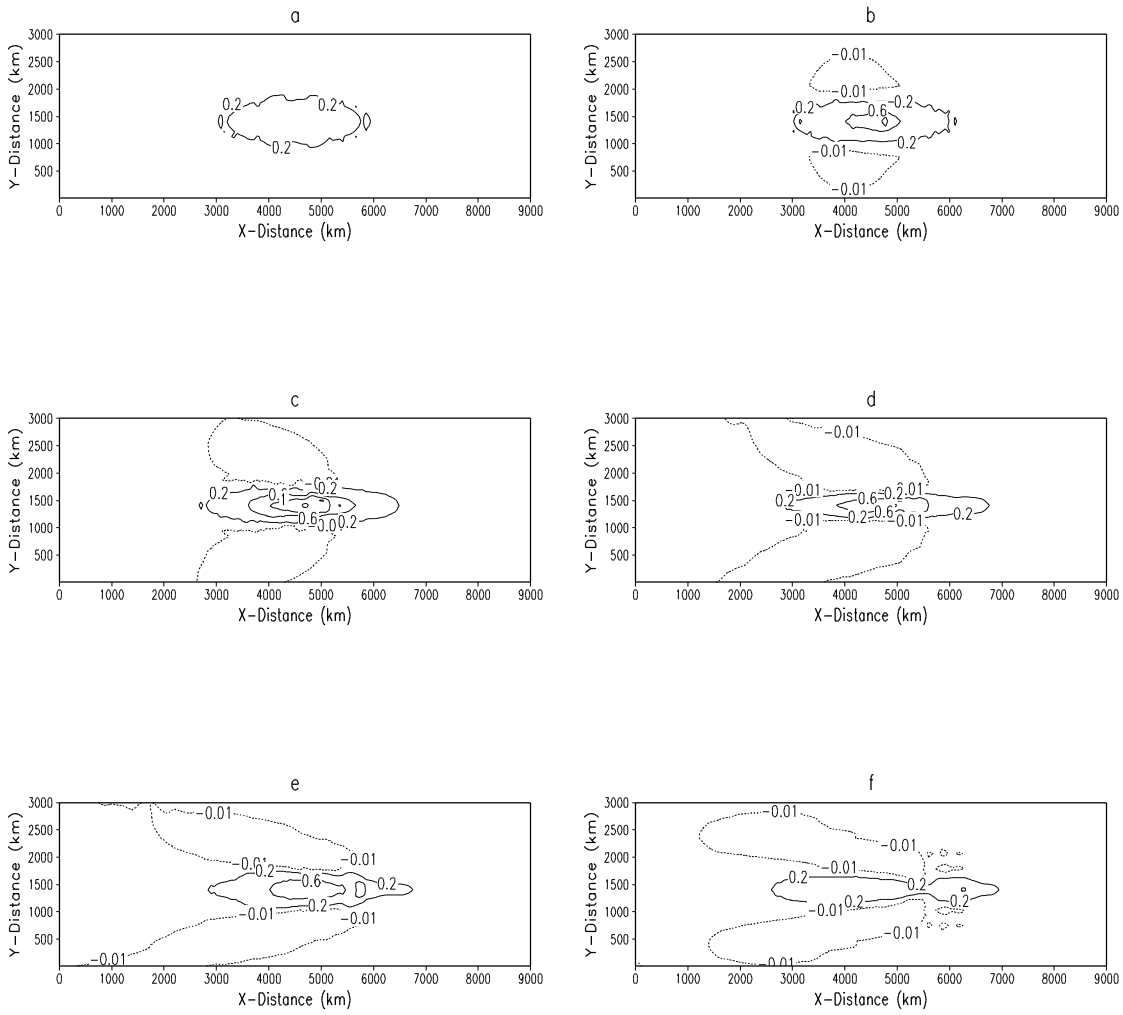

Figure 3.3. Simulated surface zonal velocity, U (m/s), in Exp 1 (a) 3 days (b) 5 days (c) 10 days (d) 15 days (e) 20 days (f) 30 days since the beginning of simulation. Positive values indicate eastward currents. Note that wind stress is switched off on the 10^{th} day.

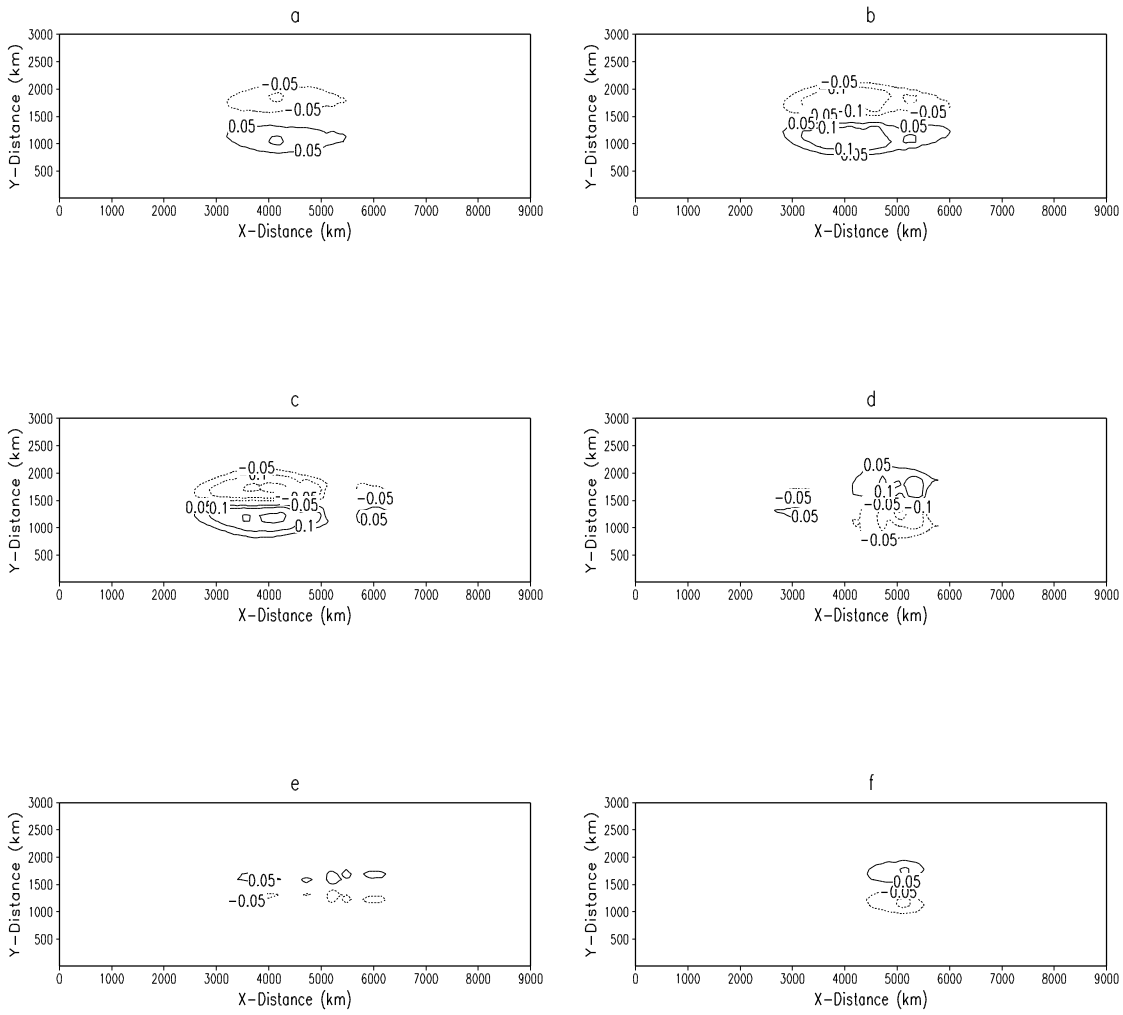

Figure 3.4. Simulated surface meridional current, V (m/s), in Exp 1 (a) 3 days (b) 5 days (c) 10 days (d) 15 days (e) 20 days (f) 30 days since the beginning of simulation. Note that wind stress is switched off on the 10th day. Positive values indicate the northward currents and the negative values indicate the southward currents.

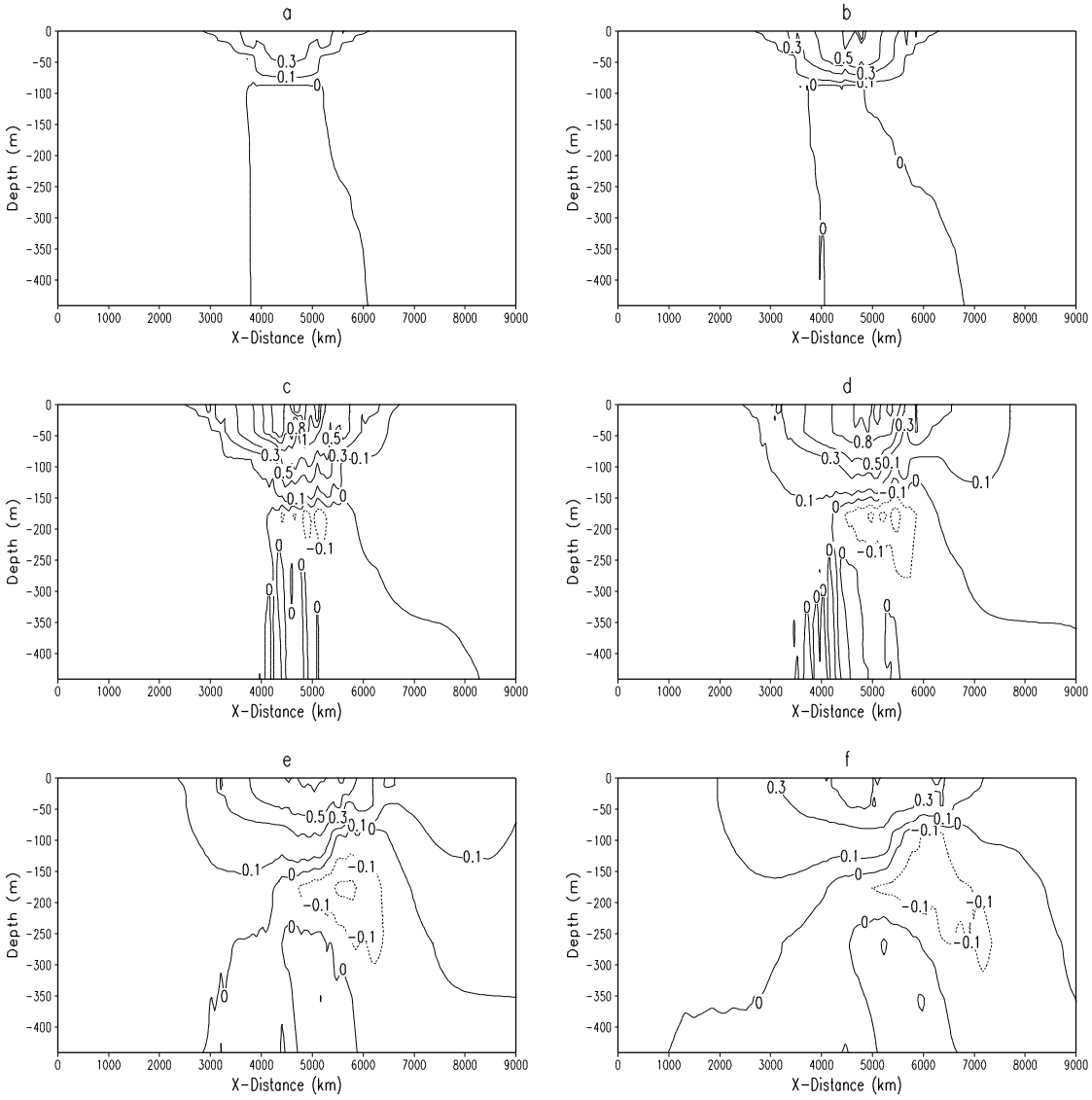

Figure 3.5. Simulated vertical (X-Z) cross-sections of zonal velocity U (m/s) in Exp 1 (a) 3 days (b) 5 days (c) 10 days (d) 15 days (e) 20 days (f) 30 days since the beginning of simulation. Positive values indicate the eastward Yoshida jet. Negative values indicate the subsurface westward jet (SSWJ).

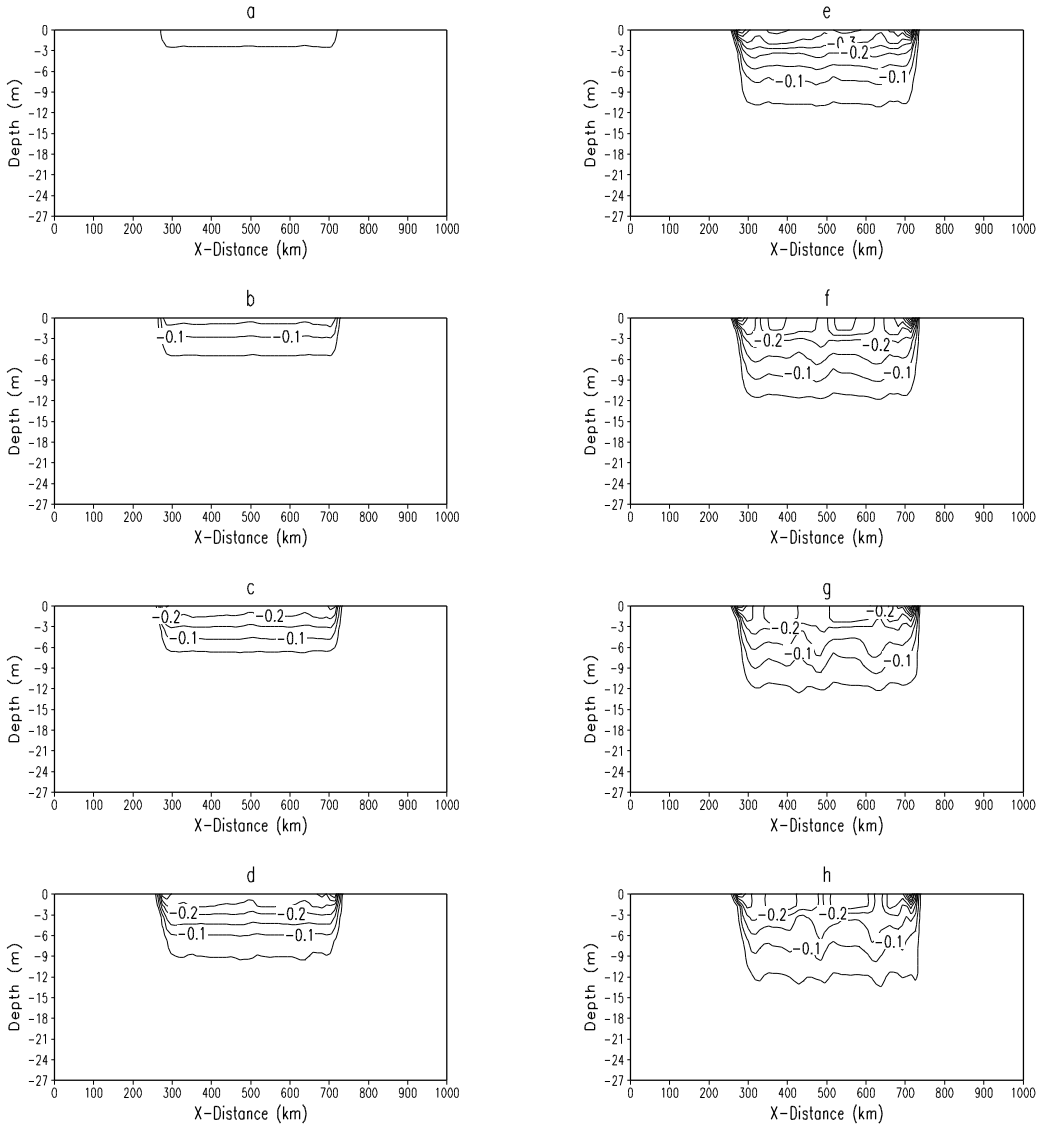

Figure 3.6. Simulated vertical (X-Z) cross-sections of the differences between the salinities in Practical Salinity Unit (psu) with and without rainfall (a) 2h (b) 3h (c) 4h (d) 5h (e) 6h (f) 7h (g) 8h (h) 9h since the beginning of simulation. The negative values indicate the rainfall-induced low salinity layer.

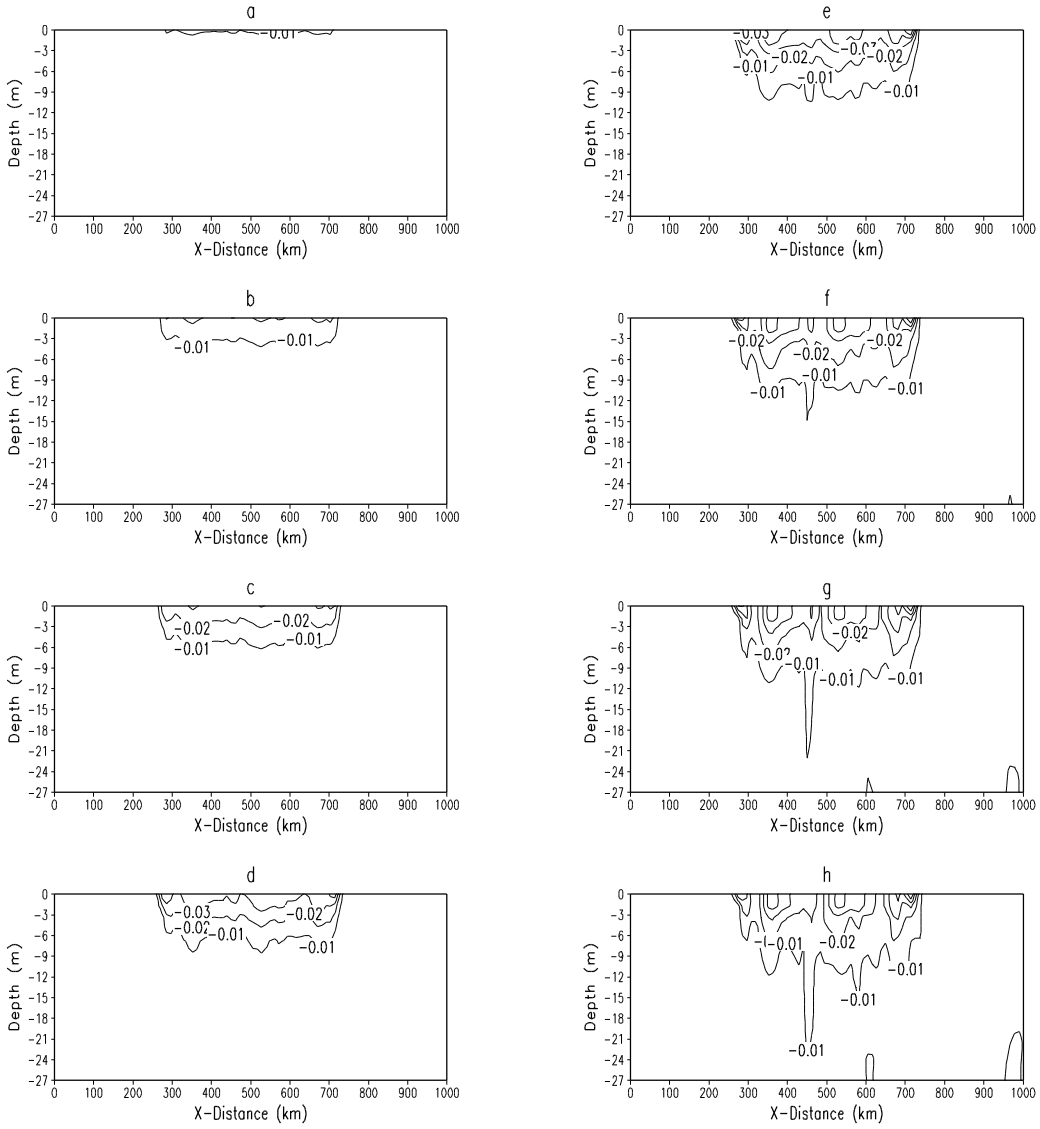

Figure 3.7. Simulated vertical (X-Z) cross-sections of the differences between the potential temperature (K) with and without rainfall (a) 2h (b) 3h (c) 4h (d) 5h (e) 6h (f) 7h (g) 8h (h) 9h since the beginning of simulation.

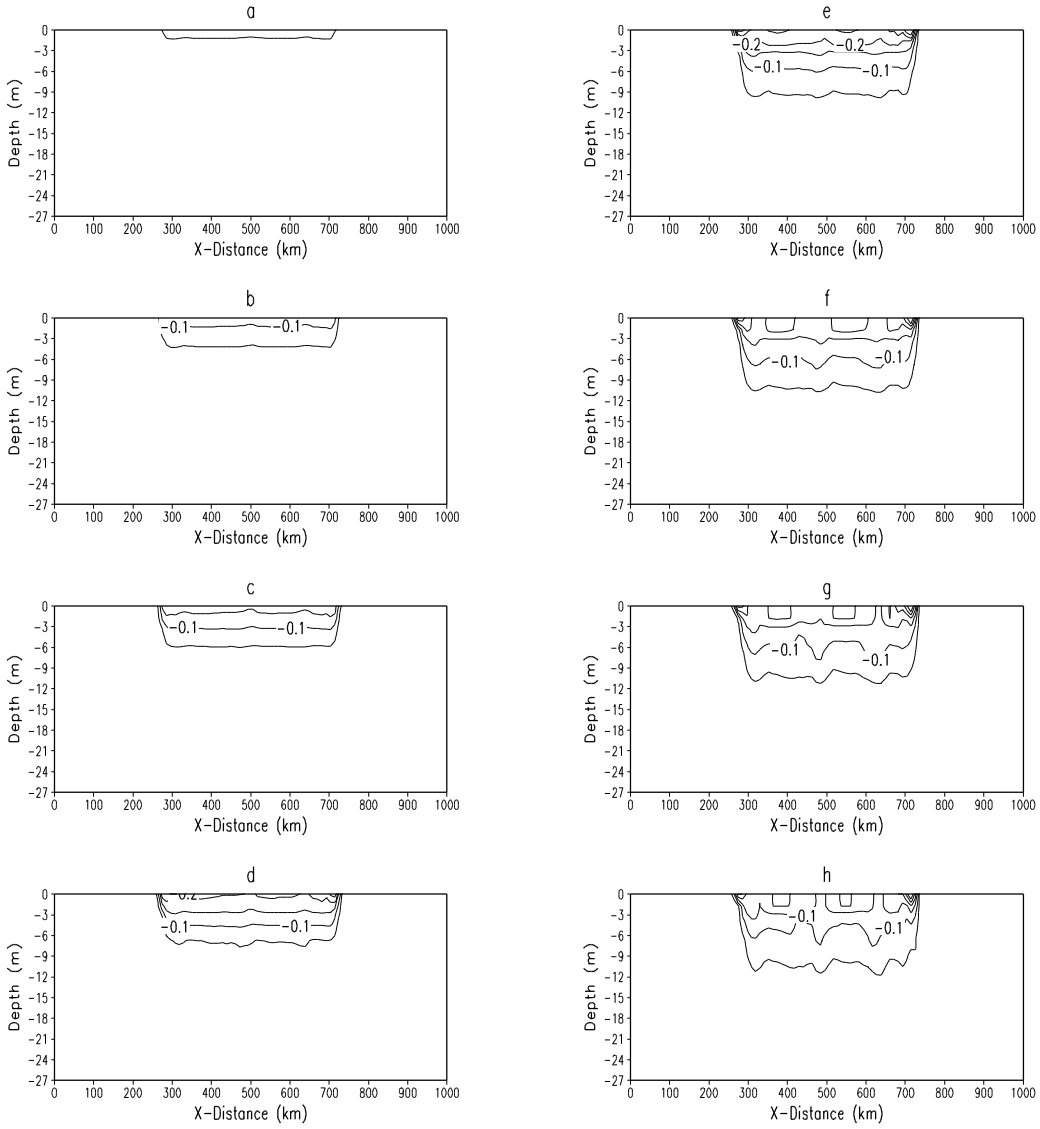

Figure 3.8. Simulated vertical (X-Z) cross-sections of the differences between density (kg/m^3) with and without rainfall (a) 2h (b) 3h (c) 4h (d) 5h (e) 6h (f) 7h (g) 8h (h) 9h since the beginning of the simulation. Note that the pattern of the density variation follows that of the salinity variation (see Figure 3.6).

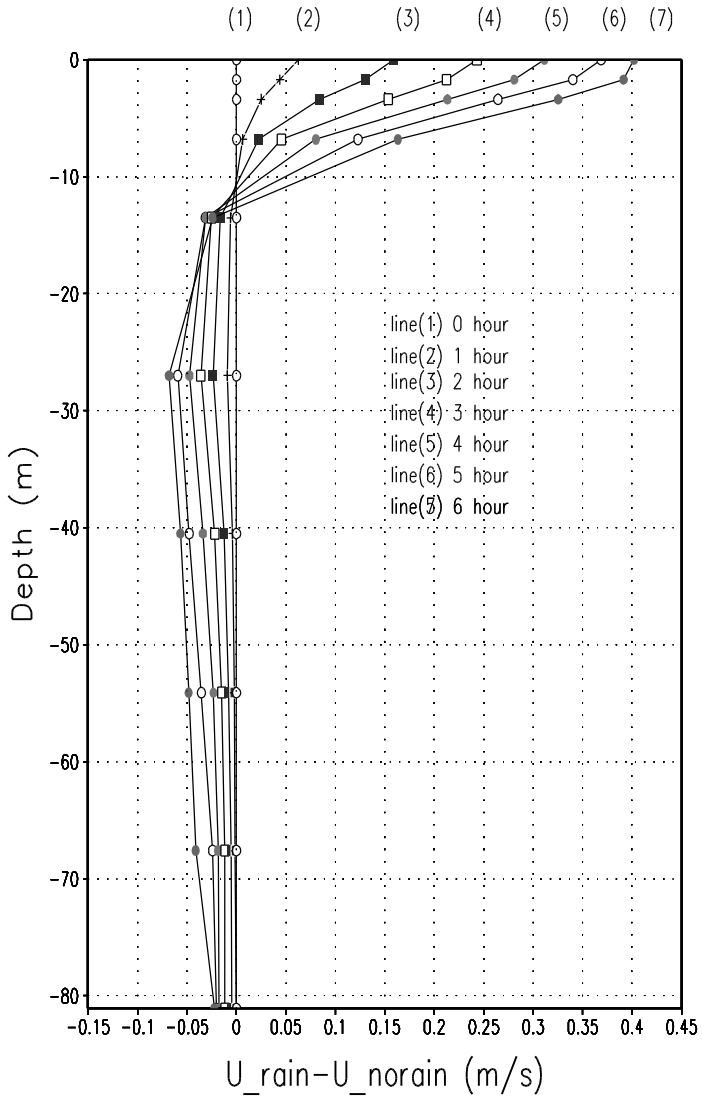

Figure 3.9 Simulated vertical profiles of the difference between zonal velocities with and without rainfall (U_rain-U_norain) in m/s, 0-6 hours since the rainfall starts

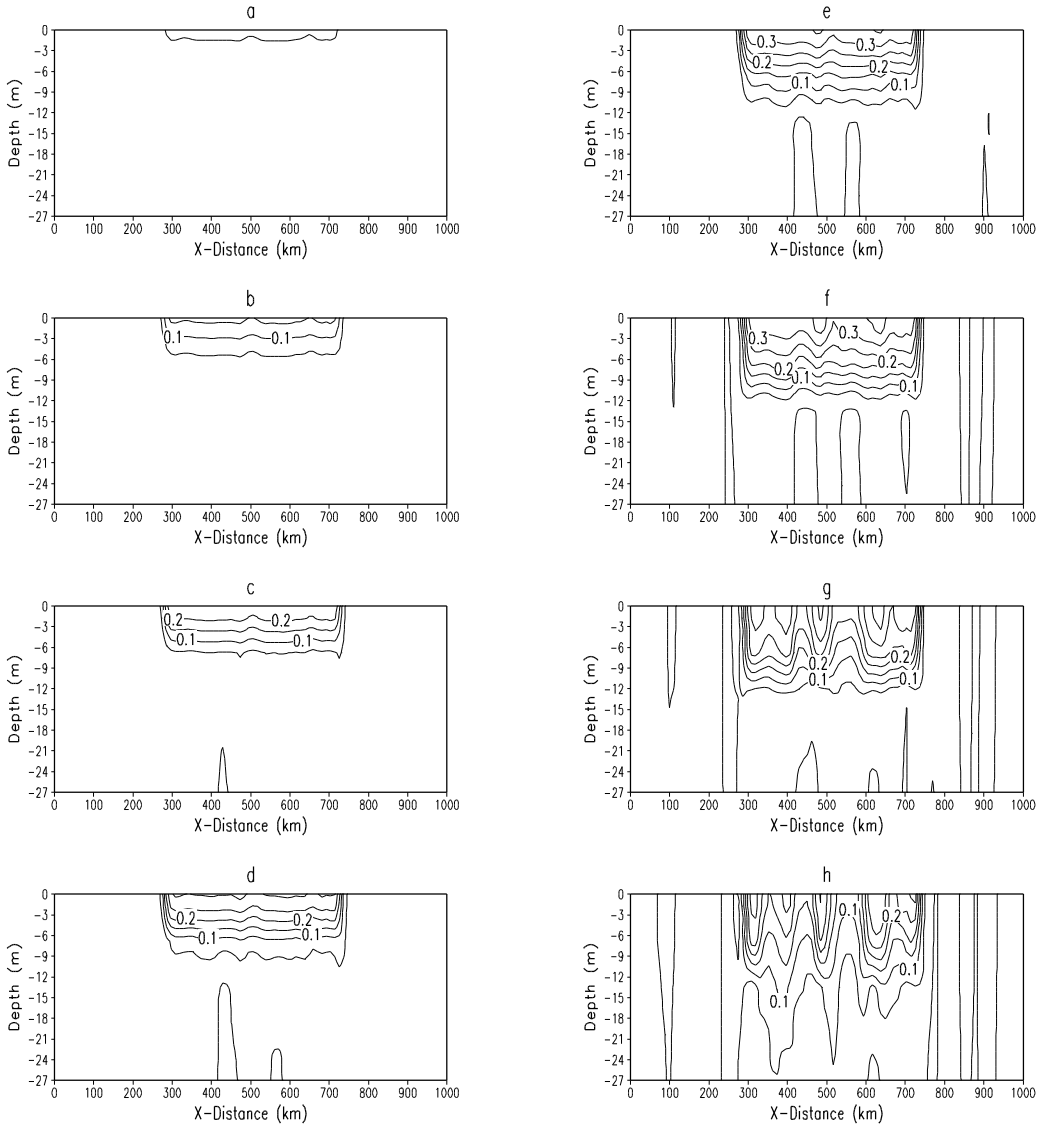

Figure 3.10. Simulated vertical (X-Z) cross-sections of the differences between the zonal velocities, U (m/s), with and without rainfall (a) 2h (b) 3h (c) 4h (d) 5h (e) 6h (f) 7h (g) 8h (h) 9h since the beginning of the simulation.

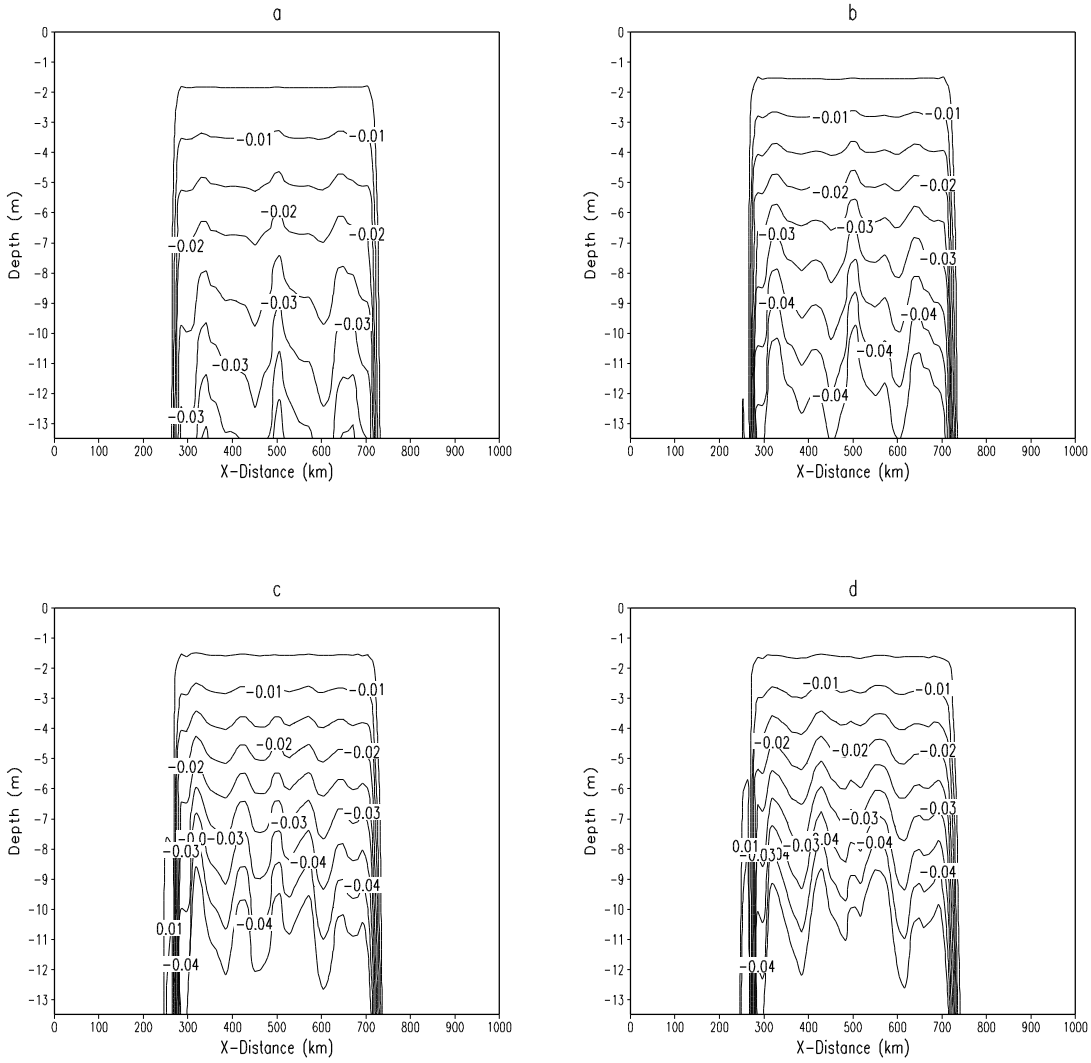

Figure 3.11. Simulated vertical (X-Z) cross-sections of the differences of the momentum turbulent coefficient K_m (m^2/s) between the simulation results with and without rainfall (a) 2h (b) 3h (c) 4h (d) 5h since the beginning of simulation.

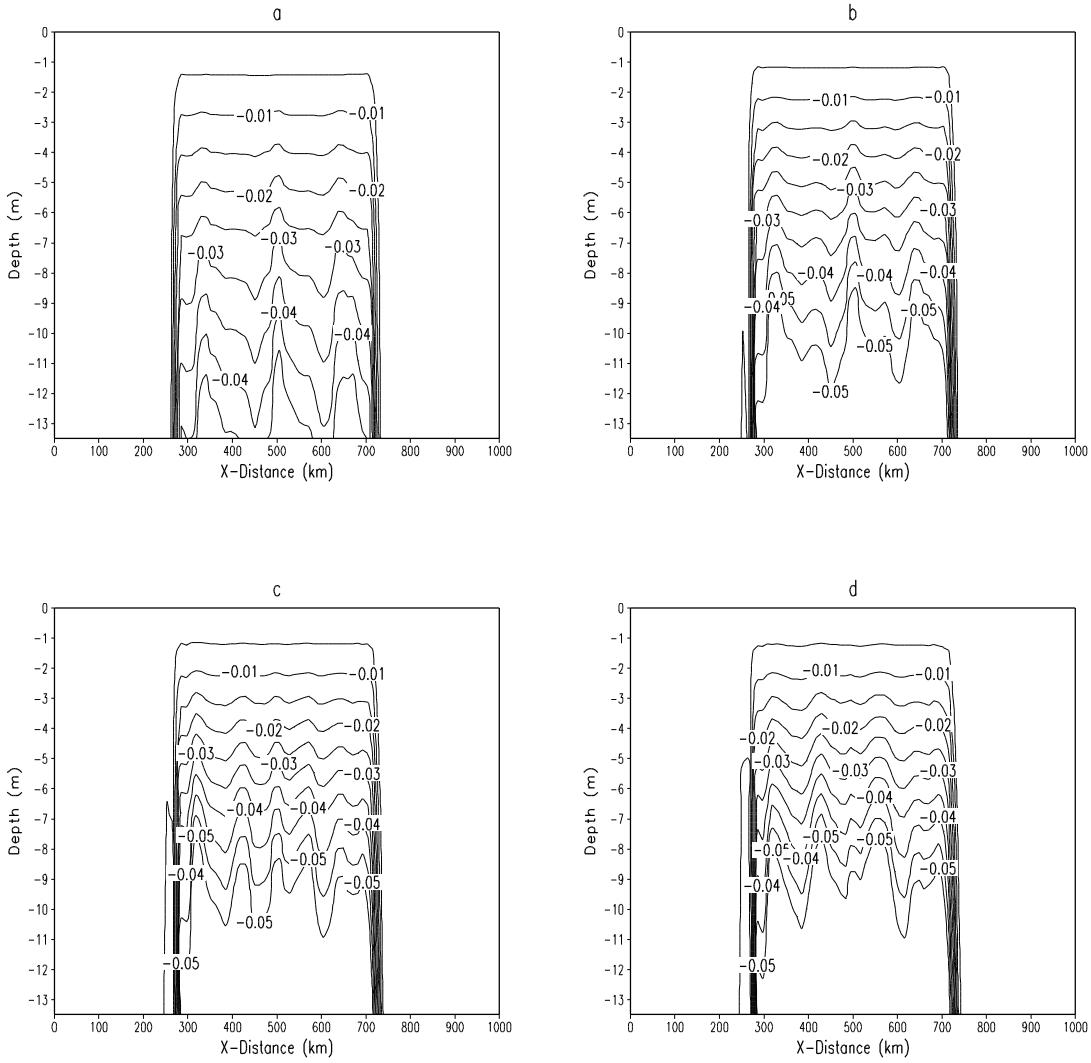

Figure 3.12. Simulated vertical (X-Z) cross-sections of the differences of the turbulent diffusivity K_h (m^2/s) between the simulation results with and without rainfall (a) 2h (b) 3h (c) 4h (d) 5h since the beginning of simulation.

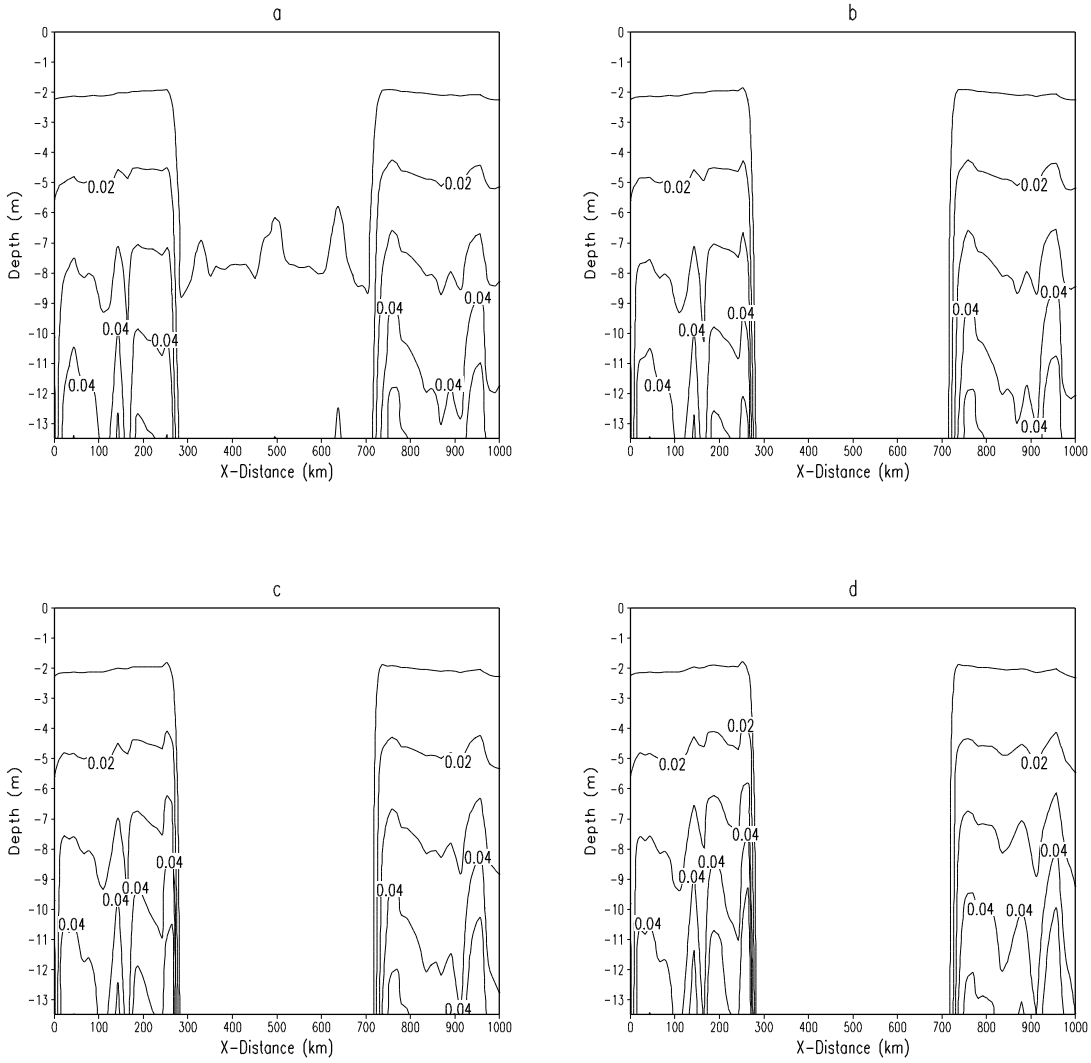

Figure 3.13. Simulated vertical (X-Z) cross-sections of the momentum turbulent coefficient K_m (m^2/s) with rainfall (a) 2h (b) 3h (c) 4h (d) 5h since the beginning of simulation. Note that under the rainfall-covered region K_m values become near zero due to the increased static stability.

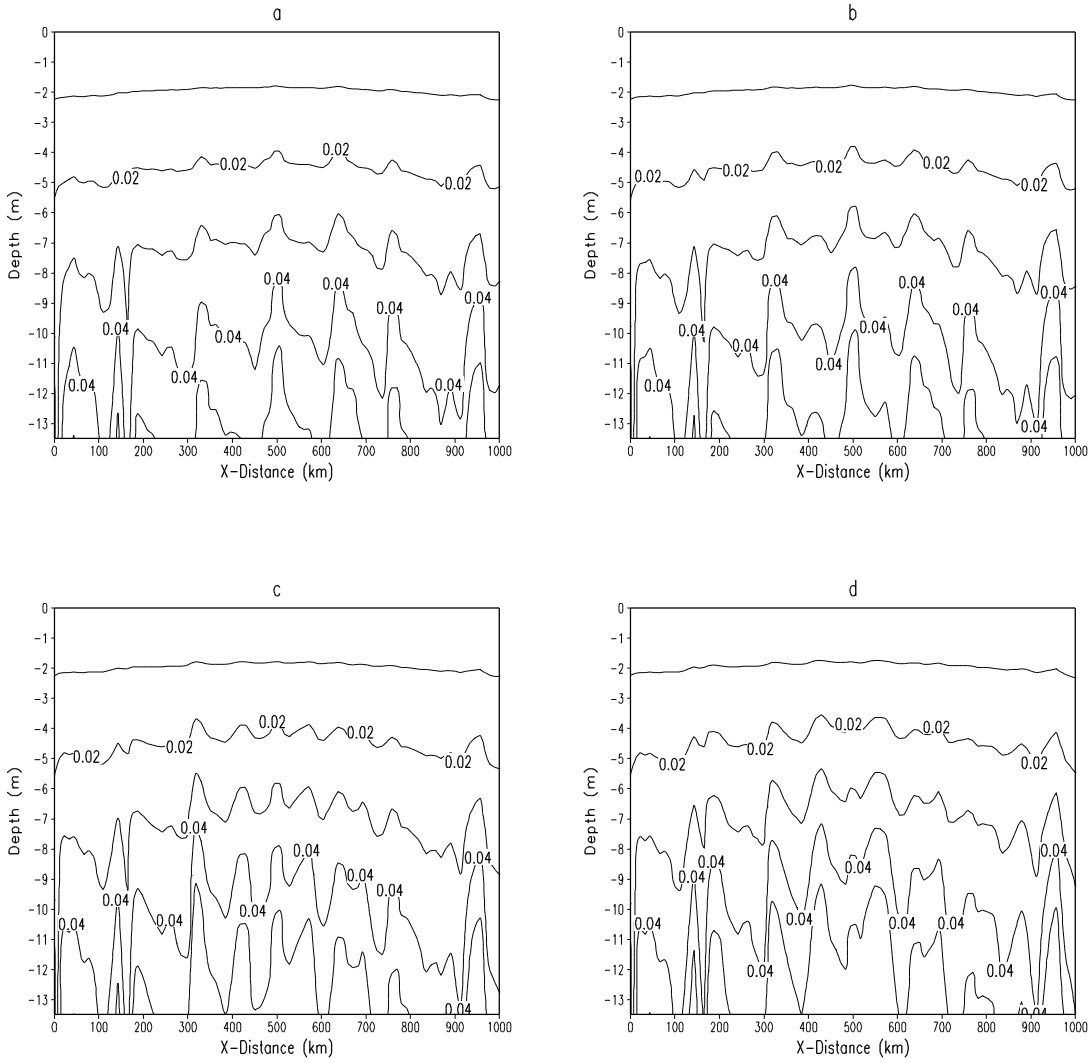

Figure3.14 Simulated vertical (X-Z) cross-sections of the momentum turbulent coefficient K_m (m^2/s) without rainfall (a) 2h (b) 3h (c) 4h (d) 5h since the beginning of simulation.

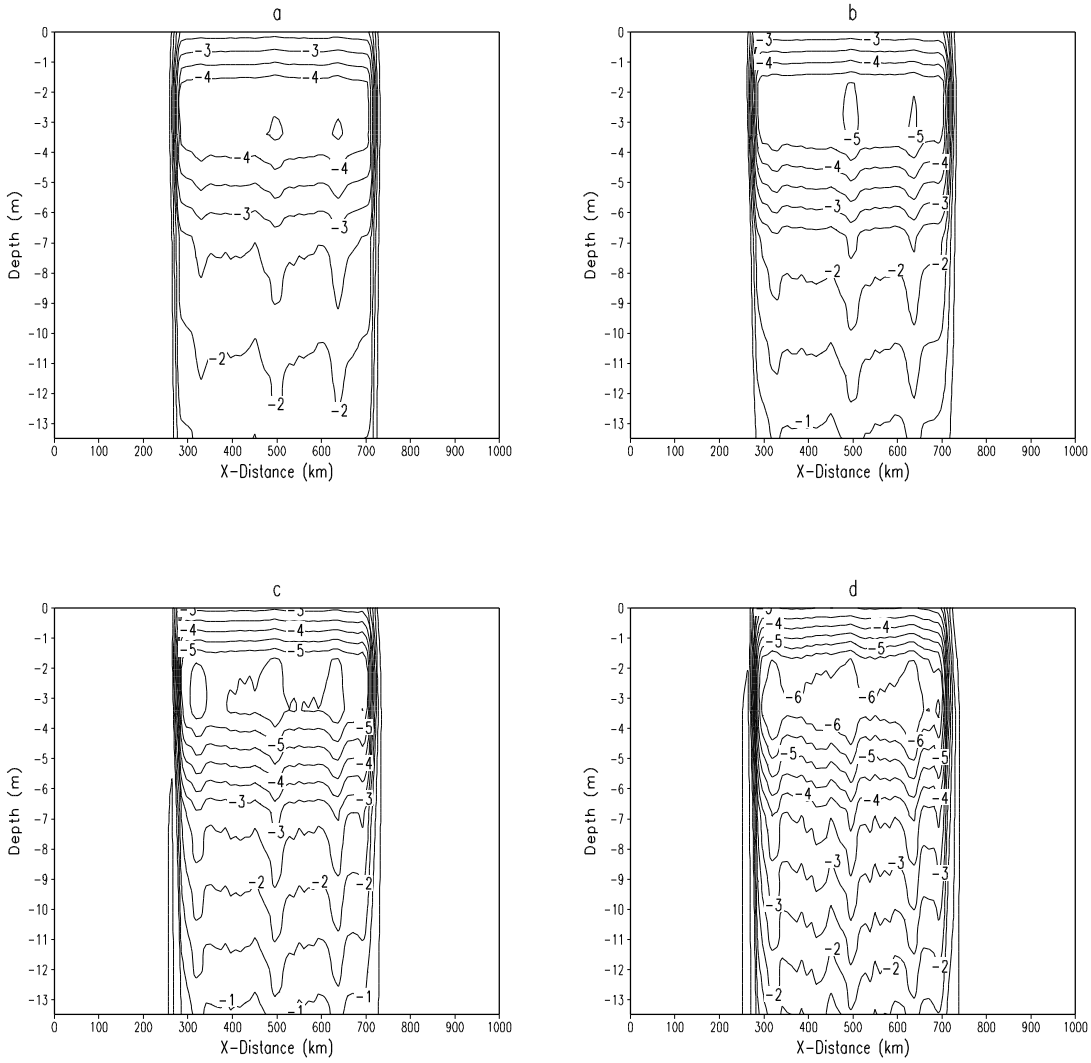

Figure 3.15. Simulated vertical (X-Z) cross-sections of the differences between the TKE buoyancy production terms (m^2/s^3*10^{-7}) with and without rainfall (a) 2h (b) 3h (c) 4h (d) 5h since the beginning of simulation.

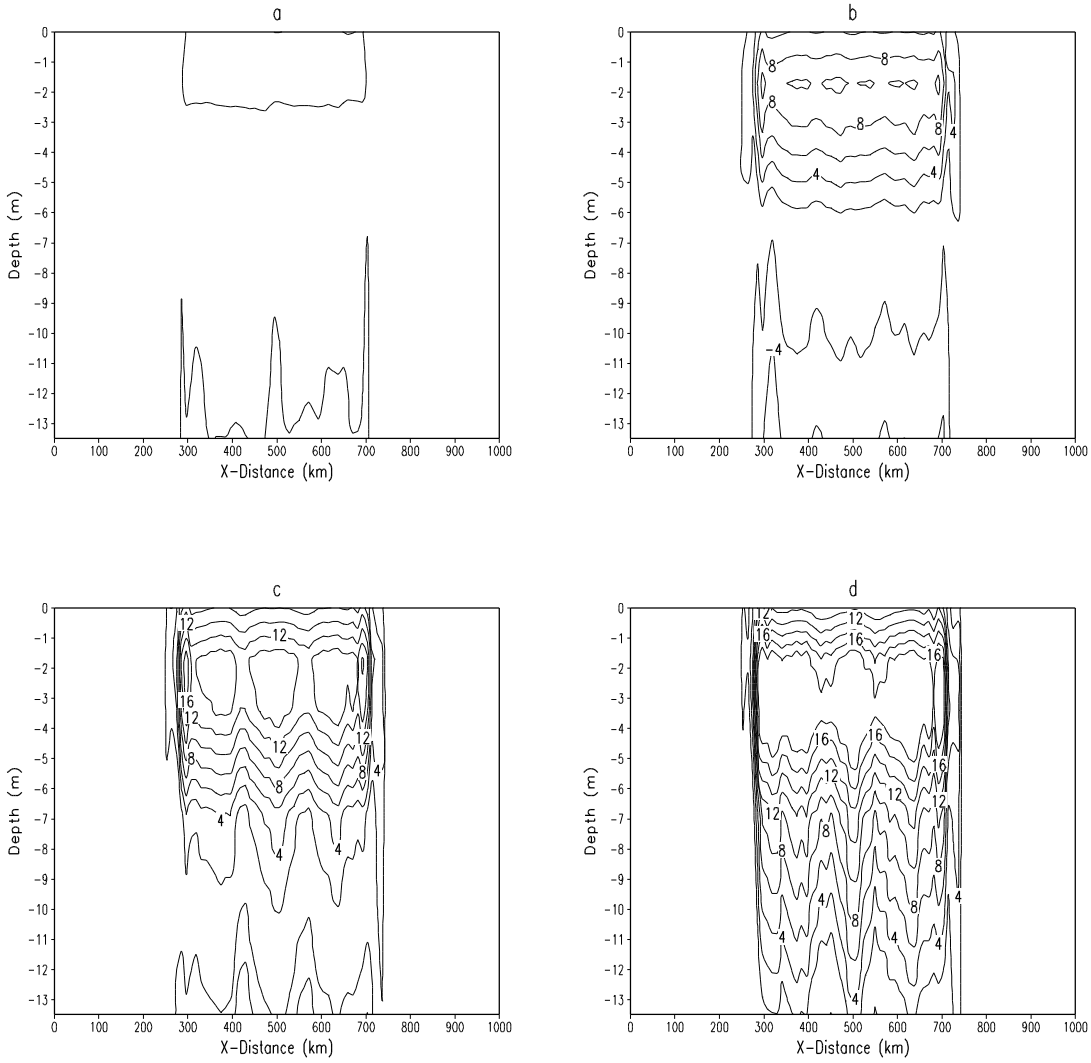

Figure 3.16. Simulated vertical (X-Z) cross-sections of the differences between the TKE shear production terms (m^2/s^3*10^{-7}) with and without rainfall (a) 2h (b) 3h (c) 4h (d) 5h since the beginning of simulation. Note that the increases in wind shear are due to the concentration of momentum near the ocean surface

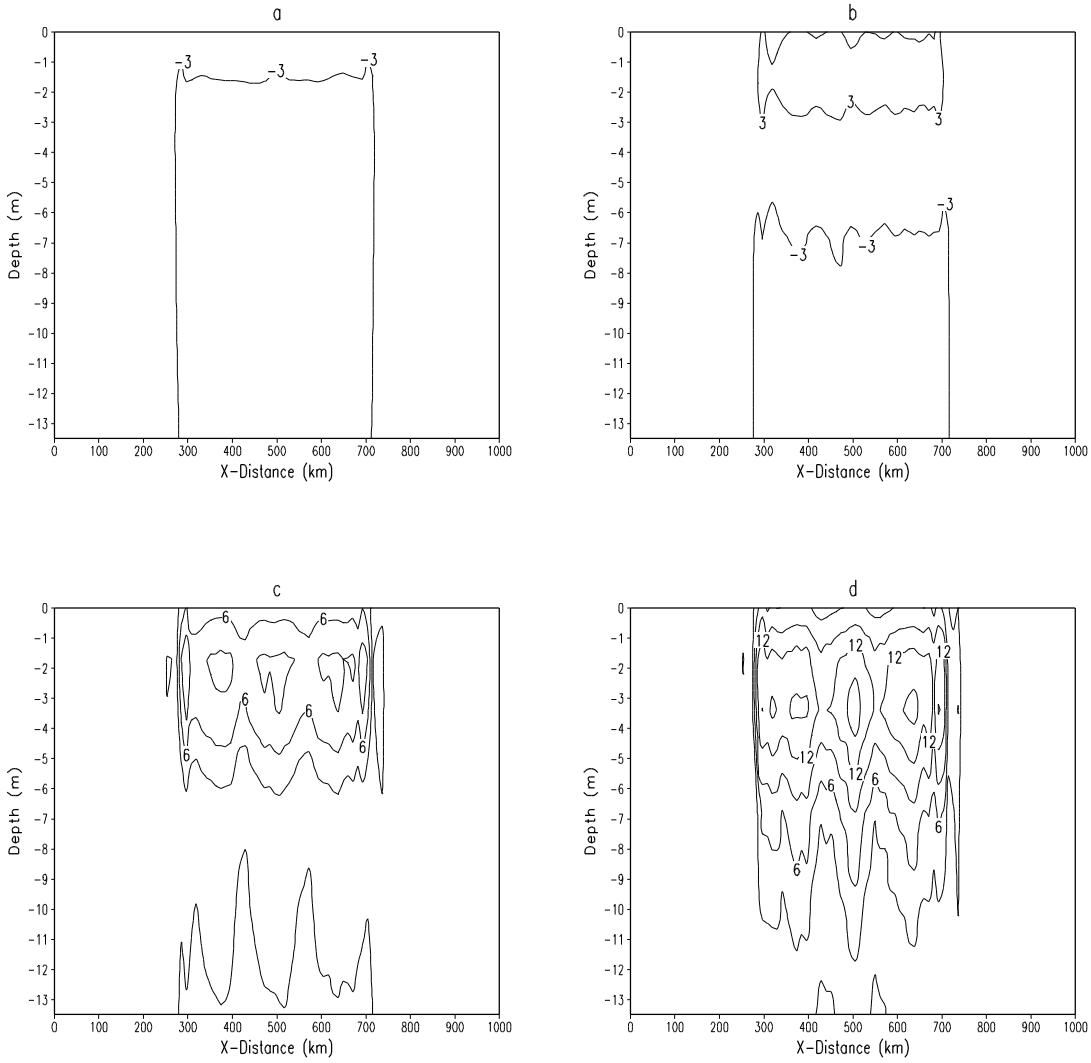

Figure 3.17. Simulated vertical (X-Z) cross-sections of the differences between the TKE dissipation terms (m^2/s^3*10^{-7}) with and without rainfall (a) 2h (b) 3h (c) 4h (d) 5h since the beginning of simulation.

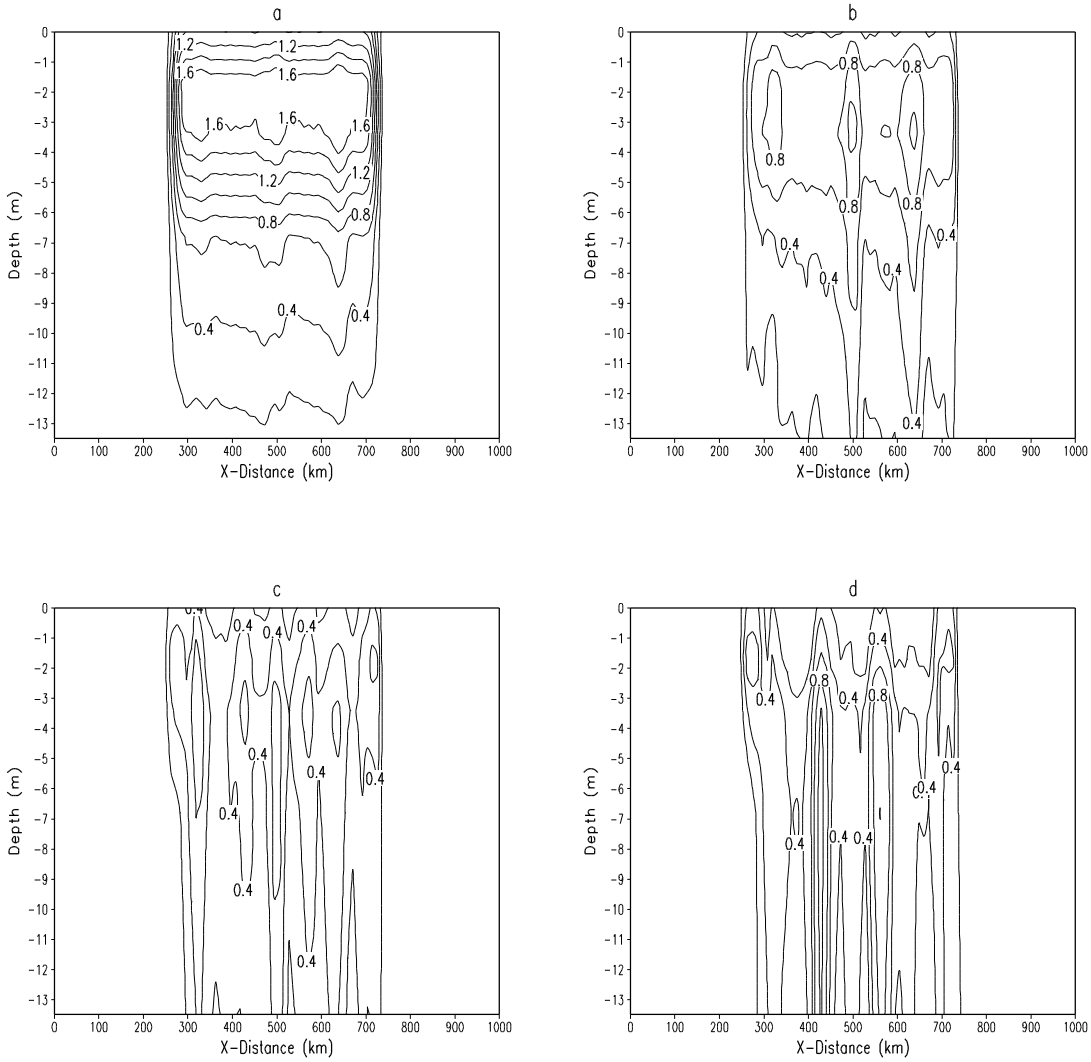

Figure 3.18. Simulated vertical (X-Z) cross-sections of the differences between the TKE net production terms (buoyancy production + shear production - turbulence dissipation) (m^2/s^3*10^{-7}) with and without rainfall (a) 2h (b) 3h (c) 4h (d) 5h since the beginning of simulation.

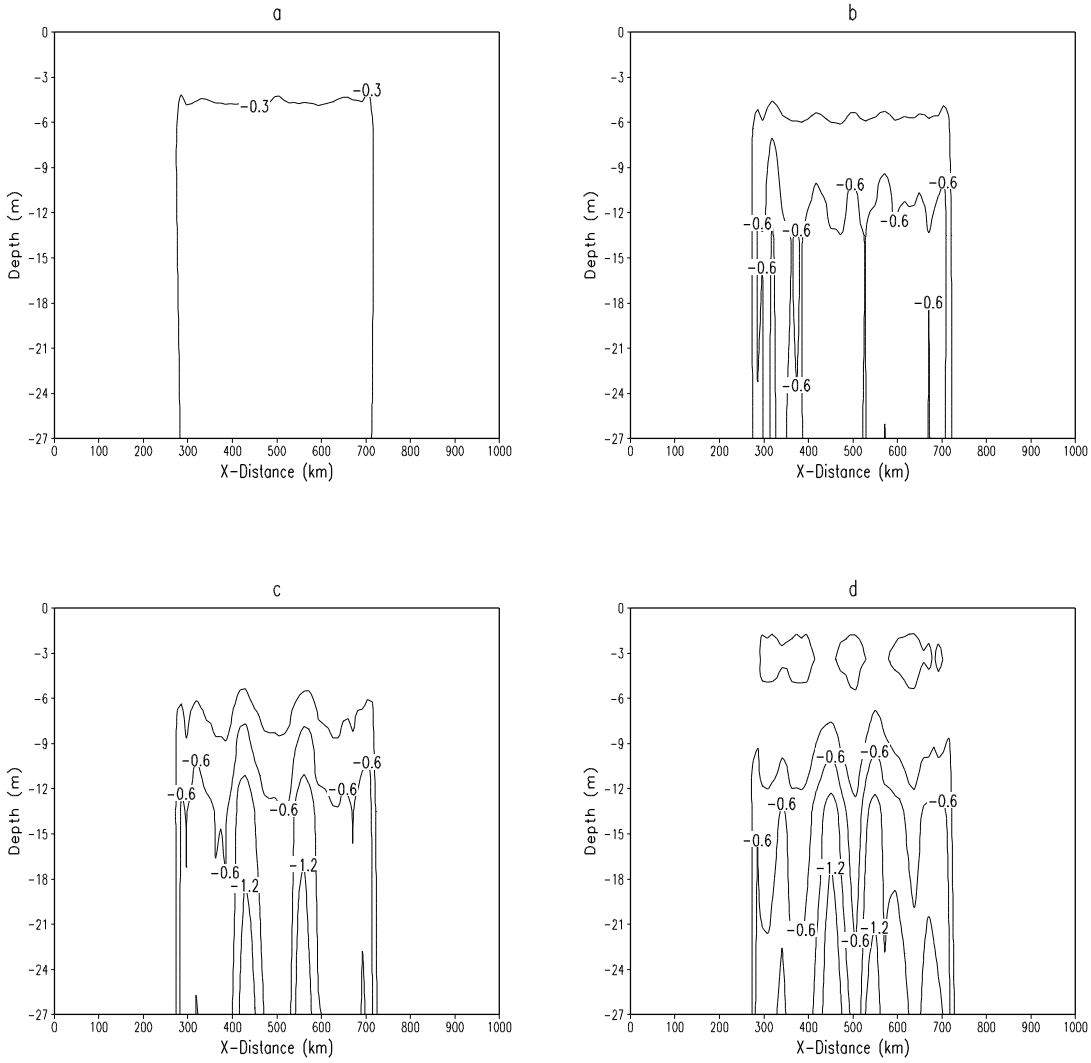

Figure 3.19. Simulated vertical (X-Z) cross-sections of the differences between TKE (m^2/s^2*10^{-3}) with and without rainfall (a) 2h (b) 3h (c) 4h (d) 5h since the beginning of simulation.

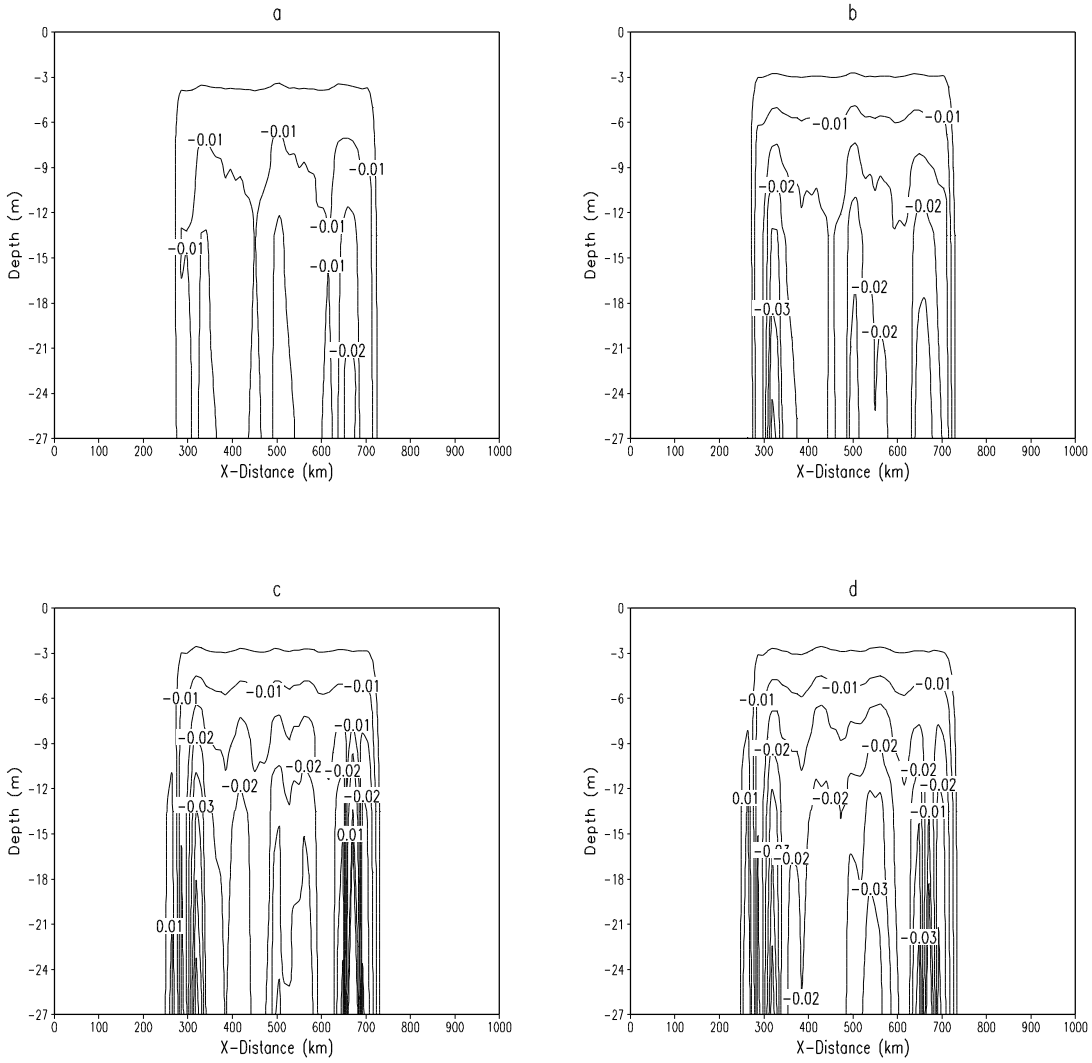

Figure 3.20. Simulated vertical (X-Z) cross-sections of the differences of the TKE diffusivity coefficient K_q (m^2/s) with and without rainfall (a) 2h (b) 3h (c) 4h (d) 5h since the beginning of simulation.

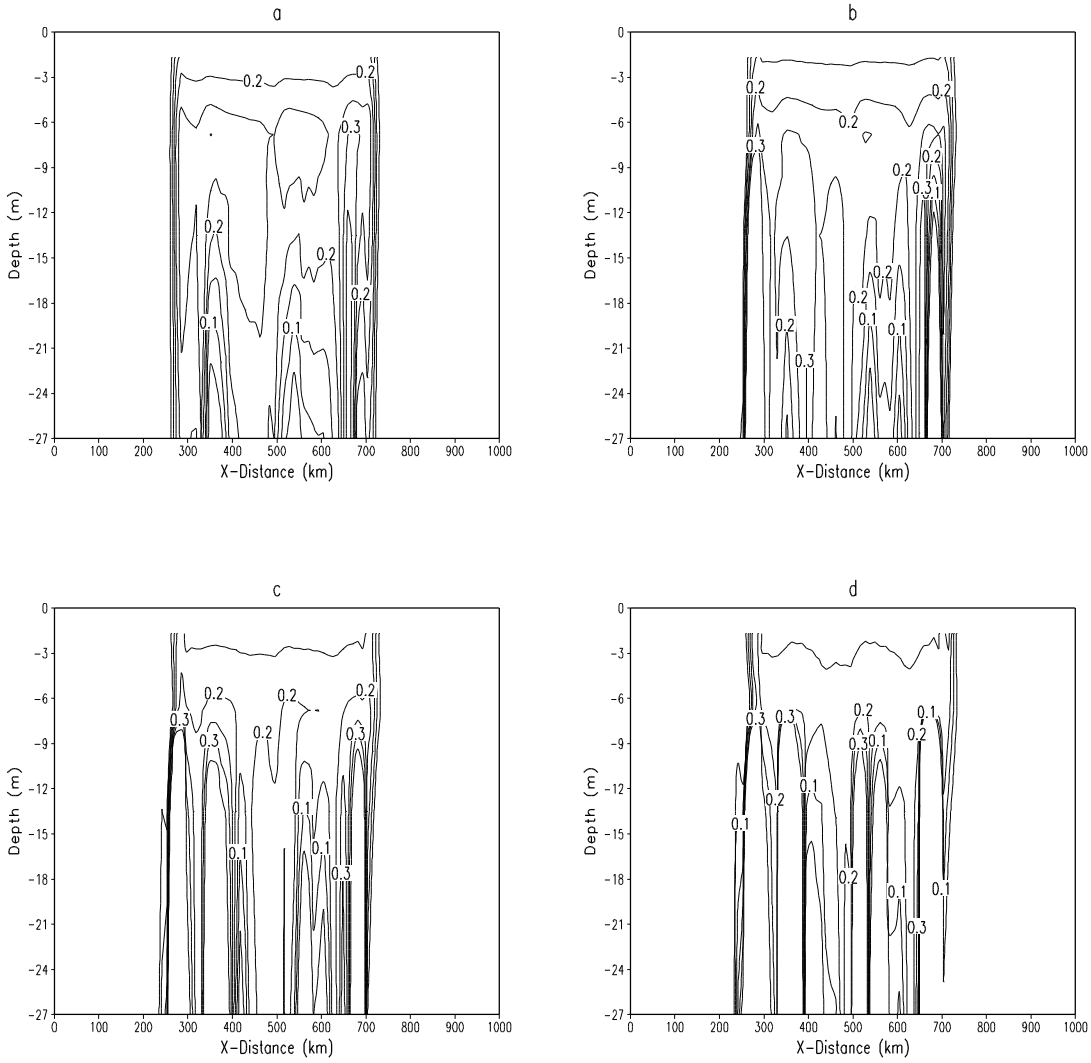

Figure 3.21. Simulated vertical (X-Z) cross-sections of the differences between Richardson number with and without rainfall (a) 2h (b) 3h (c) 4h (d) 5h since the beginning of simulation.

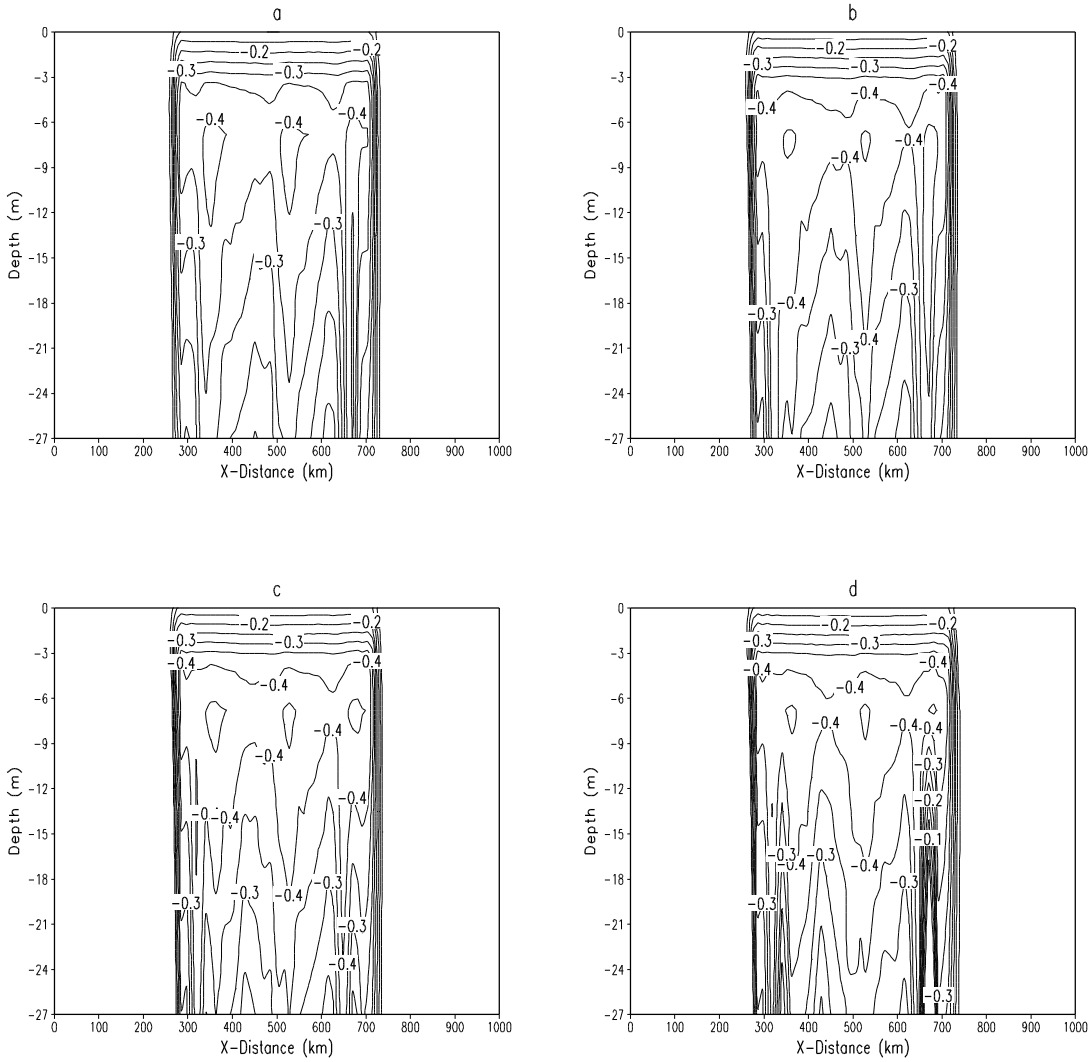

Figure 3.22. Simulated vertical (X-Z) cross-sections of the differences between the values of S_h with and without rainfall (a) 2h (b) 3h (c) 4h (d) 5h since the beginning of simulation.

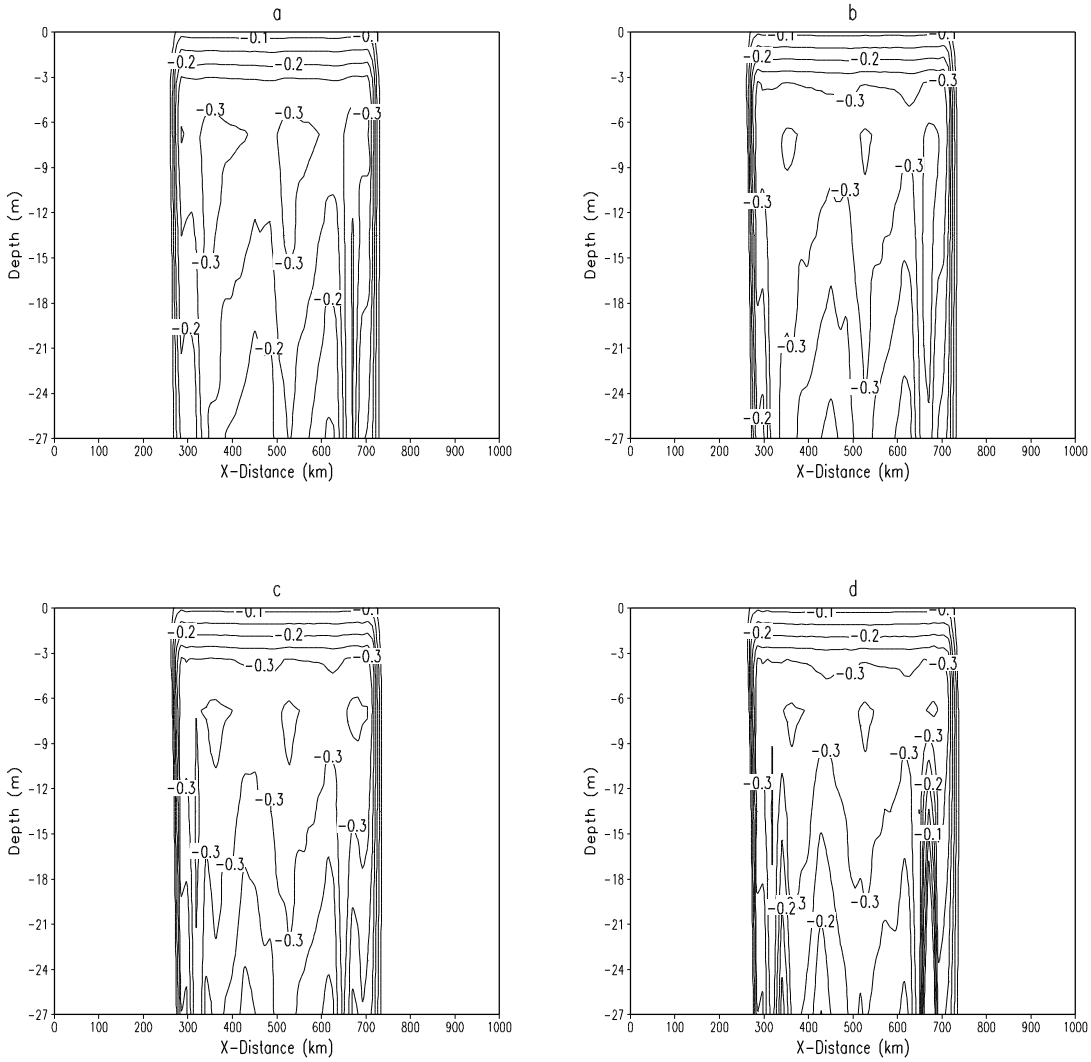

Figure 3.23. Simulated vertical (X-Z) cross-sections of the differences between the values of S_m with and without rainfall (a) 2h (b) 3h (c) 4h (d) 5h since the beginning of simulation.

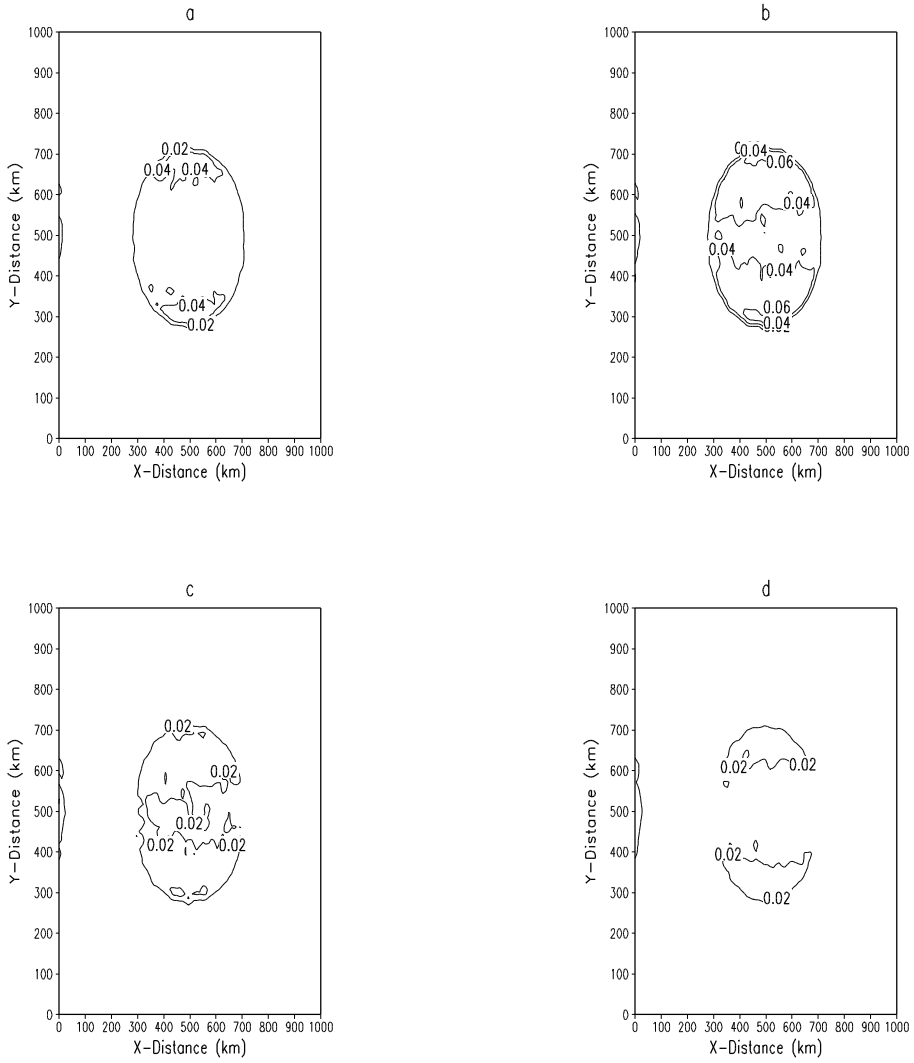

Figure 3.24. Simulated SST (K) anomalies due to the short-wave radiation with no rainfall in Exp 4 (a) 1h (b) 2h (c) 3h (d) 4h since the beginning of the experiment.

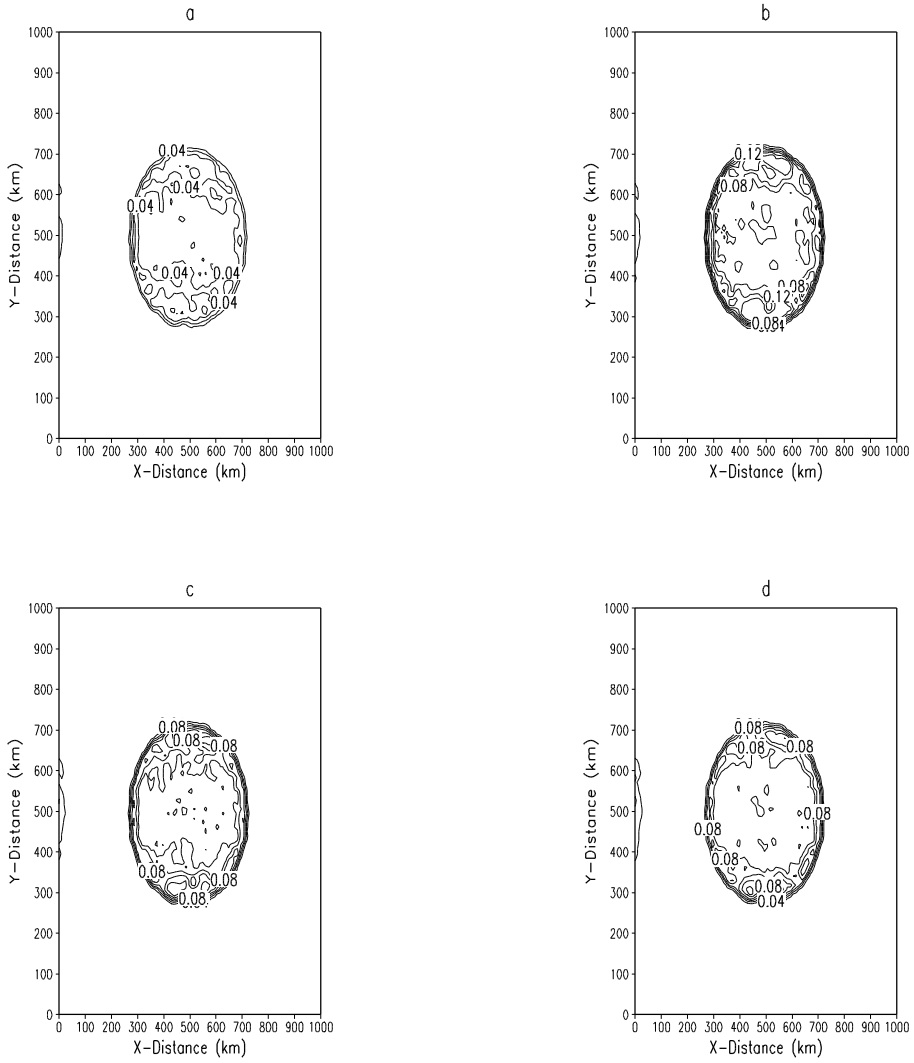

Figure 3.25. Simulated SST (K) anomalies due to the short-wave radiation with rainfall in Exp 5 (a) 1h (b) 2h (c) 3h (d) 4h since the beginning of the experiment

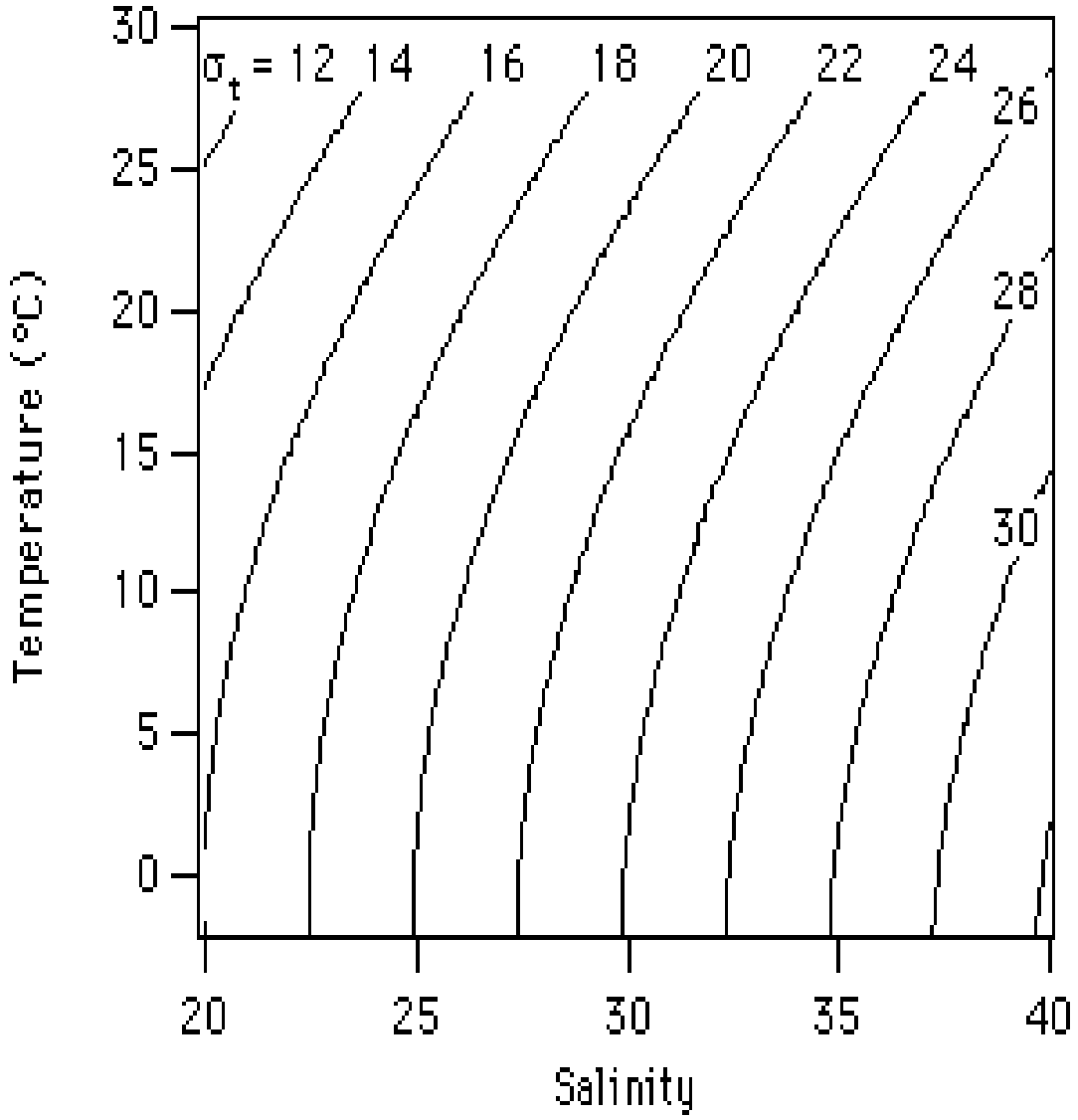

Figure 3.26 illustration of the general relationship between seawater density, salinity and temperature

Chapter 4. OCEAN'S RESPONSE TO SQUALL LINES AND ITS FEEDBACK TO ATMOSPHERE

4.1. Model description and Coupling method

Atmospheric and oceanic boundary layers are intrinsically coupled. In general, kinetic energy is transferred from the atmosphere to the ocean mixed layer, driving the circulation of the upper ocean. In turn,thermal energy is fed back from ocean to atmosphere, affecting the atmospheric circulation, the weather and the climate. These energy transfer processes are carried out at the atmosphere-ocean interface through momentum, heat (sensible and latent) and freshwater fluxes. The physical processes that are responsible for these exchanges include, among others, wind forcing (causing momentum transfer from atmosphere to ocean), precipitation (causing freshwater flux and sensible heat flux), evaporation (causing salinity and latent heat fluxes), sensible heat flux and short and long-wave radiation. Fig4.1 illustrates the natural material and energy exchange processes occurring across the atmosphere-ocean interface.

An air-sea coupled numerical model that includes the material and energy transfer processes illustrated in Fig.4.1 (momentum, salinity, sensible and latent heat fluxes) is necessary to investigate the mesoscale air-sea interaction processes because direct observations of the air-sea interactions are difficult and often limited to a few specialized platforms. The direct observation data of the sea surface are especially insufficient to properly describe mesoscale convection processes such as the ones occuring in a squall line whose time scales are only a few hours. During the occurrence of such convection processes, satellite data of the sea surface are generally not available due to the deep clouds covering the sea surface, thus making the numerical model a necessity. In our study of the mesoscale tropical convection processes atmospheric radiation effects are neglected due to the relatively short 6-hour duration.

Because the exchange processes across the air-sea interface cannot be quantified analytically, parameterization of the air-sea fluxes are generally used in mesoscale and climate models. In this study, the bulk aerodynamic method (a commonly used parameterization model) is used to estimate the momentum, heat and freshwater fluxes across the air-sea interface.

According to the bulk model:

$$\overline{(u'w')_s} = -C_d \overline{M}\overline{U} \tag{4.1}$$

$$\overline{(v'w')_s} = -C_d \overline{M}\overline{V} \tag{4.2}$$

$$\overline{(q'w')_s} = -C_E \overline{M}\left(\overline{q} - q_G\right) \tag{4.3}$$

$$\overline{(q'w')_s} = -C_H \overline{M}\left(\overline{q} - q_G\right) \tag{4.4}$$

Where

$\overline{(u'w')_s}$ and $\overline{(v'w')_s}$ = the momentum fluxes

$\overline{(q'w')_s}$ = moisture flux

$\overline{(q'w')_s}$ = heat flux

C_D = drag coefficient

C_H and C_E = bulk transfer coefficient for heat and moisture, respectively

$\overline{M}$ = mean horizontal wind magnitude above the surface

$\overline{U}$ and $\overline{V}$ = mean horizontal wind vectors above the surface

$\overline{q}$ and $\overline{q}$ = mean potential temperature and moisture above the surface

q_G and q_G = mean potential temperature and moistureat the sea surface

The calculated $\overline{(u'w')_s}$ $\overline{(v'w')_s}$ $\overline{(q'w')_s}$ $\overline{(q'w')_s}$ are used as the bottom boundary condition for the atmosphere model and as the top boundary condition in the ocean model.

The precipitation-induced heat flux (F_t) and freshwater flux (F_s) are given by (Curry and Webster,1999):

$$F_s = r\,IS_o \tag{4.5}$$

$$F_t = r\,C_p I(T_a - T_o) \tag{4.6}$$

where

r = water density

I = rainfall intensity

S_o = surface salinity

C_p = specific heat of liquid water (4218 JK^{-1}/Kg)

T_a = atmospheric temperature near the surface and assumed to be equal to rain drop temperature

T_o = sea surface temperature

The atmospheric model used in this coupledsystem is the Advanced Regional Prediction System (ARPS), developed at the University of Oklahoma(Xue *et al.*, 1995). The ocean model used in this study isthe Princeton Ocean Model (POM) of Princeton University (Blumberg *et al.*,1987). A Message Passing Interface (MPI) is used to communicate betweenthese two models. MPI, used widely on almost all Unix multi-processor platforms, is a library that provides powerful, efficient and portable way to implement parallel computation. Using MPI, two separate programs can exchange data. In this case, ARPS model and POM model can exchange momentum, heat and freshwater fluxes and sea surface temperature, concurrently (see Fig4.2).

4.2. Model Configuration and Experiment Design

, Simulation of the ocean's response to an idealized precipitation processwas discussed in Chapter 3. The results showed that precipitation hasa significant effect on sea surface temperature (SST). However, the SST variation in the ocean model was not fed back into the atmosphere as the bottom boundary condition in ARPS

model. Instead, the bottom boundary condition was set to be a constant. In this Chapter, two experiments are conducted to investigate whether the SST variation due to the precipitation has any effect on the atmosphere and in particular convection processes. A squall line observed during TOGA COARE (Webster and Lukas, 1992) is simulated. In EXP 4.1, both the ocean's responses to the squall line and the SST's feedback effects on the atmosphere are investigated. That is, in the ARPS model, the bottom boundary conditionis updated to include the SST variationsimulated in POM. In a companion experiment, EXP 4.2, all the model configurations are the same as in EXP 4.1 except that the SST variation in POM model is not fed back into atmosphere. The difference between the simulated results in EXP 4.1 and EXP 4.2 are analyzed to investigate the SST's feedback effects on the atmosphere. The model configurations are shown in Table 4.1.

Table 4.1 Experiment design for the simulations of air-sea interaction using the coupled modeling system

Model	ΔT **(sec)**	ΔX **(m)** ΔY **(m)**	**Mininum** ΔZ **(m)**	**Turbulent closure scheme**	**Lateral B.C.**
ARPS	6	3000	100	TKE order 1.5	Radiation (open) lateral boundary
POM	6	3000	1	Mellor Yamada order 2.5	Radiation (open) lateral boundary

4.3. Results and Discussion

4.3.1 Oceanic response to squall line

The simulation results in Chapter 2 showed that for tropical convection such as squall line processes, which last for only a few hours, precipitation, among others factors, appears to play an important role in affecting the dynamics of the upper ocean. Rain drops, which are significantly cooler than the sea surface temperature (SST), enter the ocean water and have a cooling effect on the upper ocean. Second, the addition of fresh rain water input causes the density of the ocean's surface layer to decrease, thus forming a thin low salinity, low density stable layer near the surface. However, in Chapter 3 , an idealized precipitation event was simulated. On the other hand, in EXP 4.1 and EXP 4.2, an observed squall line event is simulated. Basic results from EXP 4.1 and EXP 4.2 are in agreement with those described in Chapter 3.

The simulated evolution of sea surface temperature (SST) variations and the corresponding accumulated rainfall amounts for EXP 4.1 are shown in Figure 4.**3**. From Figure. 4.**3** it is apparent that with an increase in the accumulated rainfall amount, the SST in the rainfall covered region decreases. When the maximum accumulated rainfall amount reaches 70 mm at t = 6 hr, the maximum SST anomaly reaches -0.35^{o}C. In addition, the pattern of the SST anomaly resembles that of the accumulated rainfall, and the maximum SST anomaly is in the same location as the maximum accumulated rainfall.

It should be pointed out, however, that although precipitation plays an important role in affecting the SST, effect of sensible and latent heat fluxes cannot be neglected. Actually even during the squall line processes, which last for only a few hours, the magnitudes of sensible and latent heat fluxes are comparable to that of rain drop-induced sensible heat flux. Time series of the maximum heat transferred across the air-sea interface by sensible, latent and rainfall-induced heat fluxes (Equation 4.6) during the simulated squall line process is shown in Figure 4.**4**. It is clear that at the beginning of the simulation, when the rainfall amount is still small, the sensible and latent heat fluxes are greater than the rainfall induced heat flux. With the increase of rainfall amount, the rainfall-induced heat flux increases rapidly and surpasses the sensible and latent heat fluxes. The accumulated rainfall amount increases until t=140 minutes. With no further rainfall, the maximum rainfall-induced heat flux levels off and subsequently begins to decrease. Although during the rainfall process, the rainfall-induced heat flux is larger than the sensible and latent heat fluxes, they are of comparable magnitudes.

The reason that the sensible, latent and rainfall-induced heat fluxes have comparable magnitudes while the sea surface temperature variation only follows the accumulated rainfall can be studied by a sensitivity experiment in which the salinity variation is not included.

As mentioned in Chapter 2, rain drops enter the upper ocean as cool freshwater flux and cause a thin low temperature, low density stable layer. This thin stable layer isolates the surface layer from the rest of the upper ocean and blocks the turbulent

exchange of mass and energy between the sea surface and below. Therefore in the rainfall-covered region, the cooling effects are accumulated near the surface and the SST variations are significant and last longer. In the regions not covered by rainfall, the heat fluxes, although of similar magnitude as those in the rainfall-covered region, are transferred downward quickly from the ocean's surface to the mixed layer by turbulent mixing.

EXP 4.3, EXP 4.4 and EXP 4.5 are conducted to investigate the different roles of the sensible heat flux, latent heat flux, rainfall-induced heat flux and rainfall-induced freshwater flux in affecting the SST (Table 4.2) in the coupled model

Table 4.2 Sensitivity experiments to investigate the different effects of the sensible, latent and rainfall-induced heat fluxes on SST in the coupled model

	EXP 4.3	**EXP 4.4**	**EXP 4.5**
Rainfall-induced heat flux	included	Not included	Not included
Rainfall induced freshwater flux	included	Not included	Included
Sensible and latentheat fluxes	Not included	included	Included

Figure 4.5 shows the simulated SST variations in (a) Exp 4.1 (b) EXP 4.3 (c) EXP 4.4 and (d) EXP 4.5. It is clear from Figure 4.5 that when rainfall-induced freshwater flux is included (EXP 4.3 and EXP 4.5), the SST variations are significant, no matter whether the rainfall-induced heat flux or the sensible and latent heat fluxes

are included. EXP 4.4 has the same configuration as EXP 4.5 except that in EXP 4.5 the rainfall-induced freshwater flux is included while in EXP 4.4 it is not. When the rainfall-induced freshwater flux is not included, as in EXP 4.4, the SST variation is not significant. These results suggest thatthe rainfall-induced stable fresh water layer is a key factor in affecting the SST during tropical squall line processes.

4.3.2 The effects of SST variation on atmospheric convection

Simulation results in Chapter 2 and 4.3.1 showed that the tropicalconvection can have significant effects on the upper ocean. However, one important question remained unanswered is whether the rainfall-induced SST variation could, in turn, influence the atmospheric processes.

EXP 4.1 and EXP 4.2 were carried out to investigate the coupling effects. Some important features of the simulated squall line process, including the rainfall amount, maximum updraft and downdraft and cloud top heights were compared between the coupled and uncoupled experiments.

Time series of the simulated maximum accumulated rainfall amount in coupled and uncoupled experiments is shown in Figure 4.6. Time series of the simulated total accumulated rainfall amounts for coupled and uncoupled experiments is shown in Figure 4.7. Comparing Figure 4.**6** and Figure 4.**7** it is clear that the rainfall amounts in coupled and uncoupled experiments have no significant difference. The maximum updrafts and downdrafts in coupled and uncoupled experiments, shown in Figure 4.8, have no systematic difference either. The vertical (X-Z) cross-sections of the amount

of cloud water, cloud ice and cloud snow across the locations of the maximum updrafts, in (a) coupled and (b) uncoupled experimentsare shown in Figure 4.9. The cloud tops reachedan altitude of 15000 m on the 2nd hour since the simulations started and remained at that height for six hours of the simulations in both the coupled and uncoupled experiments.

The vertical cross-sections of the vertical gradients of the equivalent potential temperature are shown in Figure 4.10. Equivalent potential temperature, or theta-E, shows the temperature air would have if it ascended until all the water vapor is condensed out, and the airis brought back down to 1000 mb. The negative anomalies in Figure 4.10, which indicate decreasing theta-E with height, show the region with potential instability and the positive anomalies correspond to stable downdraft regions behind the leading edge of the convective lines. It is apparent that no significant difference is seen in Figure 4.10 between the simulated potential instabilities in coupled and uncoupled experiments. Therefore, theSST's feedback effect does not appear to have a significant effect on the stability profiles of the convective systems in the atmosphere.

The reason that the rainfall-induced SST variation has nosignificant effect on the convection may be that the tropical squall line process simulated in this study moves in a direction perpendicular to the low level wind shear at a speed of about 12 m/s. The SST variations occur over the rainfall covered region, behind the leading edge of the squall line convection. Therefore, in the region where the SST variations are significant, the downdrafts are dominant and the convections are at the stage of dissipation. When the sea surface cooling effects are fed back into atmosphere in the

rainfall covered region, the active convection has already moved along the direction perpendicular to the low level wind shear to the region where the underlying SST has not been modified by the rainfall. Since the rainfall-induced SST variation is lagging far behind the leading edges of the squall lines, it has no signficant effect on the atmosphere convectionthat produced the rain

4.3.3 The effects of SST variation on heat fluxes across air-sea interface

Although the SST variation has no significant effect on the atmospheric convection processes, the study results show that it does have significant influences on the sensible and latent heat exchanges across theair-sea interface.

The only parameter in the ocean model that is fed back into atmosphere model is the sea surface temperature (SST). The SST spatial variation corresponds well with the distribution of rainfall. Time series of the total sensible heat flux and latent heat flux across the air-sea surface over the rainfall covered regions in coupled and uncoupled experiments are shown in Figure 4.11. It is apparent that in the beginning of the simulation, when the rainfall amount is still small, magnitude of the sensible and latent heat fluxes over the rainfall-covered regions are small and no significant difference is seen between the coupled and uncoupled experiments. With the increase in rainfall amount and its coverage, difference in the heat fluxes between coupled and uncoupled models increases substantially. The difference in the total heat fluxes over rainfall-covered region between the coupled and uncoupled simulations can be as high as 6 % of the simulated value in the coupled experiment. Time-averaged differences in the heat fluxes between coupled and uncoupled experiments are 3.8 % for the latent

heat flux and 3.2 % for the sensible heat flux. That means when precipitation is present and if the rainfall-induced heat flux and freshwater flux are neglected, the heat transferred across the air-sea interface will be over-estimated by about 3 % to 6 %.

In order to validate the argument that the heat flux differences shown in Figure 4.**11** is the result of the SST variation, a correlation analysis was performed between the SST and the differences in the sensible heat flux, latent heat flux, SST, surface moisture, bulk transfer coefficients of heat and moisture, surface velocity and rainfall amount between the coupled and uncoupled The results are shown in Table 4.3. Correlation for the rainfall and the heat fluxes are shown in Figure 4.12.

Table 4.3. Correlation of the differences in $\overline{(q'w')}_S$, $\overline{(q'w')}_S$, q_G, q_G, C_H, C_q, $\overline{M}$ and rainfall amount between the coupled and uncoupled experiments

	D_S_Flux	D_L_Flux	D_SST	D_QVS	D_Ch	D_Cq	D_M	Rainfal
D_S_Flux	1.00	.98	.97	.97	.63	.63	.04	0.97
D_L_Flux	.98	1.00	.96	.96	.49	.49	.22	0.97

In Table 4.3 and Figure 4.12:

D_S_Flux = Sensible heat flux_uncoupled – Sensible heat flux_coupled
D_L_Flux = Latent heat flux_uncoupled – Latent heat flux_coupled
D_SST = Sea surface temperature_uncoupled-sea surfacetemperature _coupled
D_QVS = Sea surface moisture_uncoupled- Sea surface moisture_coupled
D_Ch = bulk heat transfer coefficient_uncoupled- bulk heat transfer coefficient_coupled
D_Cq = bulk moisture transfer coefficient_uncoupled- bulk moisture transfer coefficient_coupled
D_M = surface velocity_uncoupled-surface velocity_coupled

In Eq. 4.**3** and Eq. 4.4, q_G, q_G, $\overline{M}$, C_q and C_H could affect the sensible heat flux ($\overline{(q'w')_S}$) and latent heat flux (moisture flux,$\overline{(q'w')_S}$). The time series of the simulated rainfall amount and the differences in $\overline{(q'w')_S}$, $\overline{(q'w')_S}$, between the coupled and uncoupled experimentsare shown in Figure 4.12. A correlation analysis result is shown in Table 4.3. From Figure 4.12 and Table 4.3 it is clear that the differences in the sensible and latent heat fluxes have strong correlation (>0.97) with the SST anomalies and the rainfall amount.

4.4 Conclusions

An air-sea coupled numerical model that includes the momentum, heat and salinity fluxes across the air-sea interface is developed by combining the ARPS and POM model. Results of numerical experiments using this coupled model showsthat although precipitation has significant effects on SST, the SST 's feedback into atmosphere does not have a significant influence on the atmospheric convection. However, numerical results show that the SST's feedback has significant effect on the sensible and latent heat fluxes across the air-sea interface. The difference in the simulated heat fluxes is of the order of + 6% when rainfall is included.

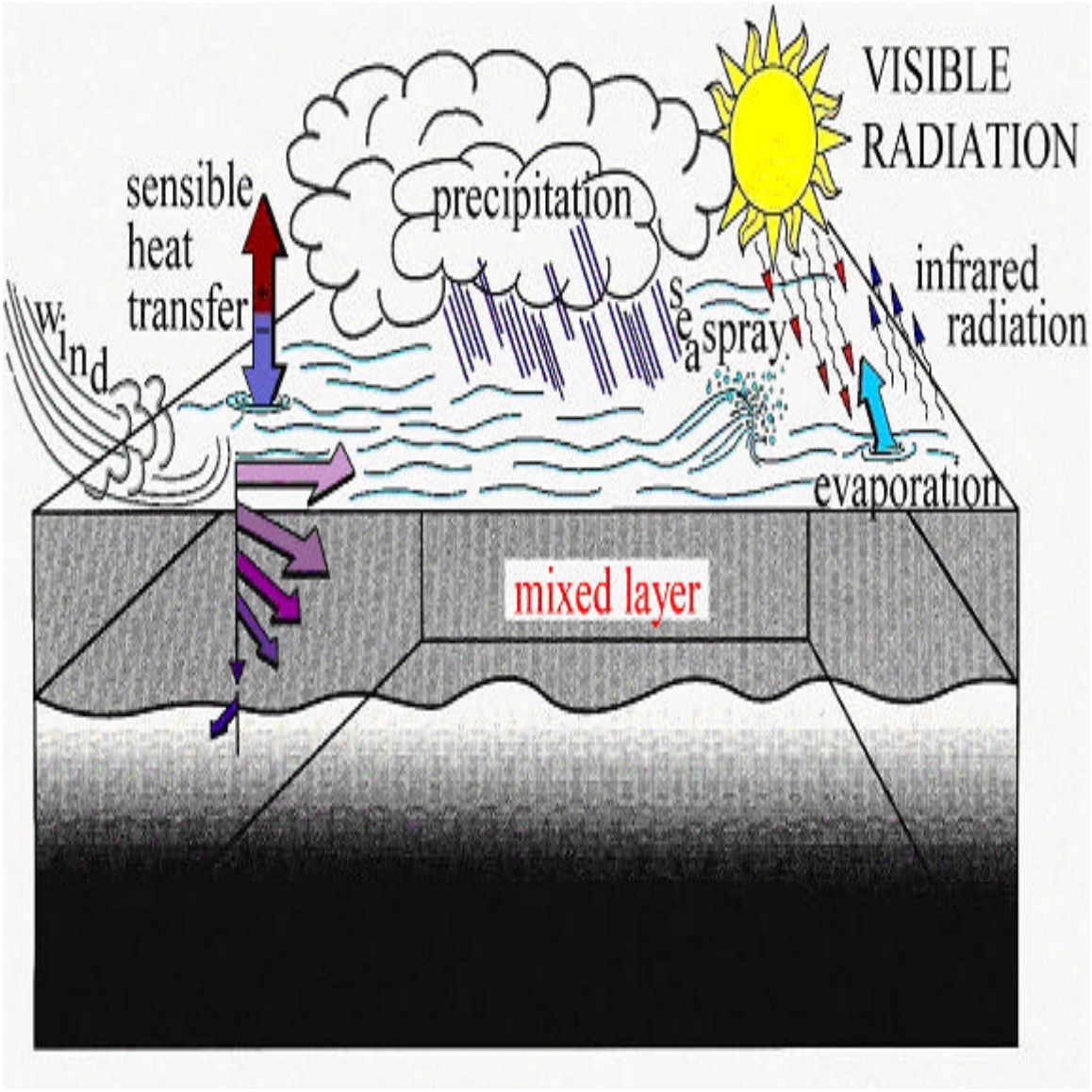

Figure 4.1 Schematic illustration of the mass and energy transfer processes across the air-sea interface in nature (see *http://www.soc.soton.ac.uk/JRD/MET/*).

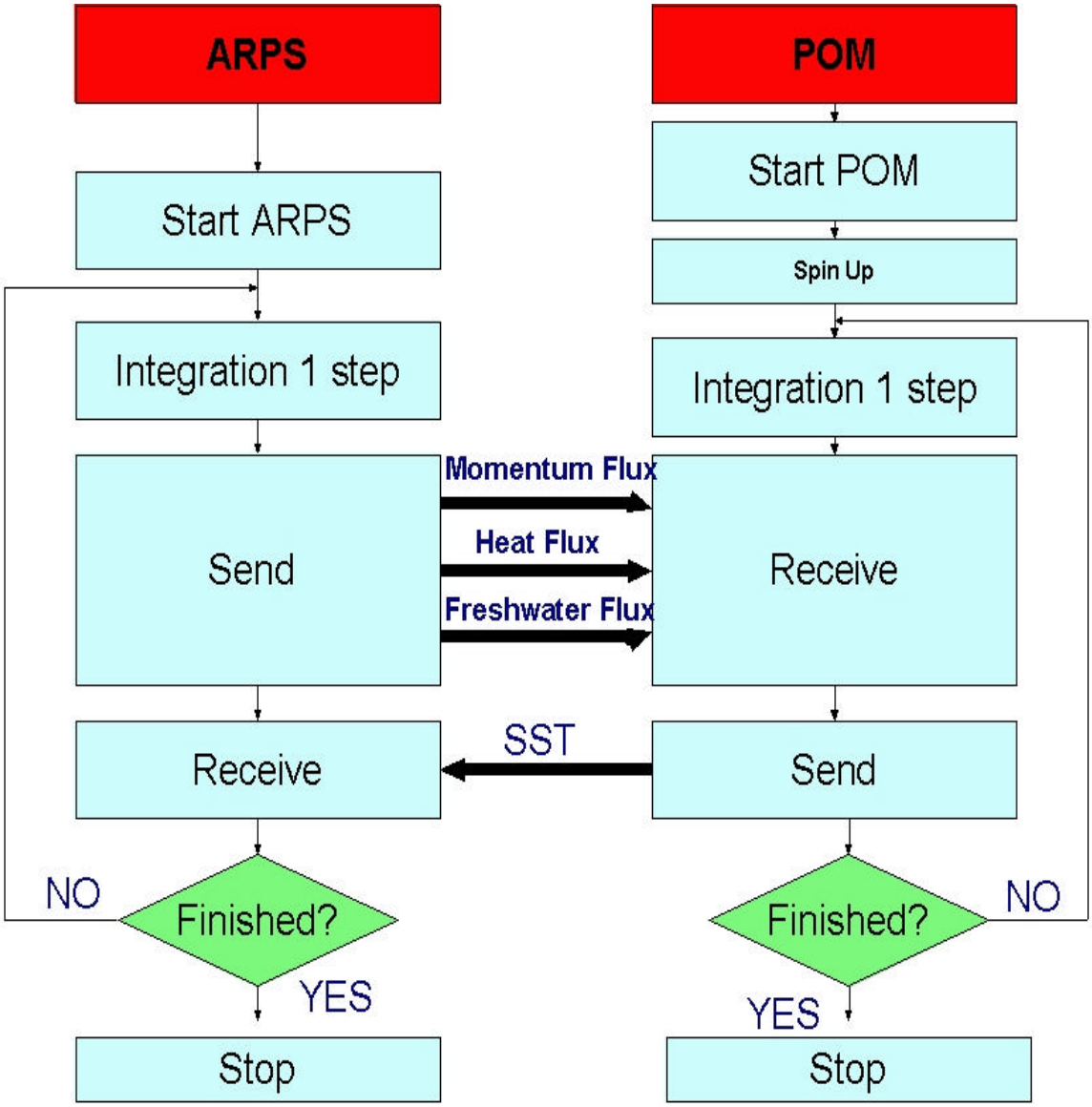

Figure 4.2. Schematic illustration of the method used in coupling the ARPS and POM model

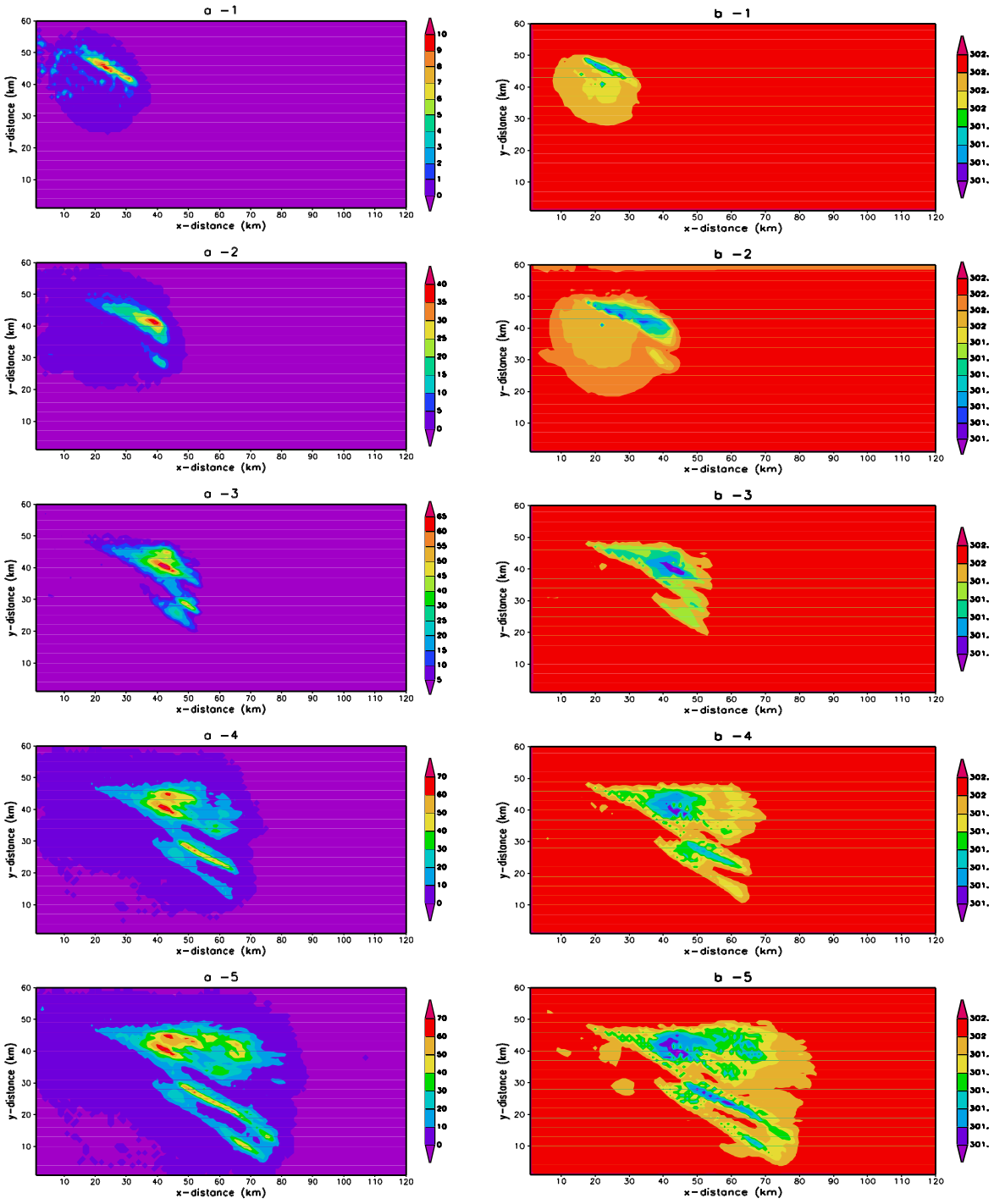

Figure 4.3 Simulated evolution of (a) sea surface temperature (SST)variations (in K) and (b) the corresponding accumulated rainfall amount(in mm) in EXP 4.1

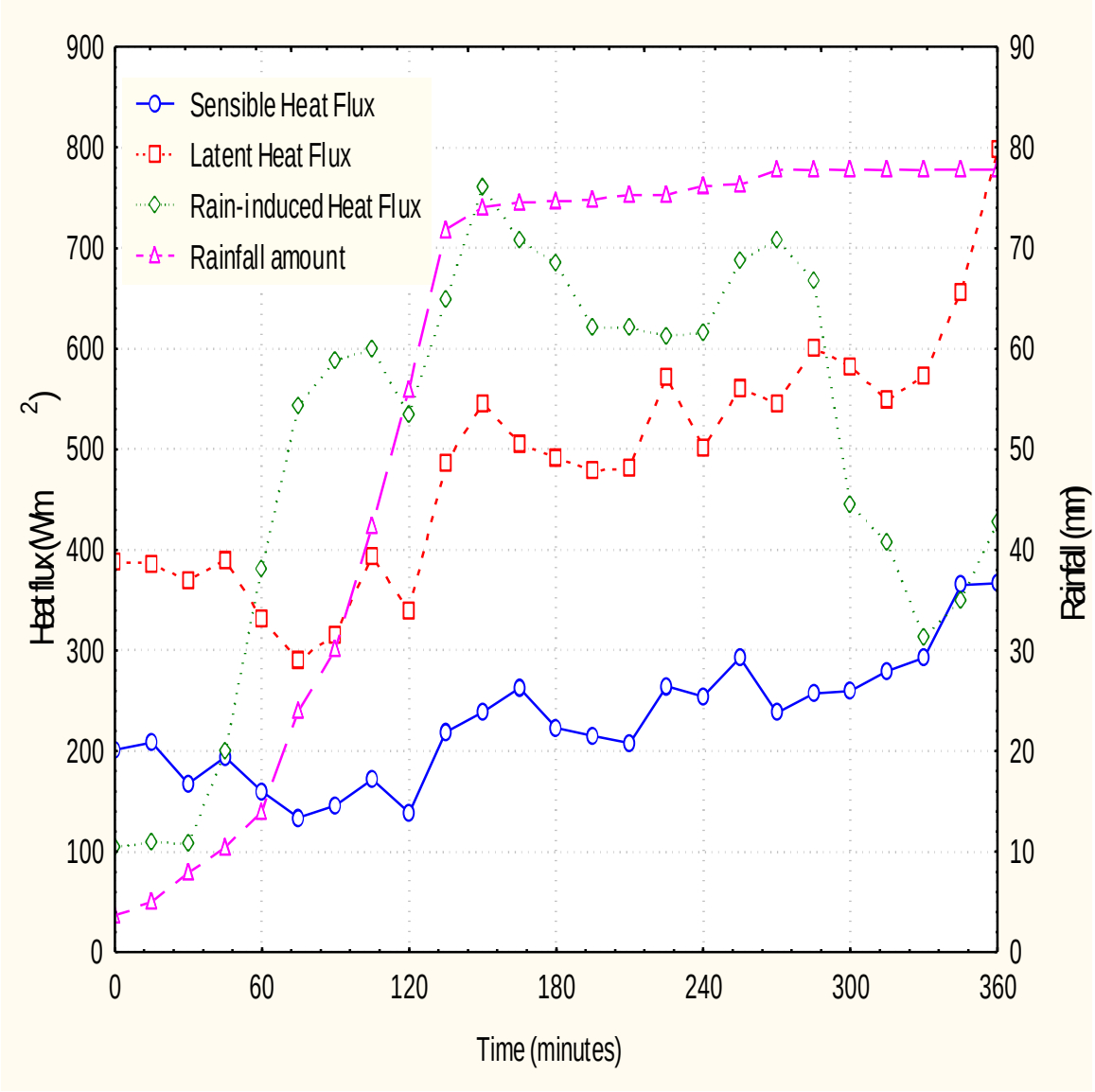

Figure 4.4 Time series of the simulated maximum rainfall amount (in mm), sensible, latent and rainfall-induced heat fluxes (in W/m^2) across the air-sea interface during the life cycle of the simulated squall line .

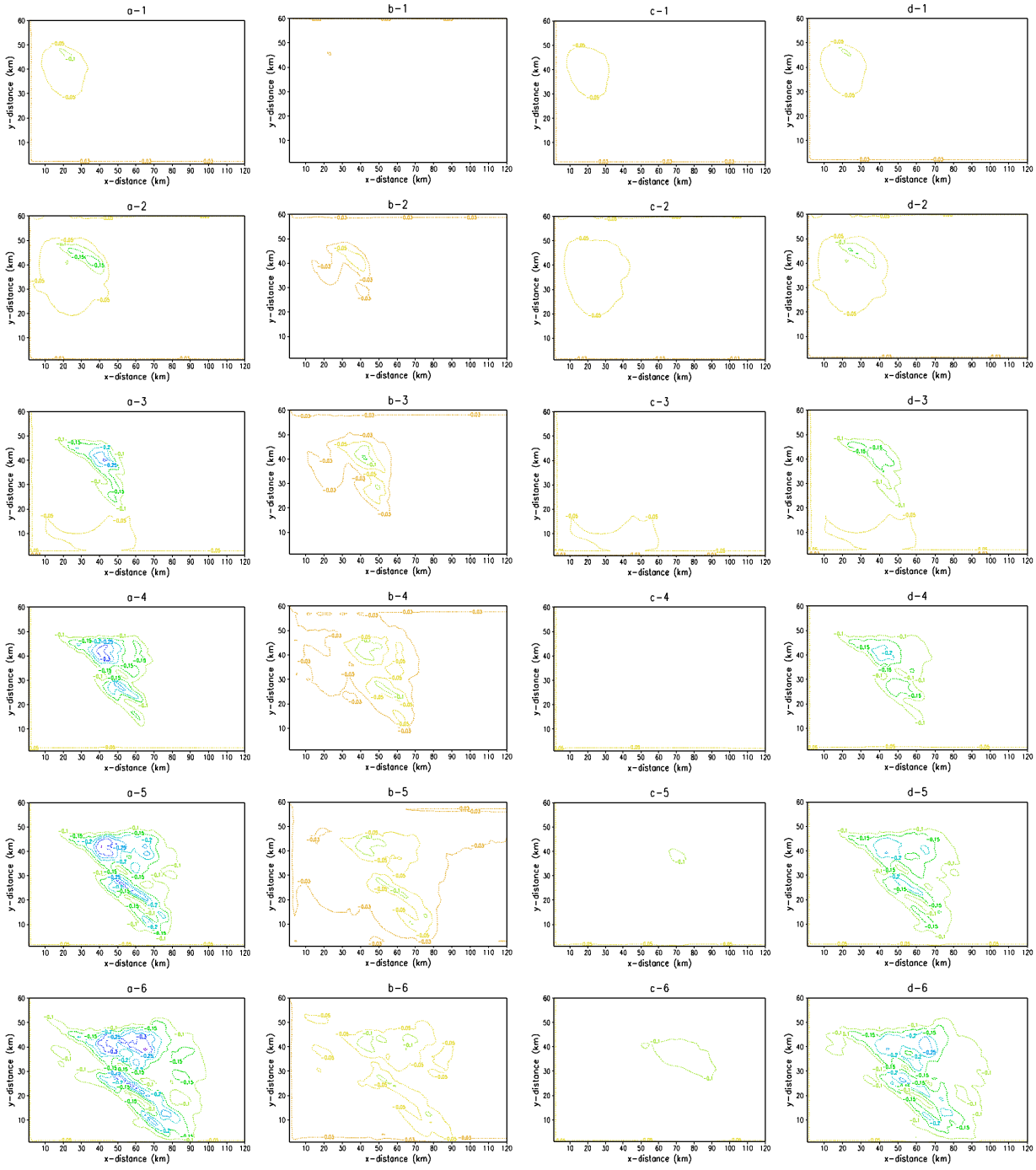

Figure 4.5 Simulated SST variations (in K) in (a) Exp 4.1 (b) EXP 4.3 (c) EXP 4.4 (d) EXP 4.5. Notice that the SST variation is sensitive to the inclusion of rainfall-induced freshwater flux.

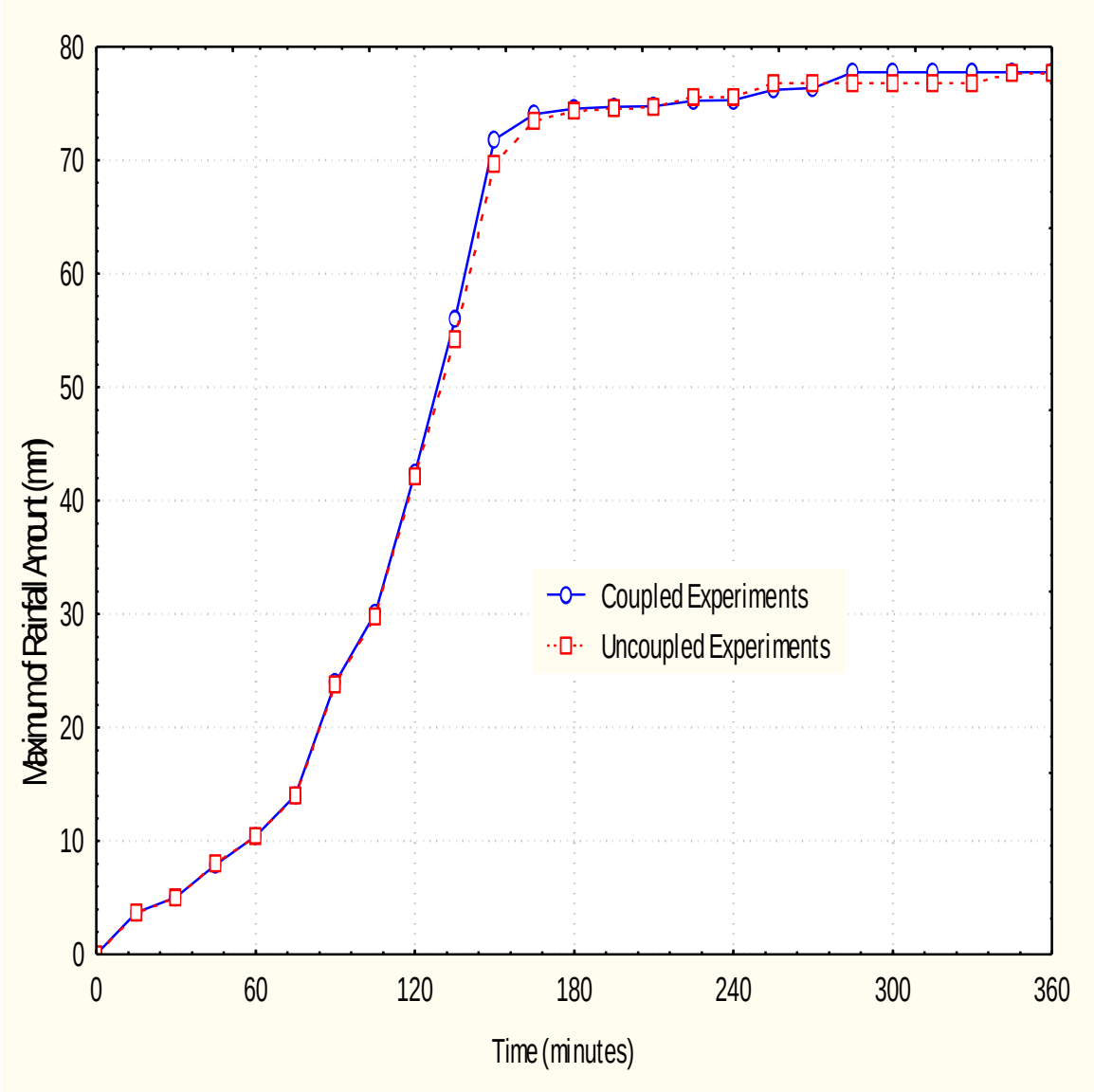

Figure 4.6 Time series of the simulated maximum of accumulated rainfall amount (in mm) in coupled and uncoupled experiments. There is no significant difference in the simulated rainfall amount between the coupled and uncoupled experiments.

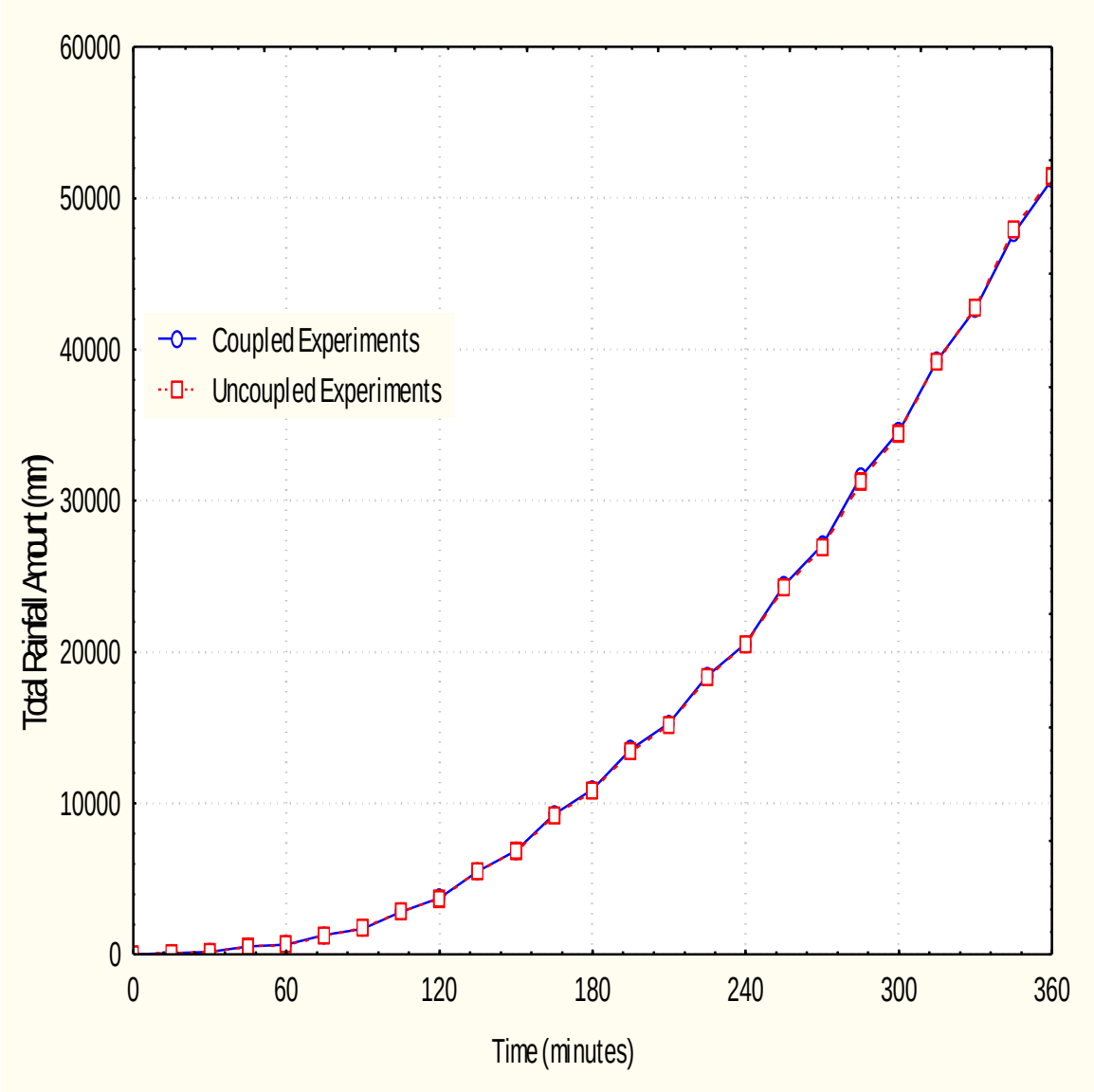

Figure 4.7 Time series of the simulated total accumulated rainfall amount(in mm) in coupled and uncoupled experiments. Notice there is no significant difference in the simulated rainfall amount between the coupled and uncoupled experiments.

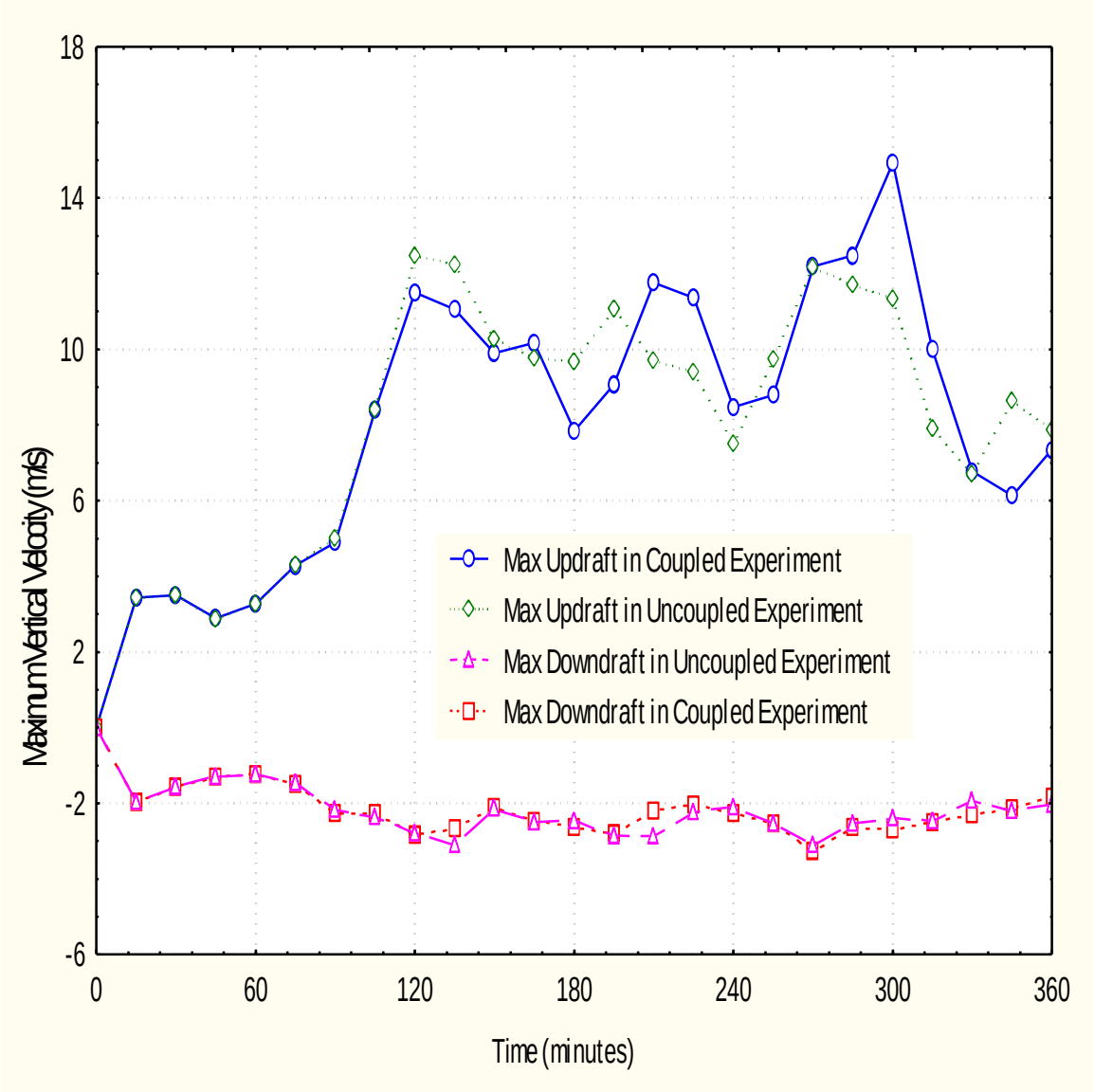

Figure 4.8 Time series of simulated maximums of updrafts and downdrafts (in m/s) in coupled and uncoupled experiments. There is no significant difference in the simulated updrafts and downdrafts between the coupled and uncoupled experiments.

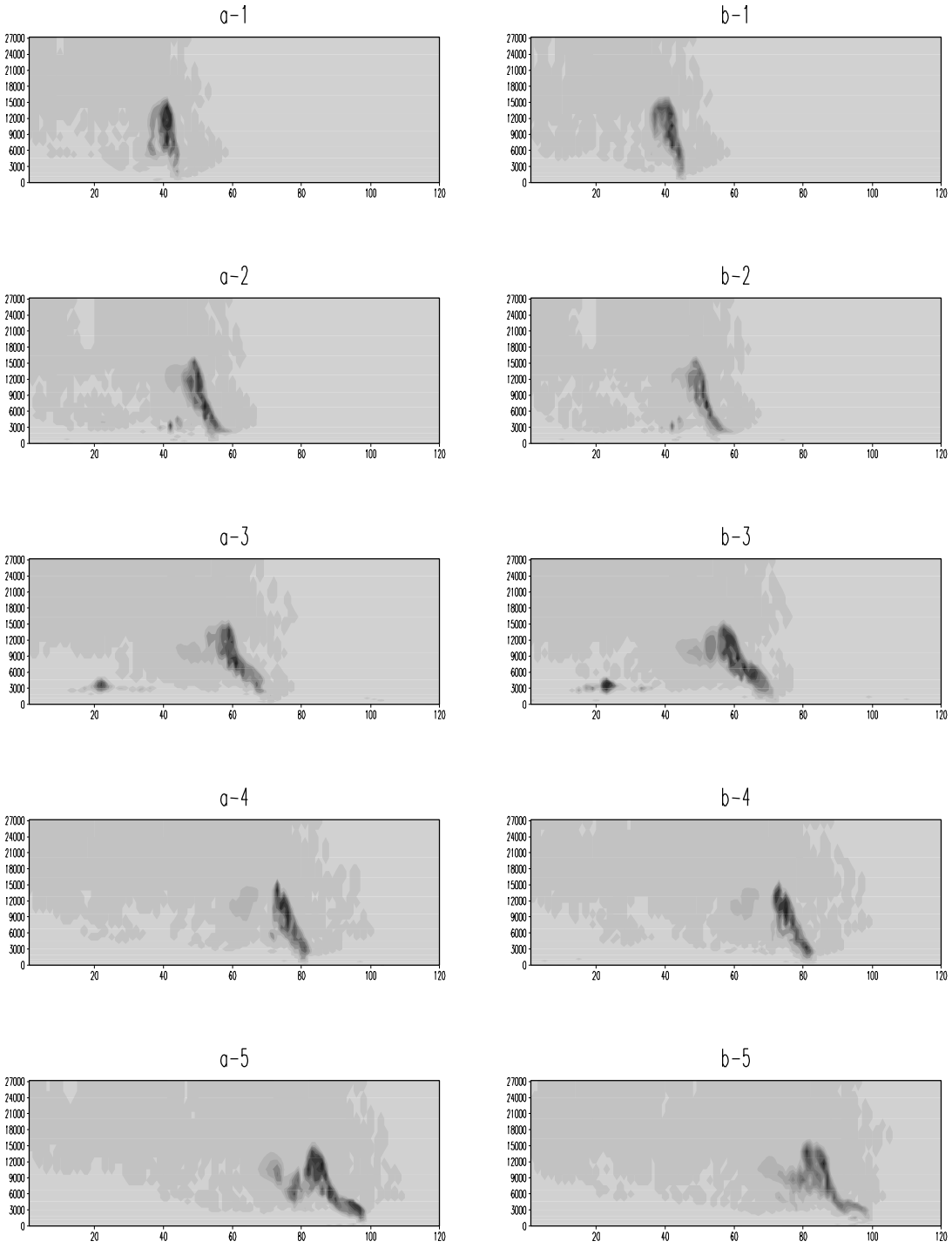

Figure 4.9 Vertical (X-Z) cross-sections of the amount of liquid cloud, ice cloud and snow cloud, made across the locations of the maximum updrafts, in (a) coupled and (b) uncoupled experiments. Notice no significant difference in cloud height is seen.

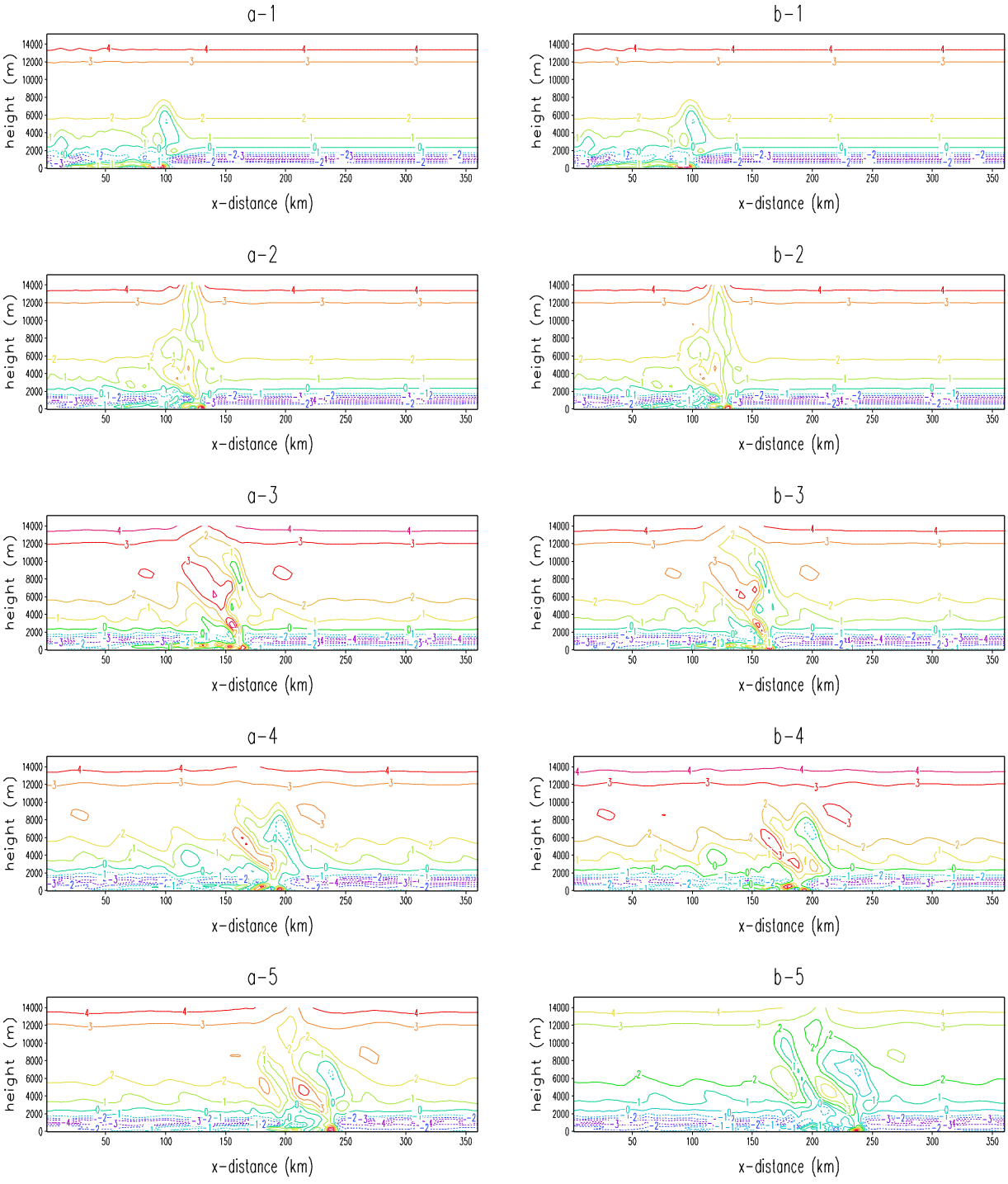

Figure 4.10 Vertical cross-sections of the vertical gradients of the equivalent potential temperature (K) in (a) coupled experiments and (b) uncoupled experiments (1) 1h (2) 2h (3) 3h (4) 4h (5) 5h since the simulations begin. Notice that there is no significant difference is apparent between the coupled and uncoupled experiments.

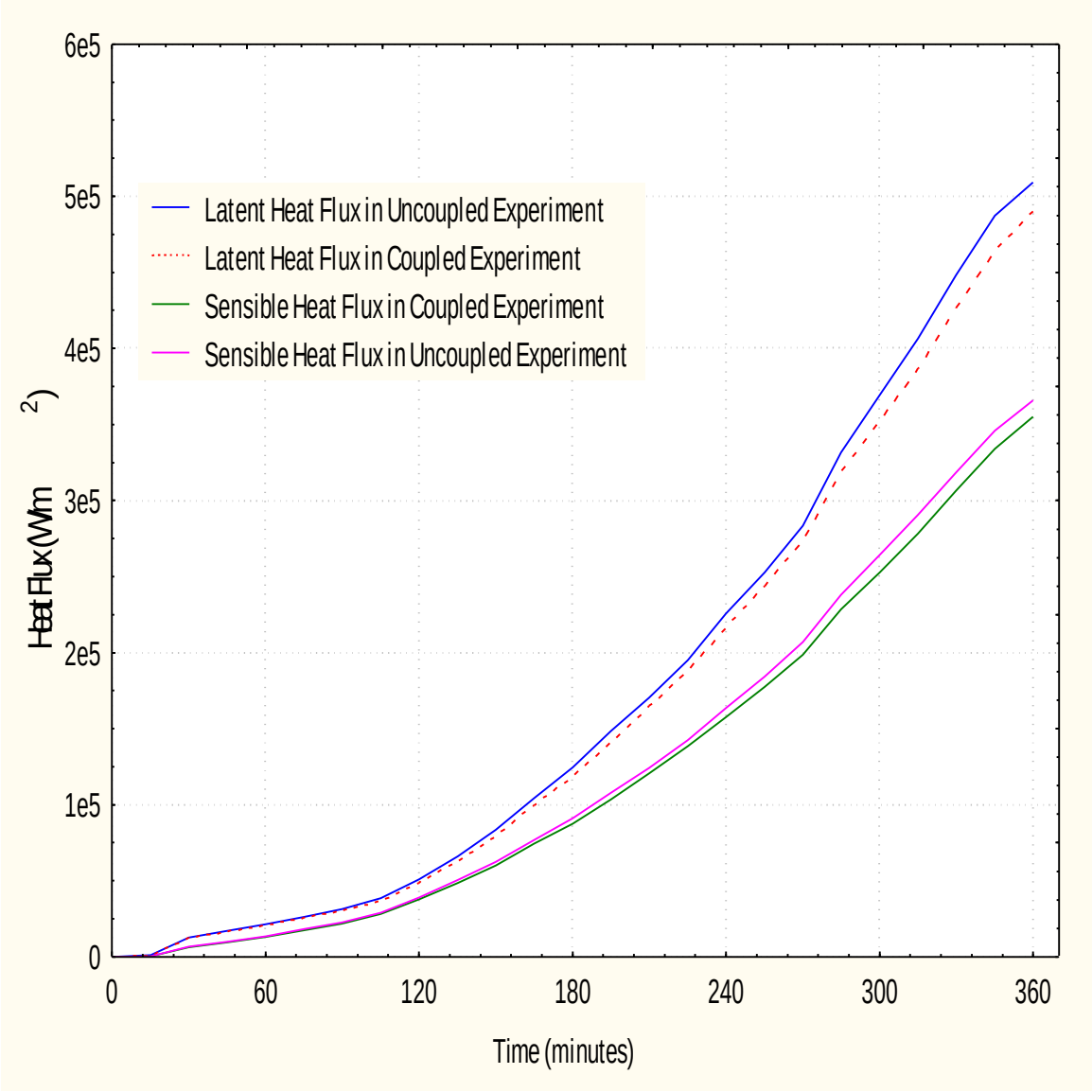

Figure 4.11 Time series of the total sensible heat flux and latent heat flux (in W/m^2) across the air-sea surface over the rainfall covered regions in coupled and uncoupled experiments. Simulated sensible and latent heat fluxes differ between the coupled and uncoupled experiments.

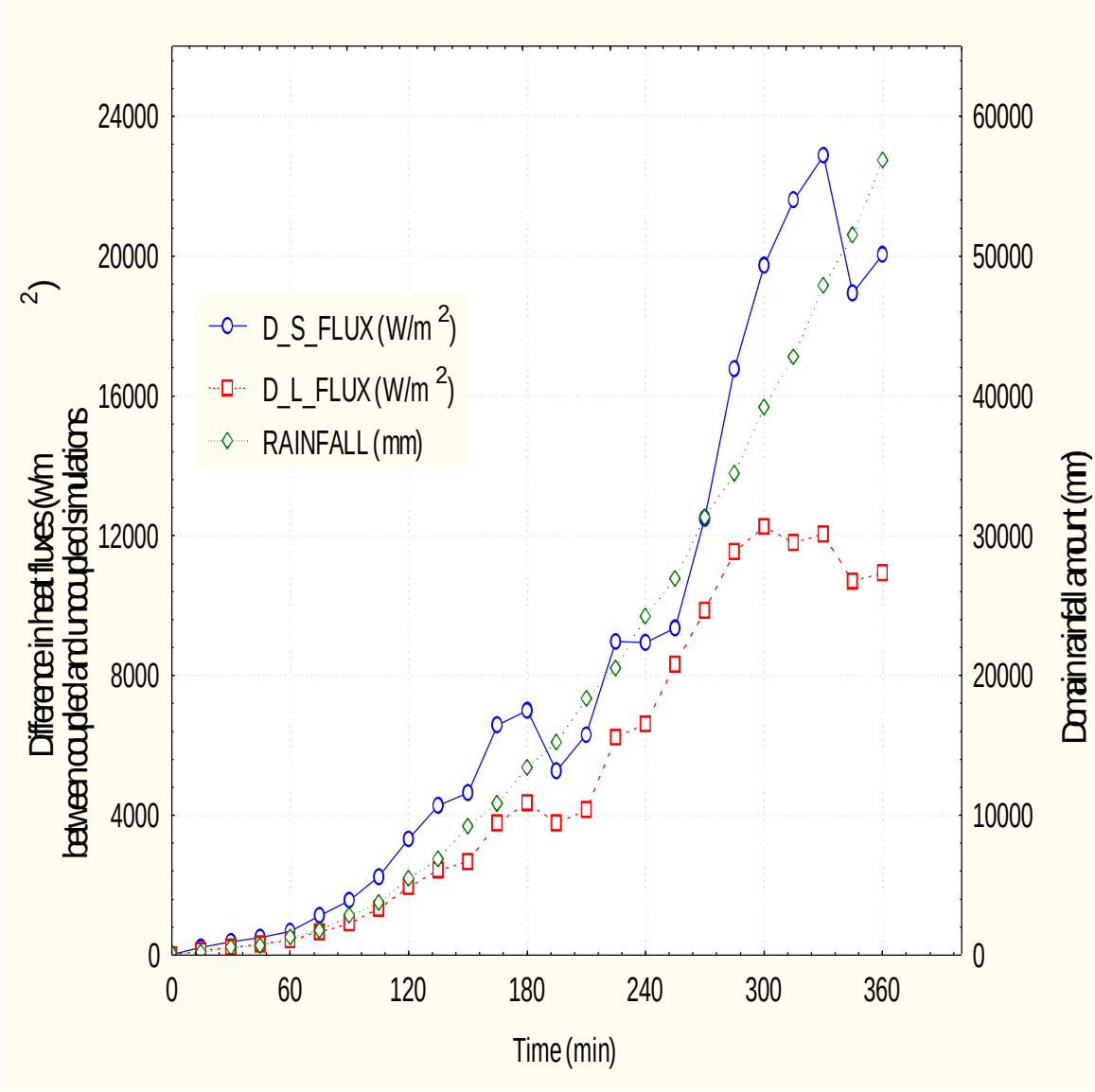

Figure 4.12 The time series of sum of the simulated differences in $(\overline{q'w'})_S$ (D_S_FLUX, in W/m^2), $(\overline{q'w'})_S$, (D_L_FLUX, in W/m^2) and the rainfall amount (mm) over the rain covered region between the coupled and uncoupled experiments. Variation of the heat fluxes and the rainfall amount have similar pattern indicating their strong correlation.

Chapter 5 CONCLUSIONS

The main objective of this research is to investigate the air-sea interaction processes and their effect on mesoscale convectionover the region of western Pacific warm pool. A squall line system observed during TOGA/COARE IOP is simulated using ARPS model.

The simulation results are in agreement with the observations. Sensitivity experiments reveal that the structure and evolution of the squall line system are sensitive to the inclusion of the ice microphysics, surface fluxes and especially, the orientation of the initial temperature perturbation.

The ocean's response to precipitation is investigated using the Princeton Ocean Model (POM). The result shows that the rainfall-induced heat and salinity fluxes cause a thin low density, low temperature stable layer near sea surface. Because of this rainfall-induced stable layer, the sea surface responds to atmospheric forcing much faster than it would do without the rainfall-induced stable layer. This process causes significant changes in the sea surface temperature (SST) over the rainfall-covered region.

An air-sea coupled numerical model that includes the momentum, heat and freshwater fluxes across the air-sea interface is developed by combining the ARPS and the POM model. Results of the numerical experiments using this coupled model shows that although precipitation has significant effect on the magnitude and distribution of the SST, simulated SST feedback into the atmosphere does not affect the overlying atmospheric convection, probably due to the fast movement of the

convection system. However, numerical results show that the SST feedback does affect the magnitudes of the sensible and latent heat fluxes across the air-sea interface. Magnitudes of the simulated sensible and latent heat fluxes without rainfall are about 6 % larger than the simulation with rainfall.

Although SST feedback does not affect the overlying atmospheric convection, the changed heat fluxes across the air-sea interface in the region of precipitation would cause horizontal gradients in sea surface temperature and cause local circulation, which in turn can trigger new mesoscale convection cells. There is a need to develop parameterizations that will include mesoscale precipitation effects on the surface flux gradients in weather prediction and climate models

List of References

Bjerknes, J., 1966: A Possible Response of the Atmosphere Hadley Circulation to Equatorial Anomalies of Ocean Temperature. *Tellus*,18, 820-829

Bjerknes, J., 1969: Atmospheric Teleconnections from the Equatorial Pacific.*Mon. Wea. Rev*., 97, 163-172

Blumberg, A.F., Mellor G.L., 1987, A description of a three-dimensional coastal ocean circulation model, Three –Dimensional Coastal ocean Models, edited by N. Heaps, American Geophysical Union, pp. 208

Businger, J. A., J. C. Wyngaard, Y. Izumi and E. F. Bradley, 1971: Flux profile relationship in the atmospheric surface layer. *J. Atmos. Sci*., 28, 181-189

Curry, J. A. and Webster, P. J. Thermodynamics of Atmospheres and Oceans, International Geophysics Series Volume 65, Academic Press, 1999. PP 254.

Fairall, C. W., E. F. Bradley, D. P. Rogers, J. B. Edson and G. S. Young, 1996: Bulk parameterization of air sea fluxes for TOGA/COARE, *J. Geophys. Res.* 101, 3747-3765.

Gary Barnes, 1994, Summary Report of the TOGA COARE International Data Workshop, Toulouse, France.

Gent and Cane, 1989: A reduced gravity, primitive equation model of the upper equatorial ocean. *J. Comput. Phys.*, 81, 444-481

Germano, M., U. Piomelli, P. Moin, and W. H. Cabot, 1991: A dynamic subgrid-scale eddy viscosity model. *Phys. Fluids A* 3, 1760-1765

Harrison D. E. and A. P. Craig, 1993: Ocean model studies of upper-ocean variability at 0^{o}, 160^{o}W during the 1982 -83 ENSO: local and remotely forced response. *J. Phys. Oceanogr.*, 23, 425-451.

Hisard, H., J. Merle, and B. Vioturiez, 1970: The Equatorial Under Current at 170°E in March and April 1967. *J. Mar. Res.*, 28, 128-303.

Hong, X. D., Raman, S., Hodur, R. M. and Xu, L., 1999: The Mutual Response of the Tropical Squall Line and the Ocean. *Pure and Applied Geophysics.* 155 (1999) 1-32.

Jorgensen, D. P., T. J. Matejka, and M. A. LeMone, 1995: Structure and momentum fluxes within a TOGA/COARE squall line system observed by airborne Dopplar radar. 21st Conf. On Hurricane and Tropical Meteorology, Miami, FL, Amer. Meteor. Soc., 579-581

Jorgensen, D.P., T. J. Matejka, D. Johnson, and M. A. LeMone, 1994: A TOGA/COARE squall line seen by multiple airborne Doppler radar. Sixth Conf. On Mesoscale process, Portland, OR, Amer. Meteor. Soc. 25-28

Kantha L, H., and C. A. Clayson, 2000, Numerical Models of Oceans and Oceanic

Processes, Academic Press

Kessler, E., 1969: On the Distribution and continuity of water substance in atmospheric circulation. Meteor. Monogr., No. 32,*Amer. Meteor. Soc.* 84

Levitus, S. and T. P. Boyer, 1994, World Ocean Atlas 1994, Volume 4: Temperature, NOAA Atlas NESDIS 4 11pp

Levitus, S., R. Burgett and T.P. Boyer, 1994 World Ocean Atlas 1994, Volume 3: Salinity. NOAA Atlas NESDIS 3, 99pp

Lilly, D. K., 1962: On the Numerical Simulation of Buoyant Convection.*Tellus*, 14, 168-172

Lukas, R., and E. Lindstrom, 1991: The mixed layer of the western equatorial Pacific ocean, *J. Geophys. Res.*, 96, suppl., 3343-3357, 1991.

Mellor G. L., An equation of state for numerical models of oceans andestuaries. *J. Atmos. Oceanic Tech.* 8609-8611, 1991.

Mellor, G. L. and T. Yamada, Development of a turbulent closure model for geophysical fluid problems, *Rev. Geophys*, 20, 851-875, 1982.

Price, J.R., 1979: Observations of a rain-formed mixed layer. *J. Phys. Oceanogr.*, 9,643-649

Raymond A. Richardson, Issac Ginis, and Lewis M. Rothstein, 1999: A numerical Investigation of the local ocean response to westerly wind burst forcing in the western equatorial Pacific. *J. Phys. Oceanogr.*, **29**,1334-1352

Shaowu Bao, Sethu Raman, Lian Xie, 2000Numerical Simulation of the Response of the Ocean Surface Layer to Precipitation. *Pure and Applied Geophysics* (in press)

Shaowu Bao, Sethu Raman, Lian Xie, 2000. Numerical Simulation of a Tropical Squall Line Convection over Pacific Ocean (in press)

Smyth, W. D., P. O. Zavialov, and J. N. Moum, 1997: Decay of turbulence in the upper ocean following sudden isolation from surface forcing.*J. Phys. Oceanogr*, 27, 820—822

Soloviev, A., and R. Lukas, 1997: Sharp frontal interfaces in near;surface layer of the ocean in the western equatorial Pacific Warm Pool.*J. Phys. Oceanogr.*, 27,999—1017

Soloviev, A., R. Lukas, S. Asghar, and D. Khlebnikov, 1993: Coherent structures near the air-sea interface in the western Pacific Warm Pool (abstract). EosTrans. AGU, 74(43), Fall Meet.Supp

L

Sui, C.H., X. Li, K.-M. Lau, D. Adamec, 1997: Multiscale Air–Sea Interactions during TOGA COARE. *Monthly Weather Review*: Vol.125, No.4, pp.448–462

Trier S. B., W. C. Skamarock, M. A. LeMone, and D. B. Parsons, 1996: Structure and

evolution of the 22 February 1993 TOGA COARE Squall line: Numerical Simulations. *J.A.S.* Vol 53, No. 20 1996

Webster, P.J. and Lukas, R. 1992:TOGA COARE: The Coupled Ocean-Atmosphere Response Experiment. *Bull. Amer. Meteor. Soc*., 73, 1377-1416

Wijesekera, H. W., C. A. Paulson, and A. Huyer, 1999: The effect of rainfall on the surface layer in the western equatorial Pacific during a westerly wind burst. *J. Phy. Oceanogr*. 29, 612-632.

Xue, M., Droegemeier, K.K. and Wong, V., 1995: Advanced Regional Prediction System (ARPS) and real-time storm prediction Preprint, International workshop on limited-area and variable resolution models, 23-27 Oct., 1995. WMO, Beijing, China

Yoshida, K., 1959: A theory of the Cromwell current (the equatorial undercurrent) and of the equatorial upwelling. *J. Oceanogr. Soc. Japan*, **15** 159-170

Zhang, K. Q. and L. M. Rothstein, 1998: Modeling the oceanic response to westerly wind bursts in the western equatorial Pacific. *J. Phys. Oceanogr.*, 28, 2227-2249